Stony Brook University

Dynamics of Alcohol and Ketone Photooxidation Reactions on TiO_2(110)

A Dissertation presented

by

Matthew D. Kershis

to

The Graduate School

in Partial Fulfillment of the

Requirements

for the Degree of

Doctor of Philosophy

in

Chemistry

Stony Brook University

May 2016

Stony Brook University

The Graduate School

Matthew D. Kershis

We, the dissertation committee for the above candidate for the

Doctor of Philosophy degree, hereby recommend

acceptance of this dissertation

Michael G. White, Ph.D. - Dissertation Advisor
Professor, Department of Chemsitry

Trevor Sears, Ph.D. - Chairperson of Defense
Professor, Department of Chemistry

José Rodriguez, Ph.D. - Third Member
Senior Chemist, Brookhaven National Laboratory

Nicholas Camillone III, Ph.D. - Outside Member
Chemist, Brookhaven National Laboratory

This dissertation is accepted by the Graduate School

Charles Taber
Dean of the Graduate School

Abstract of the Dissertation

Dynamics of Alcohol and Ketone Photooxidation Reactions on TiO_2(110)

by

Matthew D. Kershis

Doctor of Philosophy

in

Chemistry

Stony Brook University

2016

Titanium dioxide (TiO_2) has attracted significant interest over the years as a photocatalyst for the photooxidation of organic compounds. This type of chemistry finds numerous practical applications in areas such as environmental remediation and self-cleaning coatings. The work described herein employs pump-probe laser techniques to study the photooxidation dynamics of acetone, butanone, ethanol and 2-propanol over a model TiO_2(110) photocatalyst. Studies of model catalysts under ideal, ultra-high vacuum (UHV) conditions allow for detailed, mechanistic information to be obtained. A common characteristic of all these photooxidation reactions is that they proceed by ejection of methyl or ethyl (in the case of butanone) radicals from the surface. The pump-probe laser techniques used here provide information regarding the kinetic energy and internal state distributions of these radical species.

Previous studies of acetone photooxidation have shown that this molecule, when coadsorbed with molecular oxygen on a TiO_2 surface, forms a diolate species that can photooxidize to produce adsorbed acetate and gas-phase methyl radicals. These radicals desorb with a kinetic energy distribution characterized by two channels. In an attempt to better understand this bimodal distribution, state-resolved measurements were made of the methyl radical ν_2 "umbrella mode" vibration. It was found that methyl radicals which desorbed promptly from the surface ($E_{kin} = 0.15$ eV) had a cold vibrational distribution in this mode which was characterized by a $T_{vib} = 151 \pm 15$ K. While this distribution was colder than that measured in the gas phase for acetone photodissociation, the rotational energy distribution was comparable to that obtained in gas-phase measurements ($T_{rot} = 325 \pm 25$ K). Kinetic energy distributions taken at $\nu_2(v = 0)$ and $\nu_2(v = 1)$ show that vibrationally excited methyl radicals have ~ 35 meV less energy overall than those which are not. Together these results suggest a late transition state for acetone photooxidation and show that vibrationally excited methyl radicals have less energy in the form of kinetic energy.

Butanone photooxidation on TiO_2 has been previously shown to proceed via ejection of

both methyl and ethyl radicals into vacuum. Early experiments on this system using mass spectrometry indicated that butanone photooxidation may also produce secondary organic products. Subsequent measurements of the kinetic energy of these various products revealed that these products are in fact fragments of desorbing ethyl radicals. Work presented here used this system as a test case to demonstrate a technique called pixel-imaging mass spectrometry (PImMS) in particular for surface photochemistry experiments. When used in conjunction with velocity map imaging, this technique can help distinguish primary photoproducts from fragments based on differences in angular distributions between these species. When compared with kinetic energy measurements and conventional imaging techniques, this technique is far less time consuming and maximizes the amount of data that can be obtained under identical experimental conditions.

The photooxidation of ethanol and 2-propanol was also studied in an effort to make mechanistic connections between alcohol and aldehyde/ketone photooxidation. While previous studies of these molecules has shown that the first step in photooxidation is the photodehydrogenation to either acetaldehyde or acetone. In this work, it is demonstrated that these reactions also proceed via methyl radical ejection into vacuum. By comparing the kinetic energy distributions measured here with those previously obtained for acetaldehyde and acetone photooxidation, it is concluded that these radicals are produced via the photooxidation of the initial aldehyde/ketone photoproduct.

Finally, details for the design of a new time-of-flight spectrometer for ultrafast imaging studies is presented. This instrument is designed to resolve the angular distributions of desorbing molecules by the velocity map imaging technique. The performance of the detector will be demonstrated on the basis of computer simulations as well as experimental data for the gas-phase photolysis of methyl iodide.

Dedication Page

I would like to dedicate this work to my parents, Michael and Karen Kershis. Their constant love and support through the years has made this all possible. This work is as much their achievement as it is mine.

Table of Contents

1 Introduction **1**

2 Experimental **10**
2.1 Ultra-high vacuum surface science chamber 10
2.2 Sample preparation 11
2.3 Pump-probe laser system 11
2.4 Ionization schemes 12
2.5 Velocity-map imaging detector 14

3 Dynamics of acetone photooxidation on TiO_2(110): State-resolved measurements of methyl photoproducts **28**
3.1 Introduction 28
3.2 Experimental 31
3.3 Results 32
3.3.1 Rotational Energy Distributions 32
3.3.2 Vibrational population in the ν_2 "umbrella mode" 35
3.3.3 Vibrationally resolved energy distributions 36
3.4 Discussion 37
3.5 Conclusion 41

4 Exploring surface photoreaction dynamics using pixel imaging mass spectrometry (PImMS) **49**
4.1 Introduction 49
4.2 Experimental 51
4.2.1 PImMS Camera 52
4.3 Results 52
4.4 Discussion 55
4.5 Conclusions 58

5 Photooxidation of ethanol and 2-propanol on TiO_2(110): evidence for methyl radical ejection **64**
5.1 Introduction 64
5.2 Experimental 65
5.3 Results 65
5.3.1 TPD and photodesorption results 65
5.3.2 Methyl radical kinetic energy distributions 69
5.4 Discussion 71
5.5 Conclusion 73

6 Design of an Imaging TOF-MS for Ultrafast Surface Studies **80**
6.1 Construction details 80
6.2 Computer simulations of the detector 82
6.3 Preliminary Results - CH_3I photodissociation 83

7 Summary and Future Directions **93**

8 References **96**

List of Figures

1.1 Diagram illustrating photocatalytic oxidation on TiO_2 surfaces. The double arrow between charge carriers indicates that charges can recombine before having the opportunity to interact with adsorbed molecules. The white curved arrows indicate diffusion of charge carriers to the surface where they can undergo charge transfer with adsorbates. Ideally, organic molecules will undergo complete photooxidation to CO_2 and H_2O although this is not always observed under UHV conditions. 6

1.2 Model of the $TiO_2(110)$ surface. A common defect (which is of importance in this work) is to having missing bridging oxygen atoms on the surface. Reproduced from Pang et al. [1] with permission of the Royal Society of Chemistry. 7

1.3 TiO_2 band diagram before and after adsorption of an electronegative molecule on the surface. As an n-type semiconductor TiO_2 already exhibits a small degree of upward band bending due to the excess negative charge on the surface. Addition of an electronegative molecule such as O_2 exaggerates this effect further leading to an additional upward shift in the bands (ΔE_{bb}). . . . 8

1.4 Mechanism of ketone photooxidation on $TiO_2(110)$. In the case of acetone, R = CH_3. 9

2.1 Upper level of the surface photochemistry chamber. This level was typically used for sample cleaning and TPD measurements. The Auger spectrometer (AES) that is shown can be replaced with a LEED depending upon the experimental needs. 19

2.2 Lower level of the surface photochemistry chamber and attached VUV generation chamber. The dotted line shows the alternate probe laser beam path for the $(2+1)$ REMPI ionization schemes. 20

2.3 A three-dimensional rendering of the sample holder used in these experiments. 21

2.4 Diagrams showing the different ionization detection schemes used in this work. The generation of VUV photons is illustrated in the left hand panel along with relevant ionization potentials for some of the molecular species studied in this work. The REMPI schemes for deuterated methyl radical detection are shown in the right hand panel along with the relevant wavelengths coorresponding to the 0_0^0 bands of the $3p_z$ (333.9 nm) and $4p_z$ (286.5 nm) Rydberg states. For the alcohol experiments CH_3 radicals were detected using the 0_0^0 band of the $4p_z$ Rydberg state occurring at 286.3 nm 22

2.5 Drawing of the velocity map imaging time of flight spectrometer. The TiO_2 sample is approximately 29 mm from the ionization region between V_1 and V_2. 23

2.6 Graphical display from SIMION showing the vector velocity focusing capability of the imaging detector. The group of trajectories shown in blue are ions desorbing at 0° with respect to the surface normal whereas those trajectories shown in red are ions desorbing at ±20° with respect to the surface normal. . 24

2.7 Cross-sections of the imaging detector with the crystal in place to better illustrate the finite angular acceptance angle of the detector. Drawing (a) shows the horizontal acceptance angle and (b) shows the vertical acceptance angle. 25

2.8 Graph (a) shows a comparison between the vertical and horizontal detector functions, graph (b) shows a simulated ion image based upon our known detection geometry. The black circle represents the phosphor screen boundary for scaling purposes. 26
2.9 An image of the phosphor screen used to establish a calibration between pixel location and physical distance (in mm) across the detector. 27
3.1 A typical depletion curve, showing the methyl radical signal as a function of irradiation time, which is used to correct individual rotational scans for the loss of signal as a result of the surface photoreaction. Open circles denote experimental data while the solid curve represents a four parameter, biexponential fit to the data. Such complex depletion kinetics are commonly observed for substrate-mediated photochemistry on TiO_2 surfaces. 42
3.2 Rotationally resolved REMPI spectrum of 0.15 eV methyl radicals via the 0_0^0 transition of the $4p_Z$ Rydberg state. The top trace is the experimental data and the bottom trace is a PGOPHER simulation at $T_R = 325 \pm 25$ K which has been vertically offset for clarity. 43
3.3 $(2+1)$ REMPI spectrum $({}^2A_2''(3p_Z) \leftarrow\leftarrow \tilde{X}^2A_2'')$ of methyl radicals of the fast channel. The spectrum shows little vibrational excitation for radicals in this channel. Data were recorded using a 21 μs laser delay and a 3 cm^{-1} step size and are not corrected for variations in ionization laser intensity. 44
3.4 Vibrationally resolved depletion curves for methyl radicals of the fast channel. Both datasets have been corrected for differences in ionization laser power and the $\nu = 1$ set has been multiplied by 20 for ease of comparison. For both measurements, the prepared sample was irradiated using a photon flux of $\sim 2.3 \times 10^{12}$ photons$\cdot cm^{-2} \cdot s^{-1}$. 45
3.5 (a) Energy distribution for methyl radicals in the $\nu_2(\nu = 0)$ vibrational state and (b) in the $\nu_2(\nu = 1)$. The experimental data are shown as open circles, whereas dashed curves represent fits for the individual kinetic energy components. The solid curve represents the sum of these two fits. 46
3.6 Combined fits as a function of vibrational state. Curves are vertically offset for clarity and the mean fast-channel energies are marked for comparison purposes. 47
4.1 A view of the experimental setup showing the necessary modifications required to accommodate the PImMS camera. 59
4.2 Time-of-flight mass spectra taken for both (a) slow and (b) fast channels. Below each mass spectrum is the data in its 3D form where the horizontal axis represents time and the vertical axis represents the detector plane with units of pixels. The 3D images have been rotated slightly about the time axis to better illustrate the ion clouds. Thus, the vertical axes do not correspond to single detector axis (i.e., x or y) but rather some arbitrary combination of the two. 60
4.3 Two-dimensional images of masses originating from ethyl radical and its fragments. Panel (a) shows images of(from left to right) ethyl radical (mass 29), mass 28, and mass 27 taken at a 59 μs laser delay. Panel (b) shows images of the same three masses but at a 24.6 μs laser delay. 61

4.4 Horizontal cross sections taken for images of masses 29-27 (left to right) at (a) 59 μs laser delay and (b) 24.6 μs laser delay. For data taken at the longer delay, the degree of fragmentation for ethyl radical is quite severe and there is signal which falls outside of the limits imposed by our detector function. Fragmentation does not appear to be as severe for data taken at the shorter delay, although there is a clear broadening of the distribution for masses 28 and 27. 62
4.5 Angular distributions of ethyl radical desorption for the (a) slow and (b) fast channels along with $\cos^n(\theta)$ fits to the data. For the slow channel $n = 39.5$ and for the fast channel $n = 39.0$. The angular distribution of ethyl radicals is essentially the same for both kinetic energies studied in this work. 63
5.1 Ethanol TPD spectra showing signal for 29 amu for (a) no UV irradiation, (b) irradiation of ethanol in the absence of oxygen (c) irradiation of ethanol in 5×10^{-8} Torr of O_2. For curves b and c, the sample was irradiated for 5 min using a photon flux of 2.6×10^{16} photons$\cdot s^{-1} \cdot cm^{-2}$. For all three experiments, the ethanol coverage is estimated to be ~ 0.8 ML. Spectra are vertically offset for clarity. 74
5.2 Methyl radical depletion measurements taken at (a) 100 K, (b) 250 K, (c) 300 K and (d) 100 K without oxygen. These samples were irradiated using a photon flux of 2.6×10^{16} photons$\cdot s^{-1} \cdot cm^{-2}$, in the case of (a)-(c), a background oxygen atmosphere of 5×10^{-8} Torr. Individual curves are vertically offset for clarity. 75
5.3 2-Propanol TPD spectra showing signal for m/z = 21. Spectrum (a) represents a 2-propanol dose of ~ 0.6 ML in the absence of UV irradiation while spectrum (b) represents the same dose of 2-propanol irradiated for 10 min in 5×10^{-8} Torr of O_2 using a photon flux of 2.6×10^{16} photons$\cdot s^{-1} \cdot cm^{-2}$ 76
5.4 Methyl radical kinetic energy distributions for (a) ethanol and (b) 2-propanol. Solid points represent experimental data, dashed lines represent fits for fast and slow channels and the solid trace represents the overall fit. 77
5.5 Mechanism of ethanol and 2-propanol photooxidation on $TiO_2(110)$. R = H in the case of ethanol photooxidation and R = CH_3 in the case of 2-propanol photooxidation. 78
6.1 Photograph of the fully assembled detector prior to installation on the vacuum system. 86
6.2 Two dimensional cross section of the ion imaging optics. This design contains 11 tunable lenses plus a final lens that is held at ground potential. Carefully positioned holes in V_4 and V_5 allow for co-linear pump and probe laser beams to access the surface at an angle of $\sim 45^\circ$ with respect to the surface normal. 87
6.3 Circuit diagram of the voltage divider for the ion optics. Instead of having 11 individually tunable lenses, the ion optics were divided into two regions with two separate dividing circuits. This allows for easy adjustment of the V_1:V_6 ratio which in turn determines the quality of the image focus. The voltages for each lens are given in terms of either V_1 or V_6 and for VMI experiments typical voltages used are 1100 V for V_1 and 800 V for V_6. The crystal is biased separately at a voltage of $7 - 9$ V higher than V_1. 88

6.4 Computer representation of the imaging detector produced with the help of SIMION 8.0 software. The red contours show the electric field potentials inside the detector and the black, green and blue traces represent ion trajectories for methyl radicals desorbing at angles of 0, 30 and 80 degrees with respect to the surface normal. Ions are flown beginning at the crystal surface across an distance of ± 2.5 mm from the center of the crystal and are focused in groups at the detector depending upon their initial trajectory 89
6.5 Graph showing the initial ion kinetic energy as a function of final position on the MCP detector. This calculation was performed for methyl radicals moving in a trajectory parallel to the MCP and so the energy is simply the kinetic energy along this direction. This is intended to simulate methyl radical ejection following CH_3I photolysis where the photolysis laser polarization vector is also parallel to the detector plane. 90
6.6 Velocity mapped image of methyl radicals following dissociation of CH_3I. The raw image is shown on the left and the inverse Abel-transformed image is shown on the right. The inverse Abel transformation is necessary to extract the correct energy distribution from the raw image which is a 2D projection of a 3D ion cloud. Dark blue spots in the transformed image are due to dead spots in the detector. The dissociation of CH_3I and ionization of methyl radicals was performed by a single laser tuned to 286.3 nm which represents the 0_0^0 band of the $4p_z$ Rydberg state of CH_3. Hence following a one photon absorption/dissociation step, methyl radicals were ionized through a $2 + 1$ REMPI process. 91
6.7 Kinetic energy distribution for methyl radicals following CH_3I photolysis. The data was extracted from the transformed image and represents the summed signal over a 2π integration about the image center. Experimental data is shown as a blue trace while the data in red is taken from Eppink and Parker.[2] 92

List of Tables

3.1 Values showing the mean energies for energy distributions taken for each vibrational state. Also shown are the ratios showing the relative population of methyl radicals in the fast and slow channels. Energy values are in units of eV and are accurate to within $\sim 6\%$ of the quoted value 48

5.1 Mean kinetic energies for desorbing methyl radicals produced following ethanol and 2-propanol photooxidation. Values are in units of eV and have an estimated uncertainty of 10%. This uncertainty is derived from the error in measuring the neutral flight distance between the surface and ionization region of the TOF-MS 79

List of Abbreviations

2PPE - two-photon photoemission

Au-TiO_2 - TiO_2-supported gold nanoparticles

CMOS - complementary metal-oxide-semiconductor

DCM - [2-[2-[4-(dimethylamino)phenyl]ethenyl]-6-methyl-4H- pyran-4-ylidene]-propanedinitrile

DEA - dissociative electron attachment

DFT - density functional theory

HREELS - high resolution electron energy loss spectroscopy

IRAS - infrared reflection-absorption spectroscopy

KDP - potassium dihydrogen phosphate

LDS 698 - [2-[4-[4-(dimethylamino)phenyl]-1,3-butadienyl]-1-ethylpyridinium monoperchlorate

MCP - microchannel plate

ML - monolayer

Nd:YAG - neodymium-doped yttrium aluminum garnet

OFHC - oxygen-free high-conductivity

OPO - optical parametric oscillator

PImMS - pixel imaging mass spectrometry

PMT - photomultiplier tube

PVC - polyvinyl chloride

QMS - quadrupole mass spectrometer

REMPI - resonance enhanced multiphoton ionization

SHG - second-harmonic generation

THG - third-harmonic generation

TOF-MS - time-of-flight mass spectrometer

TPD - temperature programmed desorption

TiO_2 - titanium dioxide

UHV - ultrahigh vacuum

UV - ultraviolet

VMI - velocity map imaging

VUV - vacuum ultraviolet

Acknowledgements

I would first like to thank my advisor, Dr. Michael White for his support and encouragement over the past five years. Everything I've learned about being a good scientist has been a direct result of his careful guidance and mentorship. I would also like to thank Dr. Daniel Wilson for teaching me the "ins and outs" of the various experimental techniques I have used throughout the course of my graduate research. I am also grateful to my committee members, Dr. Trevor Sears, Dr. José Rodriguez and Dr. Nick Camillone for their guidance and for the constructive criticism they have provided for my work over the years. I am grateful to my group members, both past and present, for making the lab an enjoyable place to work. In particular I am grateful to Dr. John Lofaro, Dr. Robert Palomino and Joe Magee for their years of friendship and for the many times they've helped me in the lab. I am particularly grateful to Amanda Muraca for being an excellent partner on this project and for the hard work she has already put in to bring this project to the next level.

I would also like to acknowledge the PImMS collaboration at the University of Oxford for lending us a camera to use in our imaging experiments. In particular, I would like to thank Dr. Andrei Nomerotski and Jaya John John for personally bringing the camera to our lab and training us in its use so that our experiments could be successful.

There are many others at Stony Brook and Brookhaven Lab who also deserve a big thank you: Katherine Hughes for always keeping me on track with important dates and deadlines, Jean Petterson and Linda Sallustio for helping me navigate various administrative tasks at BNL, Jim Anselmini, Jeff Hoogsteden and the BNL Heavy Machine Shop for their talent and skill in helping me construct (and repair) various pieces of scientific equipment, and Mahendra Kahanda for his computer expertise. I am also grateful to the SUNY Research Foundation and U.S. Department of Energy for providing financial support for this work.

Lastly I would like to thank Mr. Anthony Nobre, my high school chemistry teacher, for encouraging me to pursue a career in science. The time spent in his classroom has had a lasting impact on me and is what motivated me to study chemistry in the first place.

1 Introduction

Titanium dioxide (TiO_2) has generated a lot of activity in the research community over the past few decades. For example, a recent search on Thomson-Reuters Web of Science database[3] for the topic "TiO_2" returned a list of over 136,000 results. In particular, since Fujishima and Honda first demonstrated the potential of TiO_2 for water splitting,[4] a lot of research has been done on the photocatalytic properties of this material. The result of this effort has led to the development of TiO_2-based technologies such as self-cleaning and self-sterilizing surfaces, anti-fogging surfaces as well as air and water purification systems.[5]

The core physical process behind all of these technologies is the photooxidation of organic molecules on TiO_2 surfaces. Therefore, in order to understand how these technologies work at a fundamental level, detailed studies of catalytic photooxidation are needed. To begin, it is important to appreciate how TiO_2 works as a photocatalyst. An overview of TiO_2 photocatalysis is shown schematically in Fig. 1.1. TiO_2 is a semiconductor material which possesses a band gap of 3.0 eV or 3.2 eV for the rutile and anatase phases respectively.[6] This means that when TiO_2 absorbs UV light below 400 nm, an electron from the valence band is promoted to the conduction band leaving behind a hole in the valence band. Once these electron-hole pairs are created they can undergo additional processes such as recombination, diffusion to the surface, diffusion to trap sites, and charge transfer to molecules which may be adsorbed on the surface.[7] In the context of photocatalytic chemistry, charge-carrier diffusion and transfer are arguably the two most desirable processes. Reactions which proceed by electron transfer from TiO_2 to the adsorbate should intuitively be thought of as photoreduction processes whereas those proceeding by electron transfer from the adsorbate to TiO_2 should be considered to be photooxidation reactions.

As is the case in this work and in many other fundamental studies, the rutile $TiO_2(110)$ single crystal surface is an ideal candidate for basic research into photocatalytic reaction mechanisms. The $TiO_2(110)$ surface is well-studied in the literature because it is easily obtained and prepared and exhibits high thermodynamic stability.[8] A model of this surface

is shown in Fig. 1.2. This surface is characterized by rows of oxygen atoms (termed bridging oxygen atoms and abbreviated as O_{br}) alternating with troughs of Ti^{4+} atoms. It is common for these surfaces to have point defects in the form of missing O_{br} atoms which leave bridging oxygen vacancies (O_v) and Ti^{3+} sites.[6] These additional electrons occupy states just below the conduction band and gives the sample character of an n-type semiconductor. As will be explained further, the role of oxygen vacancies (as well as the addition of co-adsorbed oxygen) is of critical importance in photooxidation chemistry on TiO_2.

It is important to understand the role of oxygen vacancies as well as the photochemistry of adsorbed oxygen on TiO_2 as both phenomena are central to understanding photooxidation of small organic molecules on TiO_2. Under ideal conditions (single crystal substrate, ultra-high vacuum conditions), oxygen molecules are known to adsorb on reduced TiO_2 surfaces at oxygen vacancy sites.[9,10] These molecules adopt a formal negative charge due to the excess electrons at the vacancy sites. Recent work by Petrik and Kimmel has shown that each oxygen vacancy can accommodate up to two O_2 molecules.[11] If only one molecule is adsorbed in a vacancy, it adsorbs as ${O_2}^{2-}$ whereas if two molecules are adsorbed they each adsorb as ${O_2}^{-}$. Once adsorbed, oxygen molecules are stable unless the surface is heated past ~ 400 K at which point they will undergo thermal desorption.[10] It is typical for one of the molecules to desorb while the other dissociates such that one O atom fills the vacancy while the other is deposited on the surface nearby. Oxygen can also photodesorb if the surface is irradiated with light ≥ 3.0 eV as originally observed by Yates and co-workers.[9] It is believed that oxygen photodesorption is a hole-mediated process where interaction between the hole and the negatively charged oxygen molecule produces a neutral oxygen molecule that is free to desorb.[11] It is also believed that oxygen molecules can interact with electrons which result in O_2 dissociation and the formation of O-adatoms on the surface.[11]

In addition to the many chemical transformations that oxygen can undergo on TiO_2 surfaces, the presence of adsorbed oxygen molecules is important for promoting hole-mediated photoreactions of co-adsorbed species. One explanation of this behavior is that oxygen pro-

motes such reactions through a "band-bending" mechanism.[12,13] This mechanism can be explained due to the fact that as an n-type semiconductor, reduced TiO_2 has excess charge on the surface in the form of Ti^{3+} sites at oxygen vacancies. Upon adsorption of molecular oxygen, this excess charge is transferred to the oxygen molecules and the result is an upward bending of the TiO_2 valence and conduction bands.[13] A diagram illustrating this phenomenon is given in Fig. 1.3 for the case of an electronegative molecule adsorbed on TiO_2. When electron hole pairs are created the holes are more readily drawn toward the TiO_2 surface as a result of this excess negative charge. Since there is an increased probability for these holes to travel toward the surface, there is an enhancement of hole-mediated photoreactions. Zhang and Yates demonstrated this phenomenon by studying the photodesorption of $^{18}O_2$ in the presence of either $^{16}O_2$ or Cl_2 co-adsorbates.[12] Since oxygen and chlorine are both electron acceptors, it was found that their presence on the surface enhanced the photodesorption yield of $^{18}O_2$ by withdrawing negative charge from the surface and thus enhancing the hole transport from the bulk to the surface.

While band-bending has been shown to be an important mechanism for certain hole-mediated photoreactions, oxygen has also been shown to promote photooxidation by forming unique photoactive compounds with organic adsorbates.[6] In particular this has been observed in ketone photooxidation which is a major subject of this dissertation.[14–19] Experiments conducted by Henderson have shown that acetone photooxidation requires the co-adsorption of oxygen on the TiO_2 surface.[14] Following exposure to oxygen and UV light, Henderson observed that acetone photooxidation proceeds via ejection of a methyl radical from the surface leaving behind a surface-bound acetate species (see Fig. 1.4). This mechanism was rationalized via a two-step process where an acetone-diolate complex was formed in the first step by addition of an adsorbed oxygen atom to the carbonyl carbon atom of the acetone molecule. This diolate complex, which represents the photoactive species, decomposes in the second step via methyl radical loss. Structural evidence for this diolate complex has been obtained through both HREELs and IRAS measurements which show the presence of this

molecule on the surface following the co-adsorption of acetone and oxygen.[18,20]

A key finding in the above experiments is that acetone photooxidation is negligible without the presence of oxygen and that the acetate photoproduct does not undergo further oxidation to CO_2 and H_2O under the conditions studied. A possible explanation for this observation was given in a recent paper by Wilson and co-workers where the authors suggested that differences in the alignments of molecular HOMO levels with respect to the TiO_2 valence band could explain these differences in reactivity.[15] The hypothesis of these authors is that the acetone HOMO level lies to far below the TiO_2 valence band maximum for efficient electron transfer to occur to the thermalized holes. On the other hand, it is hypothesized that the once the diolate is formed, its HOMO lies much closer to valence band maximum so charge transfer between the diolate and valence band holes can occur. The poor reactivity of acetate is also attributed to poor overlap between the HOMO and valence band. Since it should be expected that proper orbital overlap is necessary for efficient photocatalysis to occur, this explanation appears to be highly plausible. Further experimental and theoretical data (i.e. photoemission experiments and DFT calculations) is needed to confirm that this hypothesis is accurate.

In the sections that follow, experimental results for ketone and alcohol photooxidation reactions on TiO_2 are presented. In particular this dissertation focuses on three separate but closely related topics: understanding acetone photooxidation through spectroscopic measurements of methyl radical photoproducts, understanding butanone photooxidation through the use of advanced imaging techniques and understanding the ethanol and isopropanol photooxidation mechanisms through the use state-resolved laser probes. These experiments were all completed using single crystal TiO_2 samples under UHV conditions using techniques which enable the detailed study of primary reaction steps. All of the molecules studied represent common environmental pollutants and so understanding of their fundamental, photocatalytic chemistry is of relevant interest to those interested in environmental remediation by photocatalysis. This work concludes with a section looking toward the future and toward

relevant experiments that remain to be done.

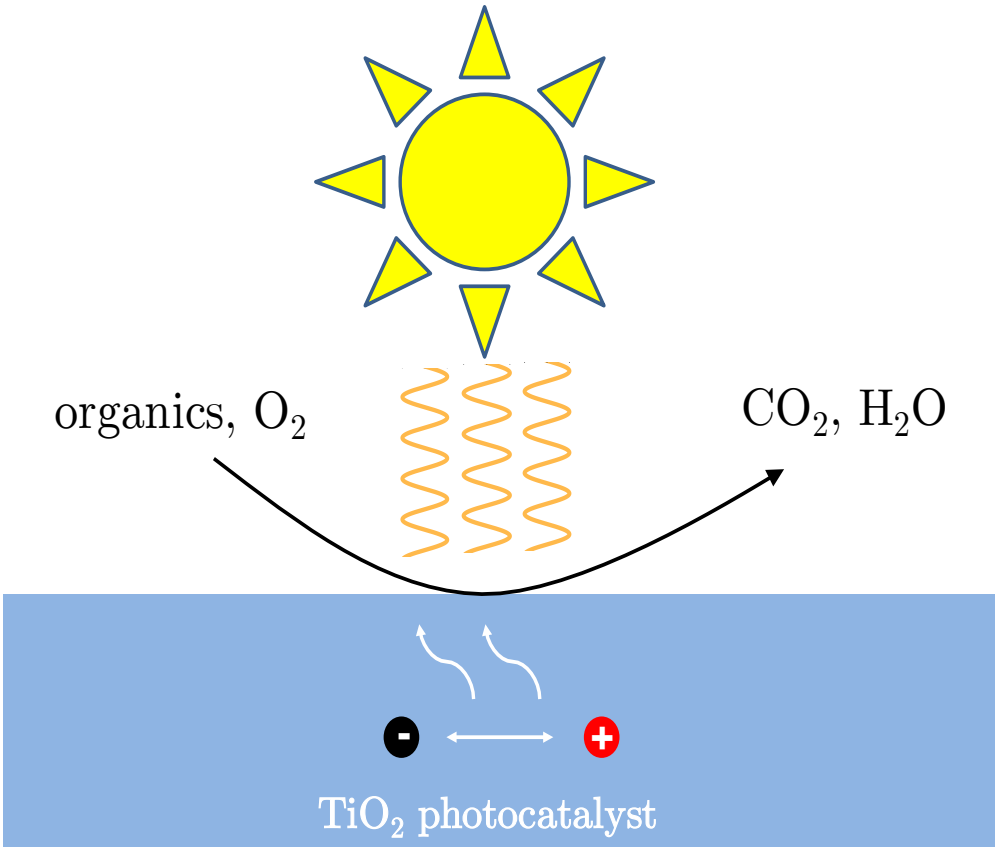

Figure 1.1: Diagram illustrating photocatalytic oxidation on TiO_2 surfaces. The double arrow between charge carriers indicates that charges can recombine before having the opportunity to interact with adsorbed molecules. The white curved arrows indicate diffusion of charge carriers to the surface where they can undergo charge transfer with adsorbates. Ideally, organic molecules will undergo complete photooxidation to CO_2 and H_2O although this is not always observed under UHV conditions.

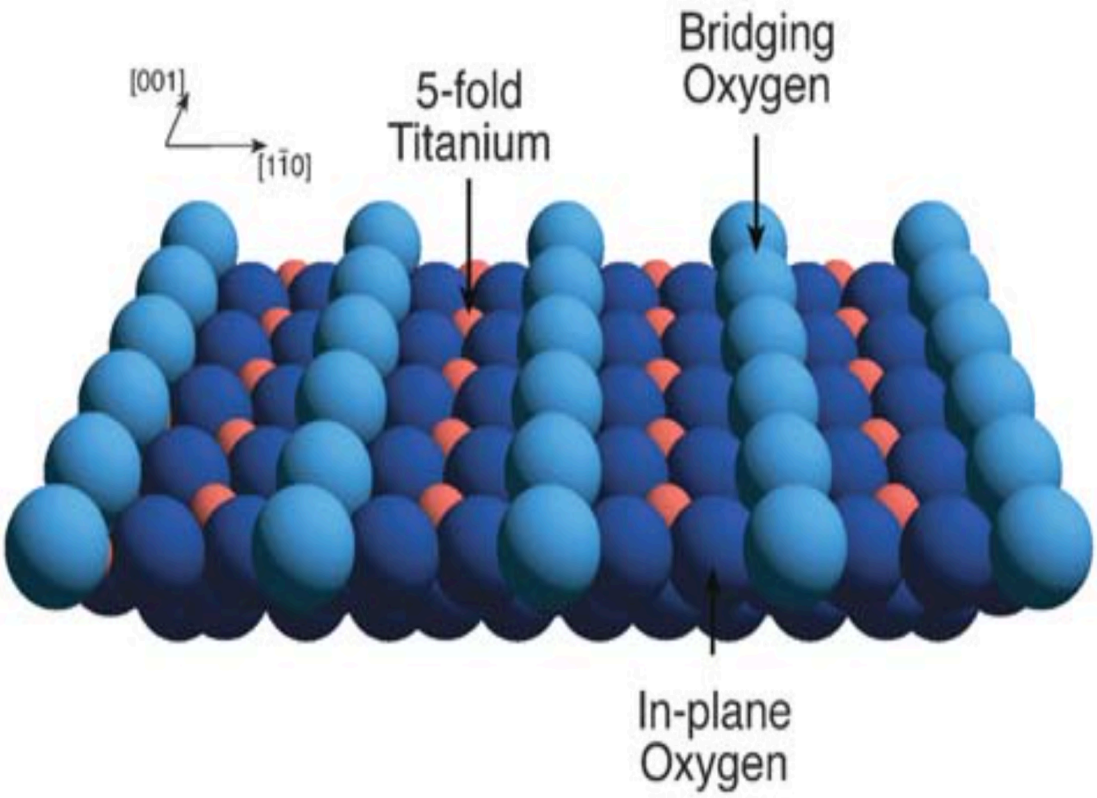

Figure 1.2: Model of the TiO_2(110) surface. A common defect (which is of importance in this work) is to having missing bridging oxygen atoms on the surface. Reproduced from Pang et al. [1] with permission of the Royal Society of Chemistry.

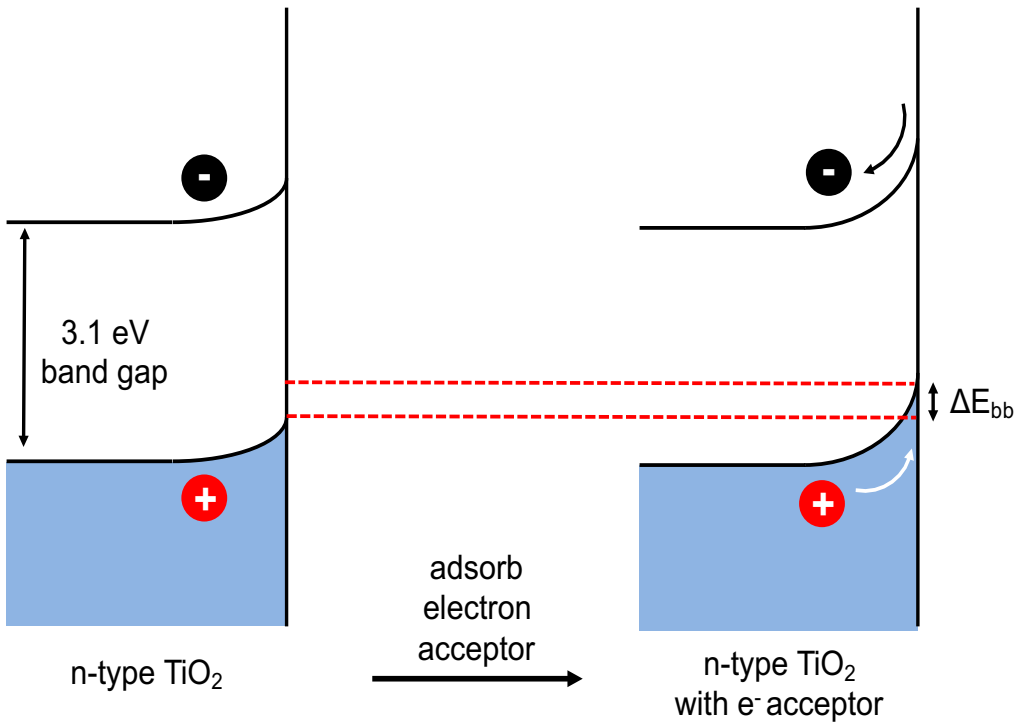

Figure 1.3: TiO_2 band diagram before and after adsorption of an electronegative molecule on the surface. As an n-type semiconductor TiO_2 already exhibits a small degree of upward band bending due to the excess negative charge on the surface. Addition of an electronegative molecule such as O_2 exaggerates this effect further leading to an additional upward shift in the bands (ΔE_{bb}).

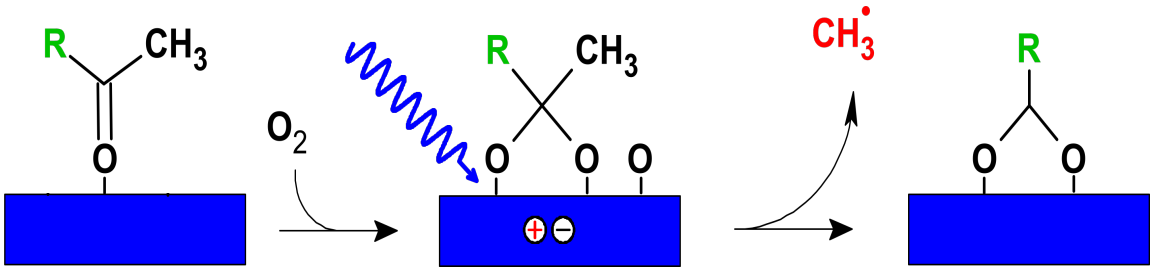

Figure 1.4: Mechanism of ketone photooxidation on $TiO_2(110)$. In the case of acetone, R = CH_3.

2 Experimental

2.1 Ultra-high vacuum surface science chamber

The ultra-high vacuum (UHV) chamber that was used for the experiments presented here was composed of two separate levels as well as a windowless vacuum ultraviolet (VUV) radiation source used for single photon ionization of desorbing photoproducts. the apparatus is composed of a two-tiered chamber with a base pressure of $\sim 2 \times 10^{-10}$ Torr, as well as a windowless vacuum-ultraviolet (VUV) radiation source which is connected to the main chamber via a differentially pumped capillary tube. The VUV chamber will be discussed further in the section on detection schemes. Drawings of the top and bottom levels are shown in Figures 2.1 and 2.2 respectively.

The top tier of the main chamber contains instrumentation for surface preparation and characterization including an ion gun (NGI3000-SE, LK Technologies), quadrupole mass spectrometer (Hiden Analytical) for temperature programmed desorption (TPD) measurements, and a low-energy electron diffraction instrument (LEED; Princeton Research). The bottom tier of this chamber contains a home-built time-of-flight mass spectrometer (TOF-MS) which is used for photochemistry measurements. The crystal is transferred between the two levels via a liquid nitrogen cooled manipulator capable of x,y,z translation and azimuthal rotation.

Additionally, the chamber is equipped with a gas inlet system that is used to transfer gaseous molecules to the experimental chamber. This system can accept connections from compressed gas cylinders as well as from special glass vials containing liquid samples whose vapor can be admitted to the system. Each level of the chamber contains a directional doser tube (1 cm o.d. with a pinhole aperture) that can be placed within $\sim 1 - 2$ mm of the surface in order to precisely expose the surface to molecules of interest.

2.2 Sample preparation

The rutile $TiO_2(110)$ crystal ($10 \times 10 \times 2$ mm, CrysTec) is oriented with respect to the laboratory frame such that the [001] direction is parallel to the floor. A three-dimensional rendering of the sample mount used in these experiments is shown in Figure 2.3. In this design, the crystal sits upon a button heater with a piece of Au foil sandwiched between the crystal and heater for enhanced thermal conductivity. The heater is enclosed by a Mo support ring and the crystal is held firmly in place with a pair of Ta clips. The sample temperature is monitored via a type-K thermocouple which is attached to the crystal using high-temperature cement (Omegabond 600). Initial surface preparation involved exposing the fully oxidized sample to repeated cycles of Ar^+ sputtering (2 keV) at 800 K and annealing at 850 K. After this treatment, the crystal turned a dark blue color, which is strongly indicative of bulk reduction.[21] Following the initial reduction, the surface was routinely prepared by low-energy sputtering (0.5 keV, 10 min) and annealing (850 K, 30 min). The surface was also cleaned in between photochemistry experiments by annealing the sample at 850 K for 10 min. This also served to replenish oxygen vacancies which are filled during the course of photooxidation experiments as such vacancies are necessary for oxygen chemisorption.[10]

2.3 Pump-probe laser system

Photochemistry measurements were carried out using pump-probe laser techniques in conjunction with TOF-MS detection of desorbing species. Photochemistry was induced at the surface using 335 nm (3.7 eV) photons which were generated by doubling the output of a Nd:YAG pumped dye laser (Spectra-Physics GCR-190, Sirah Precision Scan, DCM/LDS 698 dyes in methanol). For some of the measurements presented here, a Nd:YAG-pumped optical parametric oscillator (OPO) system (Spectra-Physics Lab 150/GWU-Lasertechnik versaScan/uvScan) was used to generate 335 nm photons. Prior to entering the chamber, the beam was fixed at a diameter of $\sim$0.7 cm and upon striking the crystal at a 45° angle, resulted in an elliptical irradiation area on the crystal face of 0.5 cm^2. A pair of Glan-

Thompson polarizers (Lambrecht) served to control photon fluence as well as to establish p-polarized light relative to the crystal face. A mechanical shutter positioned between the second polarizer and the chamber was used to precisely control the passage of light to the crystal face.

Calibrated neutral-density filters were used to further control irradiation fluence which helped ensure that product depletion was relatively slow during a typical experimental time frame (5−10 min). Generally speaking, the photon fluence in these experiments was between $10^{11} - 10^{16}$ photons $\cdot$ cm$^{-2}\cdot$ s^{-1} depending on the experimental requirements. As our laser system uses pulsed lasers with a repetition rate of 20 Hz, this fluence represents an average that was calculated by multiplying the average pulse fluence by the repetition rate.

Photoproducts desorbing from the surface were ionized at a known distance (typically 26−29 mm) from the surface using a second laser which was aligned parallel to the surface. Radiation in the ultraviolet region was generated by second-harmonic generation (SHG) of the output (KDP nonlinear crystals, INRAD Autotracker) of a second Nd:YAG pumped dye laser (Spectra-Physics GCR-230, Laser Analytic Systems LDL-20505). Ionization of the photoproducts could then be achieved either through a resonant multiphoton ionization (REMPI) scheme using the UV light, or through a one photon ionization scheme using vacuum-ultraviolet (VUV) light that was generated by focusing the UV light into a jet of N_2 gas. The differences between these two schemes will be discussed below.

2.4 Ionization schemes

A energy diagram illustrating the relevant ionization schemes is given in Fig. 2.4. For methyl radical detection, (as in chapters 3 and 5) a REMPI scheme was preferred whereas a VUV detection scheme was preferred for the butanone photooxidation experiments detailed in chapter 4. In a REMPI process, the output of a focused, pulsed laser interacts with the molecule of interest (methyl radical in this case) and has sufficient intensity to allow for the simultaneous absorption of multiple photons by the molecule. For the process to

be "resonantly enhanced", the sum of the photon energies must correspond to an actual electronic transition within the molecule.[22] In the case of methyl radicals, this transition involves promotion of an electron from the $2p_z$ orbital to the higher-lying $3p_z$ and $4p_z$ orbitals. Once the electron has been promoted to an excited state, an additional photon (or photons) can remove this electron from the molecule and lead to the formation of an ionized species that can be readily detected. Use of a REMPI detection scheme can be advantageous for a couple of reasons. One reason is that this scheme is specific to a particular molecular transition which can be useful when trying to distinguish one product from another. Another reason is that this technique offers great sensitivity as well as the ability to study a molecule's vibrational and rotational structure.

For detecting the ethyl radical and its fragments (chapter 4), a single photon ionization scheme was used by using third-harmonic generation (THG) to produce VUV light from UV light. As shown in Figure 2.2, this is accomplished by focusing the doubled output of the probe dye laser into a N_2 gas jet which results in the production of VUV light.[23] This mixture of UV and VUV photons was then directed through a differentially-pumped capillary light guide and into the main experimental chamber. The differential pumping is necessary to ensure that the high pressures present in the VUV generation chamber do not compromise the integrity of the main chamber vacuum. For the scheme used in these experiments, the dye laser was operated with Rhodamine 590 dye dissolved in methanol which produced visible light at 568.42 nm. This was then doubled via SHG to 284.21 nm and subsequently tripled to produce light at 94.74 nm (13.09 eV). These VUV photons were able to ionize ethyl radicals as well as a number of other species (i.e. CH_3, O_2) simply due to the fact that the energy of these photons exceeded the ionization potential of these species. The ability to ionize multiple species is the main advantage of using VUV ionization as compared to REMPI.

2.5 Velocity-map imaging detector

In these experiments, we used a TOF-MS that is capable of velocity vector focusing, i.e., ions created in the ionization region of the mass spectrometer are directed toward specific points on the MCP detector based upon their initial velocity vector. A key advantage of velocity focusing for surface studies is that the entire sample surface can be irradiated with an unfocused laser beam (pump) without degrading the quality of the downstream ion image. This allows us to keep the laser fluence on the surface to a minimum to avoid surface damage and limit multiphoton effects, while at the same time sampling the maximum number of absorbates for good signal levels. Second, we can use an unfocused VUV laser beam for "universal" neutral product detection, which is particularly advantageous for detecting polyatomic species, e.g., small hydrocarbon radicals, whose excited states might not be known and thereby not readily amenable to detection using resonant multiphoton ionization (REMPI) techniques.[16] Ionization by an unfocused VUV beam provides a large acceptance angle for intercepting neutral products along the VUV beam direction, but results in a line source of ions that would yield a spatially "smeared" angular distribution without vector focusing. Unlike gas-phase experiments, the pump and probe laser beams are not spatially overlapped, since both beams are likely to interact strongly with the substrate and/or adsorbates at the surface. In our design, the spatial separation of the UV pump and VUV probe beams (25-30 mm) is a compromise between optimizing the detection solid angle (short distance) and optimizing the velocity resolution of the pump-probe delay measurements (long distance). Hence, the main information we obtain from our surface velocity focusing experiments is the angular distribution of neutral products within a narrow velocity range as determined by the pump-probe laser delay and angular acceptance of the detector.

To be more specific, the pump-probe delay determines the longitudinal velocity component along the surface normal and parallel to the TOF analyzer axis. Hence, the use of short pump-probe delays results in the ionization of neutrals with higher velocities (larger kinetic energies) within a narrow range determined by the velocity resolution of the neutral

detection step and the angular acceptance of the TOF analyzer. The velocity resolution of the detection step ($\sim 14\%$) is determined primarily by the uncertainty in the neutral flight path, i.e., $\frac{\Delta l}{l}$, where Δl is the length of the ionization region given by the VUV beam diameter (4 mm), and l is the distance from the crystal surface to the ionization region (29.4 mm). The second part of the velocity spread comes from the fact that neutrals entering the TOF analyzer at non-zero angles have transverse velocity components perpendicular to the TOF axis (v_z). Since the pump-probe delay only selects the longitudinal component, this leads to the detection of neutrals with a range of velocities that are simply related to the acceptance angle of the TOF analyzer. With an acceptance angle of $30°$, the spread in neutral velocities in the horizontal direction is $\pm 13\%$ of v_z. In terms of imaging, ions with larger transverse velocity components will be focused further from the center of the detector. Hence, ion images taken for "fast" neutrals corresponding to short pump-probe time delays will appear larger than images taken for "slow" neutrals at longer delays (assuming identical angular distributions). This instrumental dependence of image size on angular spread can be readily accounted for through the calculation of "detector functions" (see below) that allow the angular distributions of desorbing neutrals to be extracted from the images.

SIMION 3D was used to design the ion imaging electrodes that serve as the acceleration and focusing fields for ions born in the interaction region following VUV ionization. A three-dimensional drawing of apparatus is given in Figure 2.5 The main constraint of the design was the use of a line ionization source with a width of $\sim$ 2 cm, which provides a large acceptance solid angle ($\pm 30°$) for reasonably sized focusing elements. A 3D rendering of the accelerating and focusing elements is shown in Figure 2. The large 2 cm ion source in the horizontal direction required the use of thick lens elements with large apertures (V_2 and V_3; 40 mm ID, 16 mm thick) to tailor the electric fields for velocity focusing at the extreme edges. To compensate for the cut-out in the repeller electrode (V_1), which allows the UV beam to strike the crystal, a "horseshoe" electrode (V_4) was added to the back of the repeller plate. The UV light reflected off the crystal was intercepted by a small mirror attached to

the back of the repeller plate (not shown) and directed away from the ion detector. The end of the glass capillary light guide was also enclosed in a metallic tube so that any distortion of the field caused by its insertion near the edge of the ionization region could be roughly compensated by applying a suitable potential (V_5). After being accelerated to 100 eV, ions exiting the final focusing lens (V_3) pass through a grounded grid and enter a field free region before striking the MCP detector. Figure 2.6 shows the results a SIMION trajectory calculation where ions are focussed by their velocity irrespective of their spatial origin. To achieve velocity focusing conditions the following lens voltage ratios were used (relative to V_1): $V_2 = 0.73V_1$, $V_3 = 0.22V_1$, $V_4 = 1.44V_1$ and $V_5 = 0.89V_1$. The overall flight distance from the ionization region to the end of the field free region is 40 cm. All the lens elements were made of oxygen-free high conductivity (OFHC) copper and electroplated with gold.

The detection geometry employed here imposes the limitation that only a subset of neutral trajectories is detected in each surface photodesorption experiment. Specifically, the use of a line ionization source downstream of the surface means that the neutral acceptance angle along the VUV beam axis, referred to as the "horizontal" direction, is larger than the acceptance angle perpendicular to the VUV beam axis, referred to as the "vertical" direction. As shown Figure 2.7, neutrals intersecting a 2 cm length of VUV beam results in a horizontal acceptance angle of about $\pm 30°$, whereas the smaller VUV beam diameter of $\sim$ 4 mm restricts the vertical acceptance angle to $\pm 12°$. These angles are defined relative to the surface normal. As noted earlier, the lens stack was optimized primarily to ensure ion vector focusing along the VUV beam axis (horizontal direction), since the larger range of acceptance angles provides more information on the spatial distribution of the desorbing neutrals.

Since this experiment is designed to measure the angular distribution of photodesorbing species from a surface, it is necessary to relate the final detector position of the ion to the initial trajectory of the neutral photoproduct entering the TOF-MS. As a result of the difference in horizontal and vertical acceptance angles, a cylindrically symmetric angular

distribution about the surface normal (detector axis) will generally appear elliptical with the major axis along the VUV beam direction. The vertical and horizontal collection efficiencies versus initial neutral trajectory angle and linear position on the detector were simulated by SIMION 3D. For the horizontal direction, 1400 ions were flown in 21 groups (1 group per mm across the 2 cm length of the VUV laser beam). The number of ions in each group was determined based on the spread in angle for neutral species intersecting a particular region of the VUV laser and ions were flown in 0.2° increments. An example of these simulations is given in Figure 2.8 where we have shown vertical and horizontal detector probability distributions (as a function of detector position) as well as a two dimensional projection of these functions, giving a simulated image. The simulations were performed for ions of a specific mass (ethyl radical, 29 amu) and initial kinetic energy (0.2 eV), the latter being determined by the pump-probe laser delay and the free flight path prior to ionization (29mm). The numbers of ion "hits" are binned as a function of detector position or equivalently as a function initial angle relative to the surface normal. In Figure 2.8 we have chosen to plot these functions as a function of detector position in mm where 0 mm represents the center of the detector and ±20 mm represents the physical boundaries of the MCP detector (40 mm dia.). The resulting vertical and horizontal functions curves are well described by Gaussian functions and represent the angular distribution of neutrals assuming that all neutral take-off angles are equally probable. It should be emphasized that these distributions are representative of the collection efficiency of the detector in the absence of surface effects. Therefore, in order to derive a surface angular distribution from our images, it is necessary to divide our experimental data by the probability functions we obtain from SIMION simulations. Additionally, our simulations provide a means of relating desorption angle to physical detector position. Converting the experimental data from a function of pixel to a function of detector position is accomplished by recording an image of the entire phosphor screen and determining the number of pixels corresponding to the phosphor screen limits. An example of such an image is given in Figure 2.9. The known diameter of the

phosphor screen (42 mm) and the number of pixels spanning the phosphor image are used to derive a linear fit between pixel number and detector position. It is then possible to use information from the SIMION simulations to plot data as a function desorption angle.

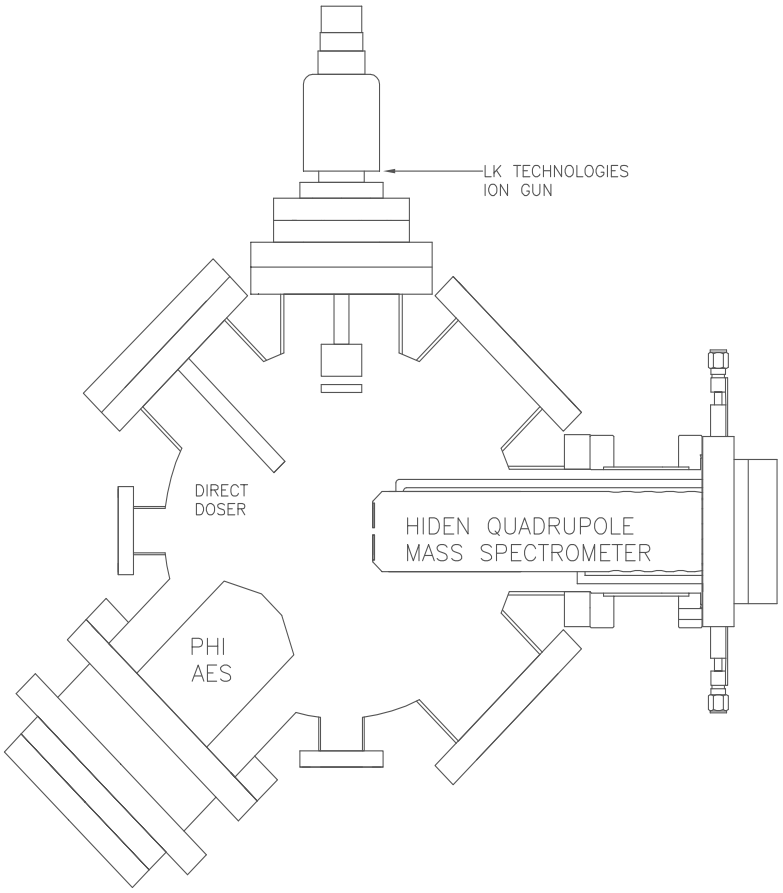

Figure 2.1: Upper level of the surface photochemistry chamber. This level was typically used for sample cleaning and TPD measurements. The Auger spectrometer (AES) that is shown can be replaced with a LEED depending upon the experimental needs.

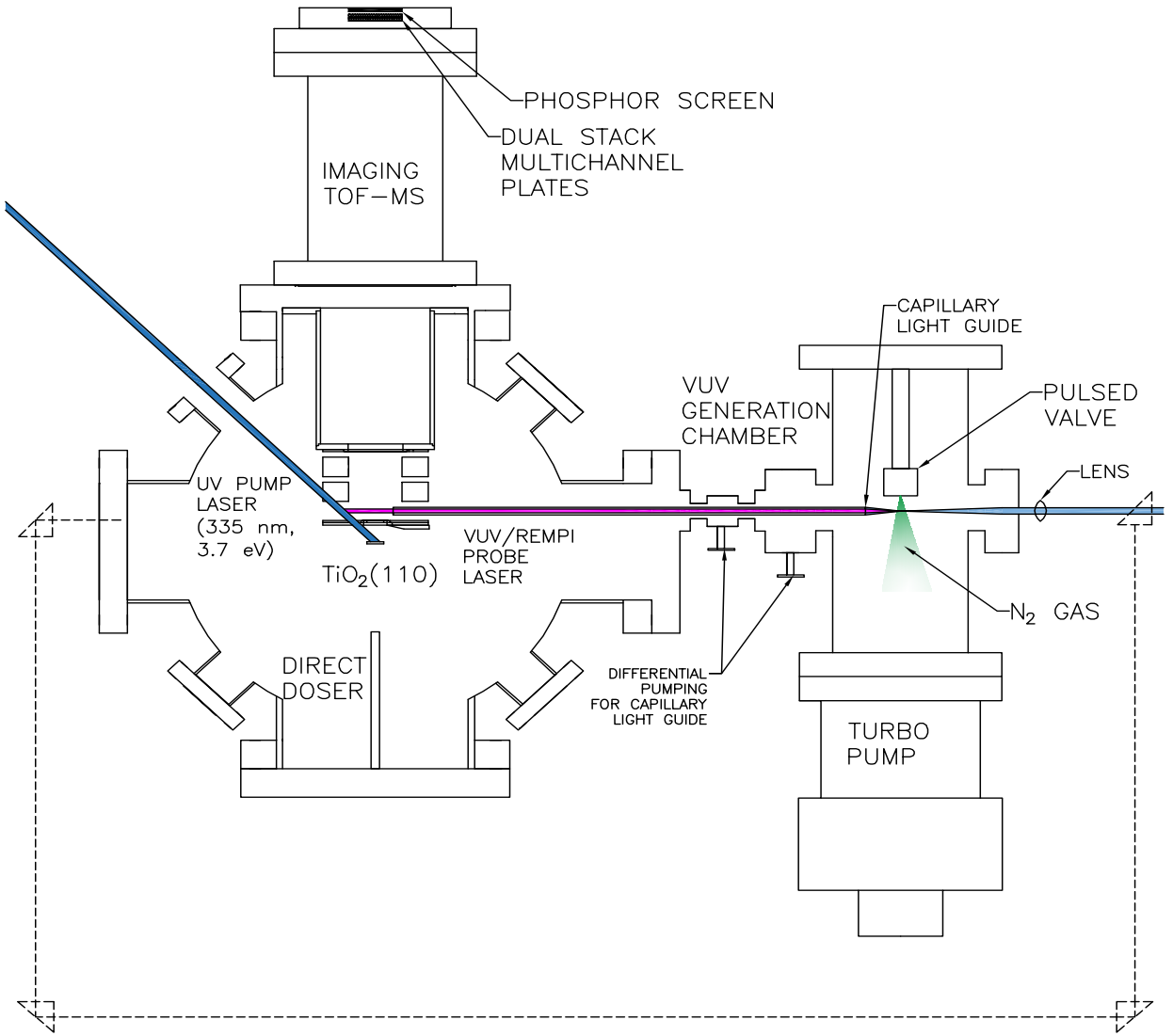

Figure 2.2: Lower level of the surface photochemistry chamber and attached VUV generation chamber. The dotted line shows the alternate probe laser beam path for the $(2+1)$ REMPI ionization schemes.

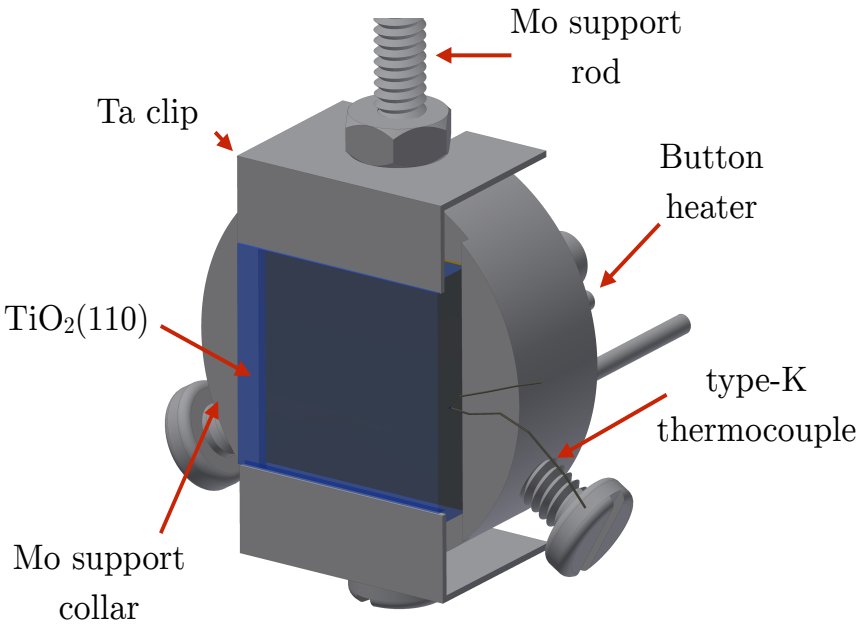

Figure 2.3: A three-dimensional rendering of the sample holder used in these experiments.

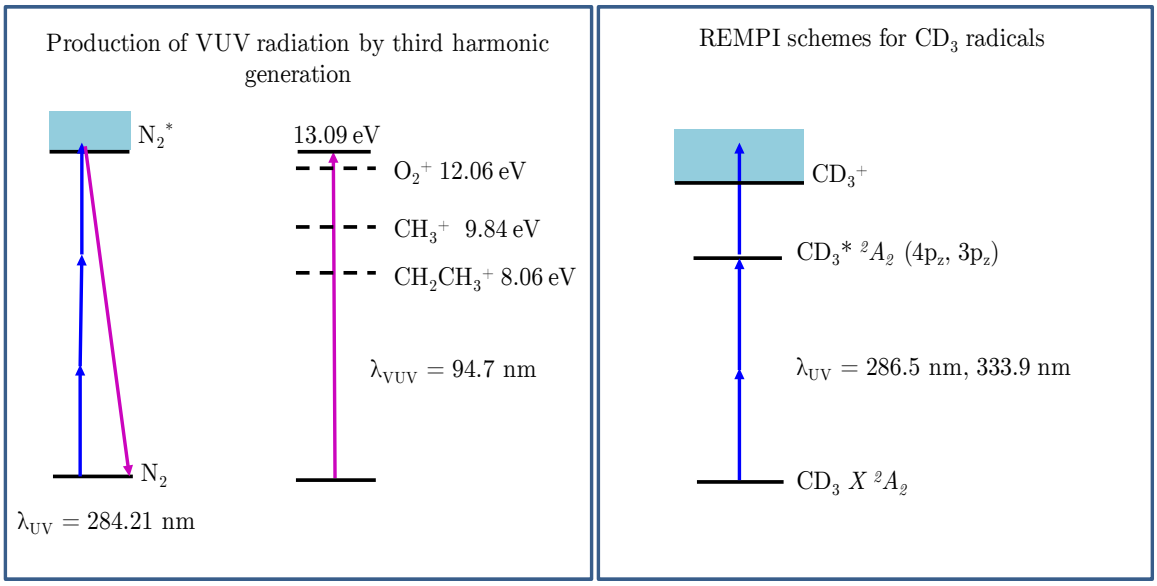

Figure 2.4: Diagrams showing the different ionization detection schemes used in this work. The generation of VUV photons is illustrated in the left hand panel along with relevant ionization potentials for some of the molecular species studied in this work. The REMPI schemes for deuterated methyl radical detection are shown in the right hand panel along with the relevant wavelengths coorresponding to the 0_0^0 bands of the $3p_z$ (333.9 nm) and $4p_z$ (286.5 nm) Rydberg states. For the alcohol experiments CH_3 radicals were detected using the 0_0^0 band of the $4p_z$ Rydberg state occurring at 286.3 nm

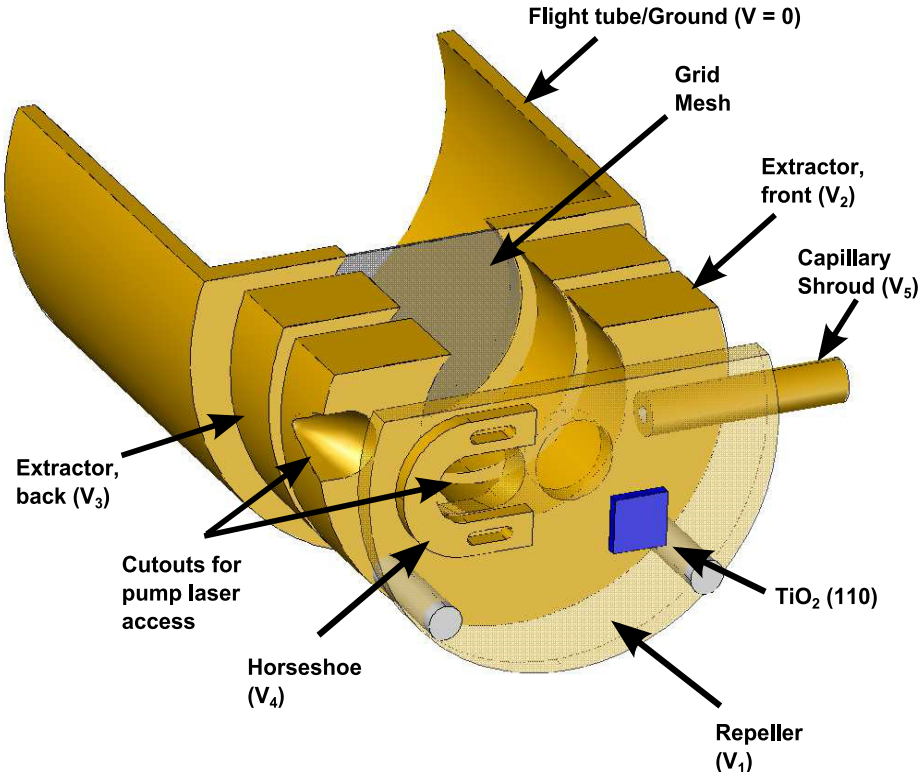

Figure 2.5: Drawing of the velocity map imaging time of flight spectrometer. The TiO_2 sample is approximately 29 mm from the ionization region between V_1 and V_2.

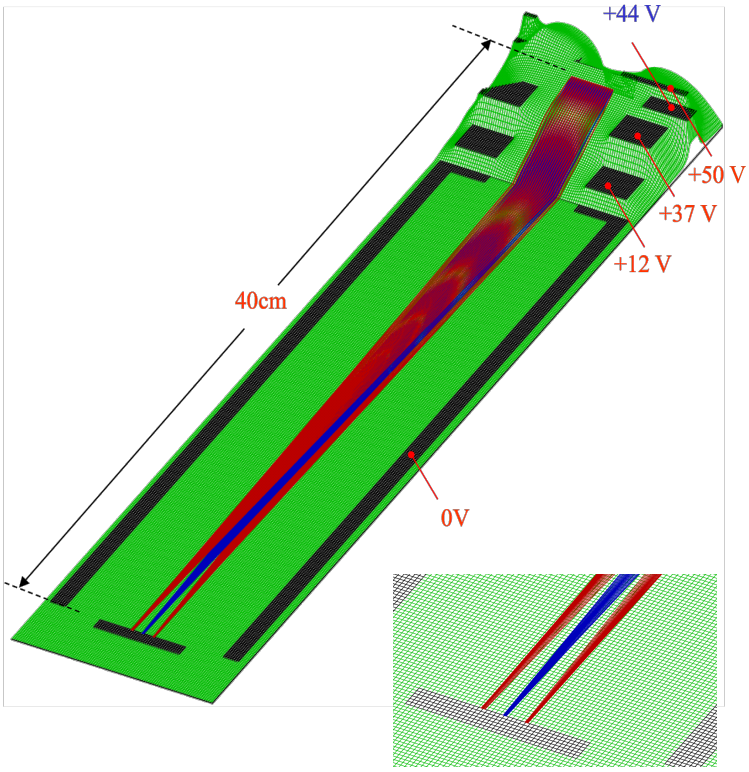

Figure 2.6: Graphical display from SIMION showing the vector velocity focusing capability of the imaging detector. The group of trajectories shown in blue are ions desorbing at 0° with respect to the surface normal whereas those trajectories shown in red are ions desorbing at ±20° with respect to the surface normal.

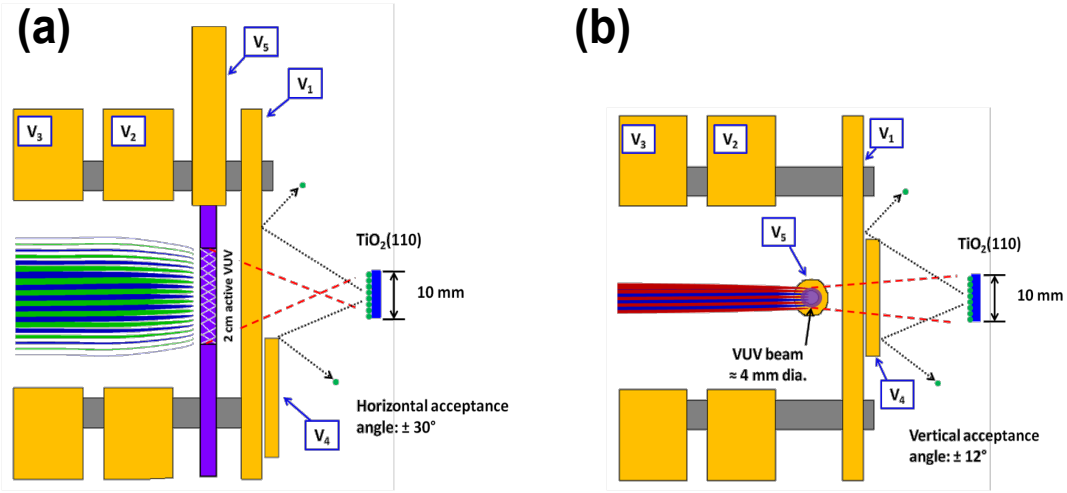

Figure 2.7: Cross-sections of the imaging detector with the crystal in place to better illustrate the finite angular acceptance angle of the detector. Drawing (a) shows the horizontal acceptance angle and (b) shows the vertical acceptance angle.

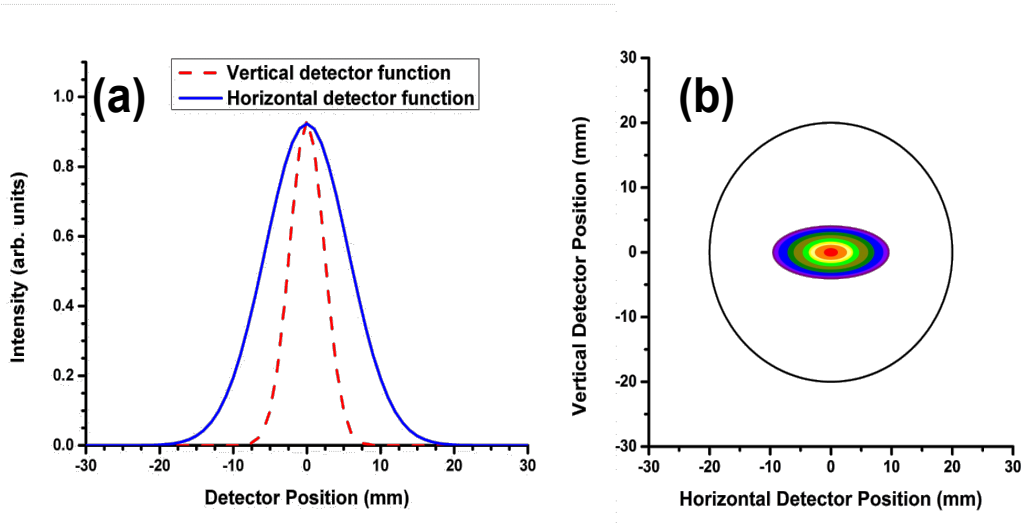

Figure 2.8: Graph (a) shows a comparison between the vertical and horizontal detector functions, graph (b) shows a simulated ion image based upon our known detection geometry. The black circle represents the phosphor screen boundary for scaling purposes.

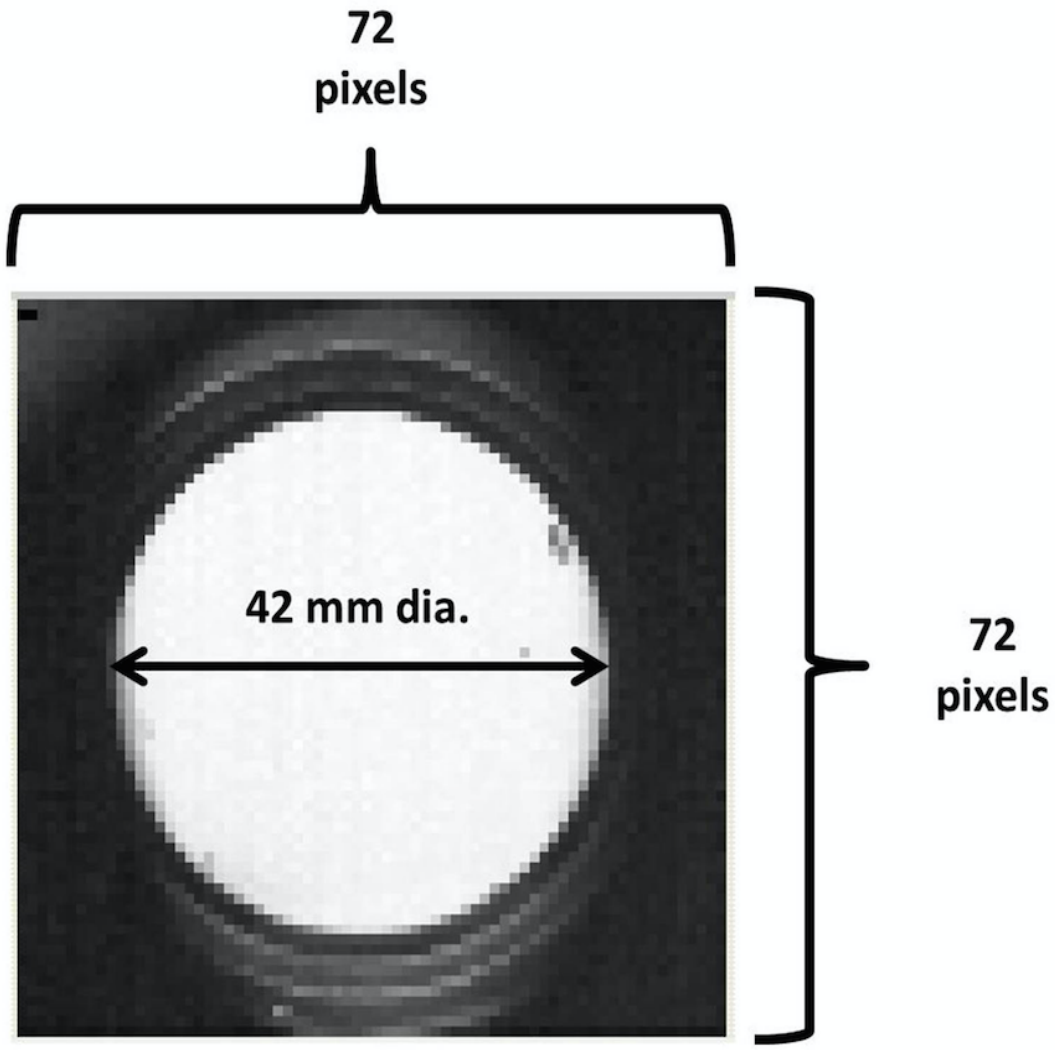

Figure 2.9: An image of the phosphor screen used to establish a calibration between pixel location and physical distance (in mm) across the detector.

3 Dynamics of acetone photooxidation on TiO_2(110): State-resolved measurements of methyl photoproducts

This section was published in *J. Chem. Phys.*, **138**, 204703 (2013)

3.1 Introduction

As a result of its photocatalytic properties, titania has been a material of great interest to the research community. One particular application involves the use of TiO_2 for the photocatalytic decomposition of organic pollutants in the environment.[24] As a common pollutant and the simplest ketone, acetone photodecomposition on TiO_2 is an interesting reaction which has been studied under both ambient and ultrahigh-vacuum (UHV) conditions.[6] An example of the former type of experiment would be the work performed by Coronado *et al.* using FTIR spectroscopy to confirm the presence of acetaldehyde, acetate, and formate species on the surface as well as CO_2 in the gas phase.[25] While studies of this reaction on powders provide useful information regarding reaction products under practical reaction conditions, ambient pressure experiments are nonetheless limited in their ability to directly study the elementary reactions which ultimately lead to these final products.

Subsequent work by Henderson has shown that under UHV conditions on TiO_2(110), acetone photodecomposes in the presence of co-adsorbed oxygen to produce a surface bound acetate species and a methyl radical which is ejected into vacuum.[14] In that work, it was observed that photodecomposition via methyl radical ejection was negligible when photon energies below the titania bandgap were used. This result suggests that acetone photodecomposition is a substrate mediated process whereby photogenerated charge carriers in the crystal are responsible for the reaction. This reaction also does not occur unless oxygen is present on the surface suggesting that acetone by itself may not be the photoactive species.

Previous work involving HREELs measurements which explored the structural relationship between acetone and oxygen on TiO_2(110) revealed the possibility that acetone can thermally react with oxygen to form an "acetone-diolate" complex.[20] Additionally, the photochemistry of such diolates has been investigated theoretically using density functional theory and molecular orbital calculations.[26] Formation of such a complex via reaction with oxygen would involve incorporation of one oxygen atom as part of the diolate with the other atom likely existing on the surface as an adatom. Evidence for the presence of oxygen adatoms on TiO_2(110) has been observed both as the result of thermal reactions[27] and photoreactions.[28] A recent study in our laboratory provided strong evidence for O-adatoms being the active species for formation of the photoactive acetone-oxygen complex.[15]

In an attempt to further elucidate the mechanism behind acetone photodecomposition, Wilson et al. used pump- probe laser ionization techniques to measure the velocity distribution of methyl radicals under various surface preparation conditions.[15] It was observed that methyl radicals leave the surface with a bimodal kinetic energy distribution which contains a "fast" and a "slow" component. Both channels were observed to be independent of both excitation wavelength and surface temperature. The former observation validates the idea of a photodecomposition mechanism involving charge carriers in the substrate, whereas the latter observation rules out the possibility of thermal influences in the desorption mechanism. From these results, it was concluded that these two energy distributions represent methyl fragments which originate from the same intermediate but find themselves in different final states.

Since desorbing methyl radicals can have energy distributed among vibrational and rotational degrees of freedom, it is reasonable to believe that the difference between the two kinetic energy channels could be resolved through a better understanding of the methyl radical internal state distributions. In determining which internal states to probe, it is important to note that during the photodissociation process, the methyl substituent from acetone undergoes a significant geometry change as it is ejected into vacuum. Specifically,

the substituent is bound to the parent molecule in a C_{3v} orientation, while the free radical exists as D_{3h}.[29] This pyramidal to planar transition implies that vibrational excitation in the umbrella mode vibration (ν_2) of methyl radical is a good candidate. Additionally, since Wilson *et al.* observed that the energy separation between the two kinetic energy channels is close to $2\nu_2$, it is possible that differences in umbrella mode population may be responsible for this kinetic energy difference.[15] Indeed, previous state-resolved studies of methyl fragments from the UV photodissociation of methyl iodide adsorbed on various surfaces have used ν_2 vibrational band populations to estimate methyl vibrational excitation and probe the coupling of vibrational and translational degrees of freedom.[30–34] Knowledge of methyl ro-vibronic distributions can also provide insights regarding the nature of the transition state complex. In particular, comparison between measurements of surface reaction dynamics and those made for gas phase systems can help to highlight both differences and similarities that can allow for better understanding of the reaction dynamics and the role of the substrate in photochemical processes.

In the experiments described here, we have employed resonance-enhanced multiphoton ionization (REMPI) techniques to probe the ro-vibronic state distributions of methyl radicals (CD_3) from the UV photooxidation of d_6 -acetone on a TiO_2(110) surface. While the energy difference between the kinetic energy channels and $2\nu_2$ is not strictly observed for CD_3 photoproducts,[15] CD_3 radicals are better suited to REMPI studies (particularly, for rotationally resolved spectra) because they predissociate to a lesser extent than CH_3.[35] It is important to note that kinetic energy distributions of CD_3 from acetone photooxidation are very similar to those obtained from un-deuterated acetone with both showing bimodal kinetic energy distributions.[15] Data presented below will provide insights regarding rotational energy distributions, ν_2 population, as well as the coupling between vibrational and translational degrees of freedom.

3.2 Experimental

For each photochemistry experiment, the surface was prepared by first exposing a 105 K surface to 80 L of research-purity O_2 (Matheson Tri-Gas) followed by $>$ 1 ML of d_6 - acetone (Cambridge Isotope Laboratories) as estimated via TPD measurements. Prior to use, the acetone was degassed by several pump-freeze-thaw cycles. Oxygen was used without additional purification. Oxygen exposures were achieved by backfilling the chamber and acetone was deposited on the surface using a directional doser (1 cm o.d. stainless steel tube with a pinhole aperture). As observed by Henderson, acetone photooxidation initially proceeds through the thermal reaction of acetone and co-adsorbed oxygen to form a photoactive acetone-diolate species.[14] To this end, we annealed our prepared surface to $\sim$ 200 K prior to photochemistry measurements to promote diolate formation and to thus improve CD_3^+ signal in our experiments. This preheating procedure also allowed us to maintain a consistent surface coverage which ultimately was $\sim$0.7 ML as confirmed by TPD experiments which were comparable to those published by Henderson.[20]

Photochemistry measurements were carried out using pump-probe laser techniques in conjunction with TOF-MS detection of desorbing species as described previously. The pump laser was set to a wavelength of 335 nm and a fluence of $\sim 2.3 \times 10^{12}$ photons $\cdot$ cm$^{-2}\cdot$ s^{-1} was typical for these experiments. As our laser system uses pulsed lasers with a repetition rate of 20 Hz, this fluence represents an average that was calculated by multiplying the average pulse fluence by the repetition rate.

Methyl radicals desorbing from the surface were ionized at a known distance (typically 26-29 mm) from the surface using a second laser which was aligned parallel to the surface. Ionizing radiation in the ultraviolet region was generated by doubling the output of a second Nd:YAG pumped dye laser (Spectra-Physics GCR-230, Laser Analytic Systems LDL-20505, Pyrromethene 597 dye in ethanol or DCM/LDS 698 in methanol). For the measurement of CD_3 rotational energy distributions, methyl radicals were ionized using one-color, (2 + 1) REMPI through the $^2A_2''(4p_Z) \leftarrow\leftarrow \tilde{X}^2A_2''$ Rydberg state intermediate.[36] Vi-

brational excitation was probed by another one-color, (2 + 1) REMPI scheme through the $^2A_2''(3p_Z) \leftarrow\leftarrow \tilde{X}^2A_2''$ Rydberg state intermediate.[36] For the former scheme, Pyrromethene 597 laser dye (ethanol solution) was used to generate 570-575 nm light (doubled to 285-287.5 nm), while for the latter scheme a mixture of DCM and LDS 698 dyes (methanol solution) was used to generate 660-670 nm light (doubled to 330-335 nm). The use of a different ionization scheme to probe vibrational excitation was necessary since, as reported by Hudgens and co-workers, only the $3p_Z$ state shows vibrational structure.[36] To analyze the methyl radical rotational distributions, comparisons were made between the experimental data and simulations performed using PGOPHER[37] and known spectroscopic constants.[35] Details concerning this procedure are presented in the following section.

As mentioned previously, we use pump-probe laser techniques which allow for the selective ionization of desorbing species based upon differences in their flight time to the ionization region. Results from our group which have been published previously have shown that photooxidation of d_6 - acetone results in the ejection of methyl radicals which exhibit a bimodal kinetic energy distribution.[15] These radicals possess a "slow" channel with a mean energy of 0.02 eV and a "fast" channel with a mean energy of 0.15 eV. Spectroscopic data were obtained by varying the ionization wavelength while fixing the laser delay to correspond to a particular kinetic energy channel, and state-resolved kinetic energy distributions were obtained by varying laser delay while fixing the ionization wavelength to that of a particular rovibronic transition.

3.3 Results

3.3.1 Rotational Energy Distributions

To measure the CD_3 rotational distribution, CD_3^+ ion signal was measured as a function of probe laser wavelength. Scans were taken over 0.5 nm regions using a laser wavelength step size of 0.005 nm and an average of 64 laser pulses per data point to maximize the spectral resolution. A small step size ensures that each rotational line is represented by a

sufficient number of data points and averaging each point over 64 (instead of a typical 32) helps improve signal to noise. Since the entire rotational spectrum could not be measured for a single crystal dose, individual scans were stitched together by overlapping each scan at a common rovibrational transition and normalizing the scans to one another so that the peak areas for the overlapped transition were equal. As a result, the entire rotational spectrum is a compilation of 14 individual scans. In addition to normalizing individual scans to one another, the data were also corrected for the depletion of surface reactants which occurred over the course of any given measurement. To accomplish this, CD_3^+ signal was measured as a function of time ensuring that enough data were taken to span our 10 min data acquisition time. Such measurements also helped to ensure that there was adequate signal to noise at long experiment times. For these measurements, the ionization laser was set to a wavelength of 286.6 nm to correspond to the 0_0^0 band head of the $4p_Z$ Rydberg state. An example of this depletion measurement is given in Figure 3.1 where we have shown both the raw data and a biexponential fit. Such complex kinetic behavior for photodesorption and photooxidation reactions on TiO_2 has been observed in other experiments.[9,11,15,38–41]

The rotational energy levels for methyl radical are those of an oblate symmetric top and can be described by the following equation:[35]

$$\begin{aligned} E =& E_0 + \Delta C K^2 - \Delta D_K K^4 + [B' N'(N'+1) - B' K^2 - \\ & D'_N N'^2 (N'+1)^2 - D'_{NK} N'(N'+1) K^2] - \\ & [B'' N''(N''+1) - B'' K^2 - D''_N N''^2 (N''+1)^2 - D''_{NK} N''(N''+1) K^2] \end{aligned} \tag{3.1}$$

where E_0 is the energy of the 0_0^0 origin band, B is the rotational constant for the moment of inertia about the C_2 axes, C is the rotational constant for the moment of inertia about the C_3 axis, K is the projection of the total angular momentum about the C_3 axis, and N is the total angular momentum minus the contribution from spin. The constants D_K, D_N, and D_{NK} account for the centrifugal distortion of the methyl radical which occurs during rotation due

to changes in C-H bond lengths (and thus the moments of inertia for CD_3).[29] For electronic transitions between non-degenerate multiplet states, spin-orbit coupling is expected to be negligible and is thus not resolved in either our experimental data or our simulation.[29] As a result, rotational transitions can be described by the quantum number N where $N = J - S$ with J being the total angular momentum for the molecule and S being the contribution to the total angular momentum from spin. The selection rules for rotational transitions as accessed via a two-photon excitation process are as follows:[36]

$$\Delta K = 0,$$

$$\Delta K = 0, \qquad \Delta N = 0, \pm 2$$

$$\Delta K \neq 0, \qquad \Delta N = 0, \pm 1, \pm 2$$

In order to facilitate the process of making line assignments and extracting a rotational "temperature" (T_{rot}), the experimental data were compared to a simulated spectrum created using PGOPHER[37] and the published rotational constants for the $4p_Z$ Rydberg state.[35] Comparison of our data to the simulation showed that methyl radicals in the 0.15 eV translational kinetic energy channel have a rotational energy distribution that is well-characterized by a Boltzmann distribution with $T_{rot} = 325 \pm 25$ K. Figure 3.2 shows the experimental data as well as the simulation for comparison. The rotational structure for the CD_3 radical as measured using a $(2 + 1)$ REMPI scheme, gives clear $P(\Delta N = -1)$, $O(\Delta N = -2)$, $Q(\Delta N = 0)$, $R(\Delta N = +1)$, and $S(\Delta N = +2)$ branches. As others have observed, the Q branch for this state is far more intense than any other branch and there is little in the way of resolvable rotational structure.[35,36] As a result, attention was focused on the measurement and analysis of the remaining four branches.

3.3.2 Vibrational population in the ν_2 "umbrella mode"

The vibrationally resolved spectrum in Figure 3.3, which spans the 0_0^0, 2_1^1, and 2_2^2 bands, shows that most of the vibrational population for this mode resides in the ground state (0_0^0 band) with little population in the first excited state (2_1^1 band) and essentially no population in the second excited state (2_2^2 band). This spectrum is the compilation of 6 individual scans taken at ~ 3 cm^{-1} increments which have been depletion corrected for coverage loss. The data, taken at a 21 μs laser delay, describe methyl radicals in the 0.15 eV translational kinetic energy channel. Since these bands are so far apart, it is not possible to scan across neighboring bands during a single experiment (i.e. single exposure of molecules on the surface). This is because the coverage of photoactive molecules on the surface is fixed for any given experiment and is being continuously depleted during our photochemistry measurements. It is thus not possible to scan the probe laser from one vibrational transition to another before the sample is depleted to an extent that makes the detection of useful signal impossible. This means that a normalization procedure like that used for the rotational energy distribution could not be used here and thus precluded the use of a Boltzmann plot as a means of assigning a vibrational "temperature" (T_{vib}) to desorbing methyl radicals. Instead, we took an approach similar to that of Srivastava and Osgood[30] where depletion measurements were made at both the 0_0^0 and 2_1^1 bands and used the ratio of integrated photoyields at each band to obtain an estimate for the vibrational population of $\nu = 1$ relative to that of $\nu = 0$. The data obtained at each transition were fit to biexponential decay functions and these functions were then integrated over the experimental time period to give the photoyield. Curves obtained at both bands are shown in Figure 3.4. By this method, the fraction of vibrationally excited methyl radicals relative to those in the ground state can be calculated. This value turns out to be $(\nu = 1/\nu = 0) = 0.012 \pm 0.005$. This number has been corrected for variations in laser power as well as the Franck-Condon factors for these transitions.[42] The uncertainty for this value is determined by taking into account the uncertainty in the fitting as well as the uncertainty in measuring the ionization

laser power used during each measurement. Assuming that the vibrational distribution can be characterized using Boltzmann statistics, this ratio can be converted to a vibrational temperature of $T_{vib} = 151 \pm 15$ K.

The latter should be treated as a lower limit since the vibrational populations are likely to be affected by predissociation rates that vary with increasing umbrella excitation.[30,33] Using rates obtained from previous REMPI studies of the $3p_Z$ state of CD_3, we estimate that the effects of predissociation would lead to a relatively small change in our derived vibrational temperature (< 20 K).[42]

3.3.3 Vibrationally resolved energy distributions

The final goal in this experiment was to investigate the coupling between translational kinetic energy and population in the ν_2 umbrella mode. To accomplish this, measurements were made where the ion signal was collected as a function of laser delay and the ionization wavelength tuned to a given rovibronic transition (either 0_0^0 or 2_1^1). To investigate the possibility of an inverted vibrational distribution, we did try to perform energy measurements at the 2_2^2 transition by initially looking for signal at a series of delays. However, it was found that the signal at this transition was too weak to allow for the collection of useful data. For measurements taken at the other two transitions, it was necessary to take the average of a minimum of three replicate data sets in order to ensure good signal statistics for the fitting process. In order to extract quantitative information from our data, the arrival time distributions were empirically fit to two "Boltzmann-like" functions as this was the fewest number of curves that could be used to fit the data well. While these functions are similar to those described by Comsa and David,[43] we freely varied many parameters to achieve the best possible fit to the data. The choice of these functions for fitting purposes is somewhat arbitrary and we are not attempting to extract translational temperatures from these fits. The measured arrival time distributions were then corrected for depletion of surface coverage and converted to velocity and energy distributions (along with the fitted curves) by applying

the appropriate Jacobian transformations as described in previous work.[15] In addition to performing Jacobian transformations on the experimental data, a linear interpolation is applied to the data as it is ultimately converted from the arrival time domain to the energy domain. This transformation is performed to generate evenly spaced energy data points since, particularly at short arrival times, small differences in arrival time ($\sim 1\ \mu s$) can lead to large differences in kinetic energy. For data with relatively low signal to noise ratio, as in the case of Figure 3.5(b), this procedure results in energy distributions with larger excursions in the data. These features should thus be interpreted as scatter in the data and not as meaningful structure.

Figures 3.5(a) and 3.5(b) show the fitted energy distributions measured for methyl radicals ionized through the 0_0^0 and 2_1^1 transitions, respectively. Figure 3.6 shows the combined fits for both distributions and illustrates that methyl radicals which are vibrationally excited are less energetic than those which are not. The numbers in Table 3.1 show that the mean energies for methyl radicals in their ground vibrational state are in close agreement with previously published results.[15] On the other hand, for methyl radicals with $\nu_2(\nu = 1)$, the mean energy of the fast channel (E_{fast}) is 0.030 eV less than for methyl radicals with $\nu_2(\nu = 0)$ and the difference in overall energy (E_{tot}) is 0.035 eV. While the energies for the slow channels are identical within experimental error, the fast:slow ratio for the vibrationless methyl radicals is almost a factor of 2 larger than that for the vibrationally excited radicals.

3.4 Discussion

While this work represents the first use of REMPI spectroscopy to characterize methyl photofragments from acetone photooxidation on $TiO_2(110)$, the literature contains a number of prior studies of methyl photofragments generated from methyl iodide on various substrates.[30–34,44–46] In particular, these publications have all used REMPI probes to investigate the population of the ν_2 umbrella mode in an effort to better understand the reaction dynamics. The reason for studying this mode stems from the notion that umbrella mode excitation

should be expected when methyl substituents go from their initial C_{3v} symmetry to the final D_{3h} symmetry of the radical product. Gas phase studies of acetone photolysis have shown that methyl radicals are produced with substantial population in the ν_2 mode ($T_{vib} \sim 800$ K).[47] This result, along with information regarding translational kinetic energy distributions, was rationalized in terms of an impulsive model of the reaction dynamics whereby the energy responsible for bond cleavage is directed along the center of mass of the methyl substituent resulting in substantial ν_2 population as well as high kinetic energy ($\sim 0.4 - 0.5$ eV).

For methyl iodide on TiO_2(110), the photodissociation mechanism is different than the mechanism being considered here.[32] In that work, Holbert and co-workers determined that desorbing methyl radicals possessed a velocity distribution with both fast and slow components. It was observed that the velocity of the fast methyl radicals was dependent on the photolysis energy and were thus attributed to direct excitation of the adsorbate. Slow methyl radicals were attributed to collisions with the surface. This conclusion was confirmed by taking velocity distributions with the ionization laser tuned to the 2_1^1 transition which showed a distribution dominated by fast radicals and essentially no slow radicals. As discussed in the next paragraph, this also indicates that lack of population in the ν_2 mode for slow radicals can be attributed to a collisional relaxation mechanism. Velocity distributions taken as a function of coverage also showed that slow methyl radicals dominate at high coverages.

Collisional relaxation was also observed by Fairbrother et al. in their study of methyl iodide photodissociation on MgO(110) where it was seen that when methyl iodide multilayers are present on the crystal surface, certain molecules adopt an anti-parallel orientation such that the methyl radicals point toward the surface. Upon photodissociation, these radicals strike the surface and rebound into vacuum. The collision with the surface efficiently relaxes the radicals to their ground vibrational state and they emerge with diminished population in the umbrella mode.[31]

For the case of acetone photooxidation on TiO_2(110), we do not expect desorbing methyl radicals to undergo collisions with the surface. Work by Henderson has shown that molecular

acetone reacts with chemisorbed oxygen on TiO_2(110) to form what he calls an acetone-diolate complex.[20] On this basis alone, it should be expected that all methyl radicals are already pointing away from the surface thereby making collisions with the surface unlikely.

In comparing our results to those obtained for methyl iodide, it is important to highlight significant differences in the reaction mechanisms. In many cases, methyl ejection from methyl iodide proceeds by direct excitation of the adsorbate in a fashion analogous to gas phase photolysis experiments. Even in the case of methyl iodide on TiO_2(110) where supraband gap photons were used, adsorbate interaction with charge carriers led to molecular desorption and not photodissociation.[48] In contrast to methyl iodide photodissociation where electronic excitation within the adsorbate leads to fragmentation, acetone photodecomposition proceeds as a result of interactions between the acetone diolate complex and photogenerated charge carriers in the substrate.[14,15] Unlike the methyl iodide experiments which showed that the velocities of fast methyl radicals were dependent upon excitation wavelength, experiments by Wilson et al. have shown that velocity distributions of methyl radicals produced from acetone photodecomposition remain unchanged as a function of incident photon energy.[15] In fact in that work, it was postulated that the two kinetic energy channels represent two different final states of the methyl radical originating from the same excited state distribution.

The results presented in this paper show that umbrella mode excitation in desorbing methyl radicals results in less energy being available for translation. Specifically, it appears that the amount of energy that is being lost in terms of kinetic energy is of the order of $\sim$ 35 meV. If we assume, as previously postulated,[15] that the total energy available to desorbing methyl radicals is fixed, then we might also expect the amount of kinetic energy lost is comparable to the energy difference between the two vibrational energy levels. The vibrational spacing for the ν_2 mode, as measured by Snelson,[49] is 463 cm^{-1} which is equivalent to 57 meV. While these two values are not in perfect agreement, the fact that they are of the same order of magnitude suggests that translation and vibration are coupled based

on simple energy conservation arguments. The discrepancy between our measured kinetic energy difference and the ν_2 vibrational spacing could be due to other processes which do not allow for complete energy redistribution into vibration. Such processes could be the participation of other internal states or adsorbate-surface energy transfer.

Another point of interest in this work is the observation of a cold vibrational distribution for methyl radicals in the fast channel. Our measurements show that the relative population of radicals in the $\nu_2(\nu = 1)$ level to that of the ground state is only on the order of $1\% - 2\%$. This population corresponds to a T_{vib} which is reasonably close to thatof the surface. Based on what is already known regarding the photoactive species in this reaction (i.e., acetone-diolate complex), it is not expected that methyl radicals undergo collisions upon desorption from the surface. This is in contrast to methyl iodide photoreactions on various surfaces which reveal a high probability of gas-surface collisions particularly at high coverages. An alternate relaxation mechanism was suggested by Srivastava and Osgood who observed vibrationally relaxed methyl radicals as a result of methyl iodide photodissociation on GaAs(110).[30] Their REMPI (ν_2) probe of translationally slow methyl radicals revealed a cold vibrational distribution as compared to gas phase measurements. This result was rationalized in terms of a dissociative electron attachment (DEA) mechanism where methyl iodide captures an electron and forms an anionic intermediate that places the methyl radical in a planar geometry.[50] If the methyl radical is in a planar geometry prior to dissociation, it can result in a lower population of the ν_2 vibrational mode. While acetone photooxidation may similarly proceed via a "late" transition state, it has been suggested that this reaction is hole-mediated rather than electron-mediated.[15] This makes photodecomposition via DEA an unlikely pathway, although future experiments making use of two-photon photoemission (2PPE) spectroscopy should help us to better understand the nature of charge transfer between the surface and the adsorbate

3.5 Conclusion

State-resolved measurements of methyl radicals resulting from acetone photodecomposition on $TiO_2(110)$ have been performed using REMPI spectroscopy. Fragments with a mean kinetic energy of 0.15 eV were found to possess a rotational distribution with $T_{rot} = 325 \pm 25$ K which falls in between the surface temperature and the value expected for the gas phase photodissociation of acetone. Our estimate of vibrational excitation in the ν_2 mode revealed that these methyl radicals can be characterized by a $T_{vib} = 151 \pm 15$ K assuming a Boltzmann distribution. This value, which is significantly colder than gas phase measurements, implies that methyl radical ejection from the acetone-diolate complex proceeds via a late transition state such that significant vibrational relaxation can occur. State-resolved energy distributions also show that less energy translational kinetic energy is available for vibrationally excited methyl radicals and that this difference is close, but not equal, to the energy spacing of the ν_2 vibrational mode.

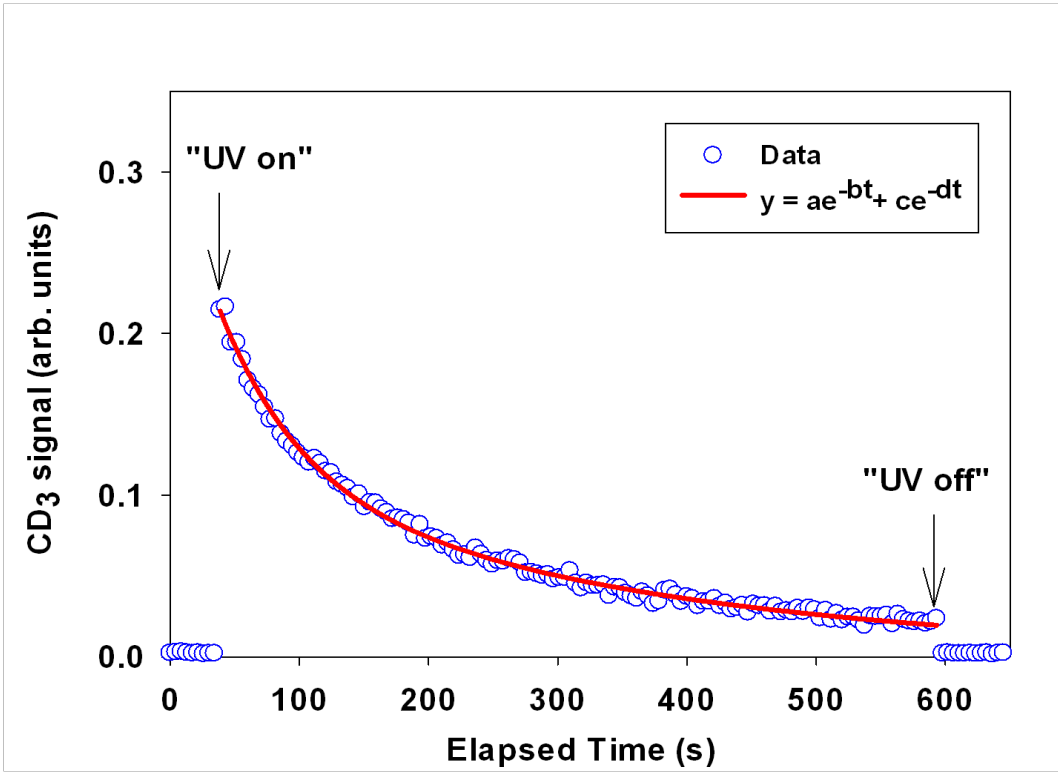

Figure 3.1: A typical depletion curve, showing the methyl radical signal as a function of irradiation time, which is used to correct individual rotational scans for the loss of signal as a result of the surface photoreaction. Open circles denote experimental data while the solid curve represents a four parameter, biexponential fit to the data. Such complex depletion kinetics are commonly observed for substrate-mediated photochemistry on TiO_2 surfaces.

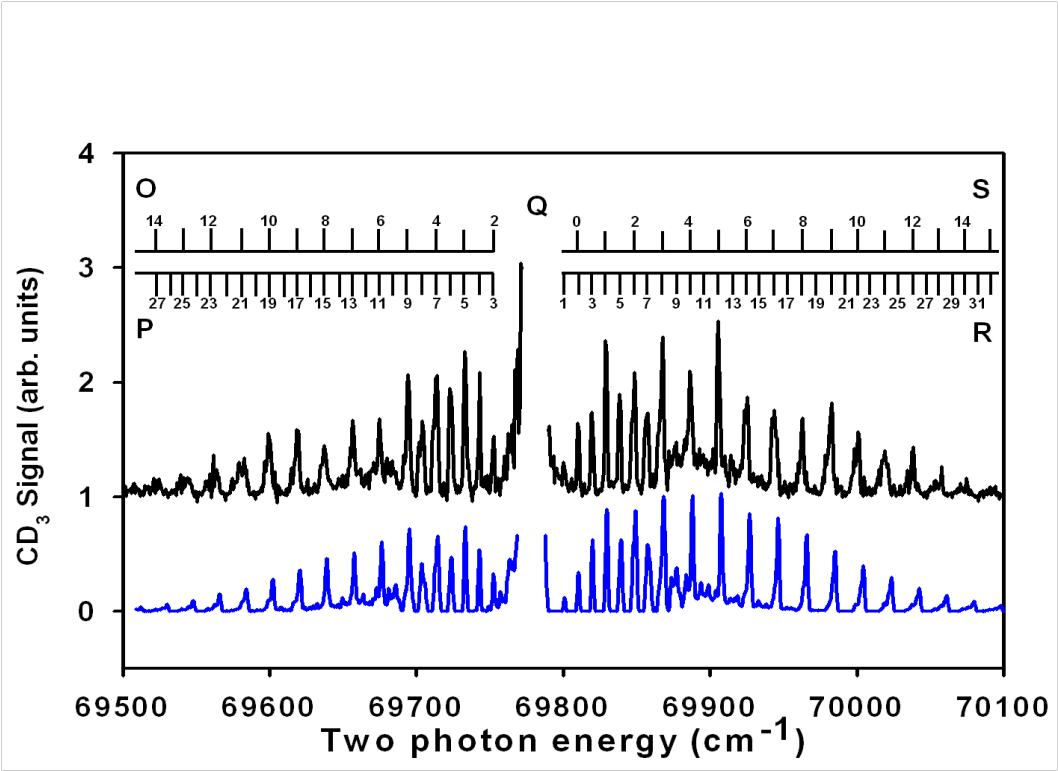

Figure 3.2: Rotationally resolved REMPI spectrum of 0.15 eV methyl radicals via the 0_0^0 transition of the $4p_Z$ Rydberg state. The top trace is the experimental data and the bottom trace is a PGOPHER simulation at $T_R = 325 \pm 25$ K which has been vertically offset for clarity.

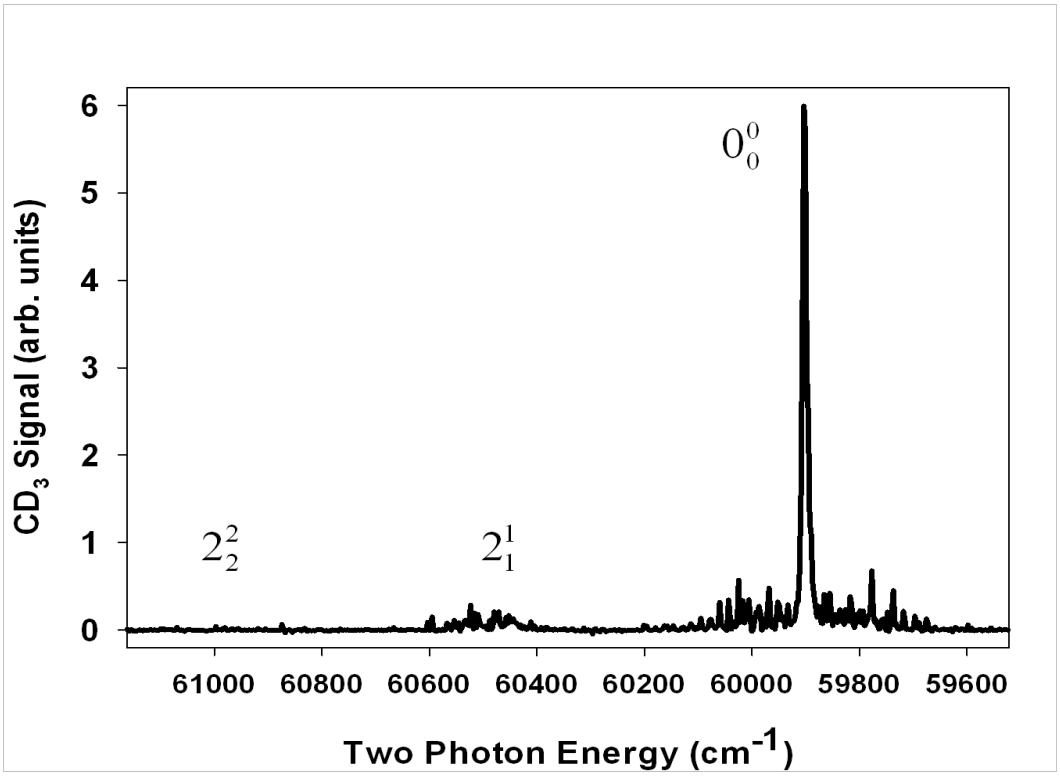

Figure 3.3: $(2+1)$ REMPI spectrum ($^2A_2''(3p_Z) \leftarrow\leftarrow \tilde{X}^2A_2''$) of methyl radicals of the fast channel. The spectrum shows little vibrational excitation for radicals in this channel. Data were recorded using a 21 μs laser delay and a 3 cm^{-1} step size and are not corrected for variations in ionization laser intensity.

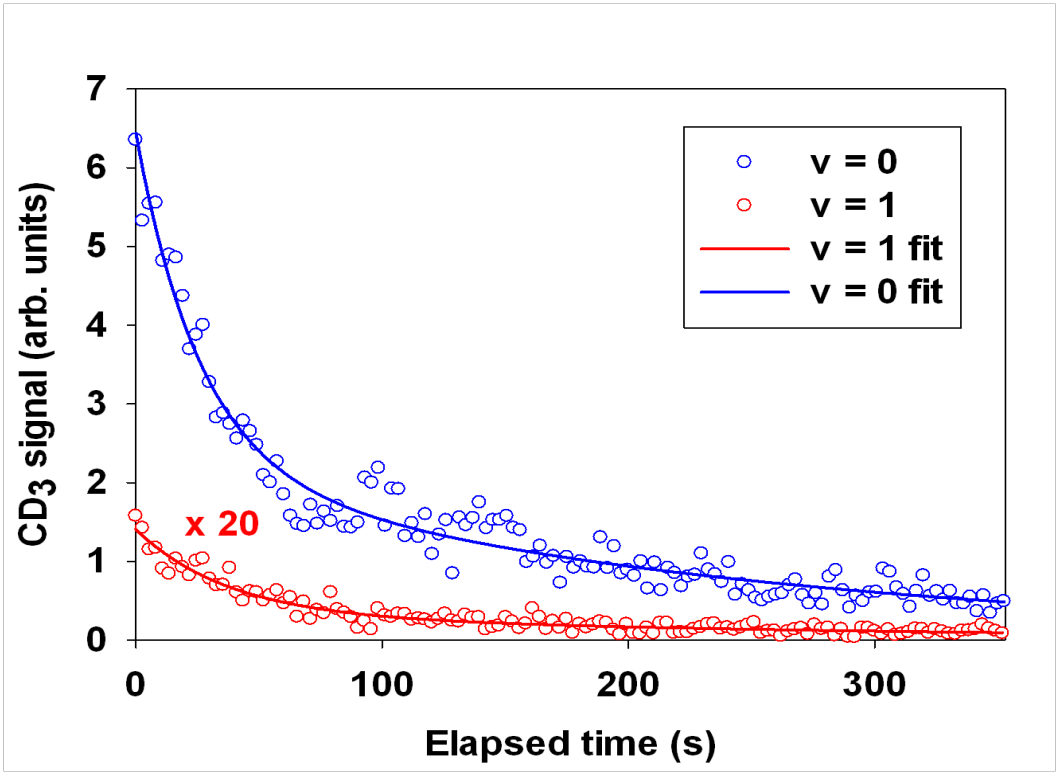

Figure 3.4: Vibrationally resolved depletion curves for methyl radicals of the fast channel. Both datasets have been corrected for differences in ionization laser power and the $\nu = 1$ set has been multiplied by 20 for ease of comparison. For both measurements, the prepared sample was irradiated using a photon flux of $\sim 2.3 \times 10^{12}$ photons·cm^{-2}· s^{-1}.

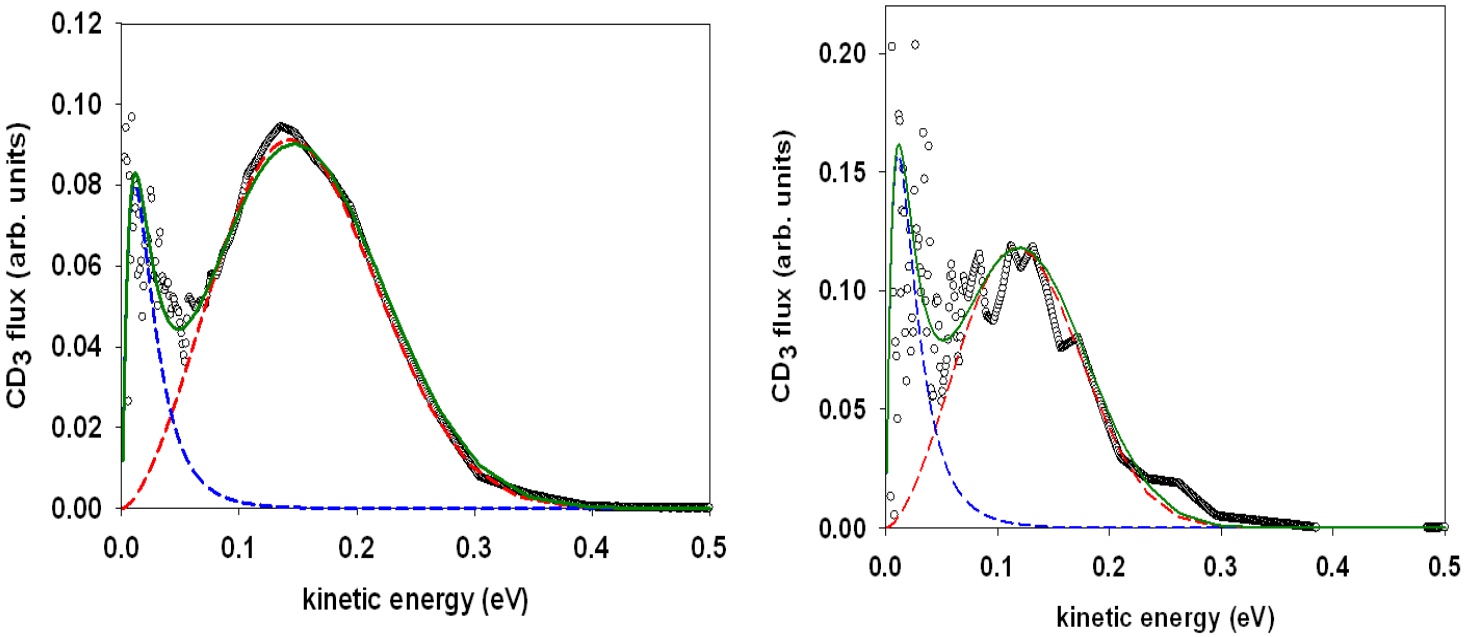

Figure 3.5: (a) Energy distribution for methyl radicals in the $\nu_2(\nu = 0)$ vibrational state and (b) in the $\nu_2(\nu = 1)$. The experimental data are shown as open circles, whereas dashed curves represent fits for the individual kinetic energy components. The solid curve represents the sum of these two fits.

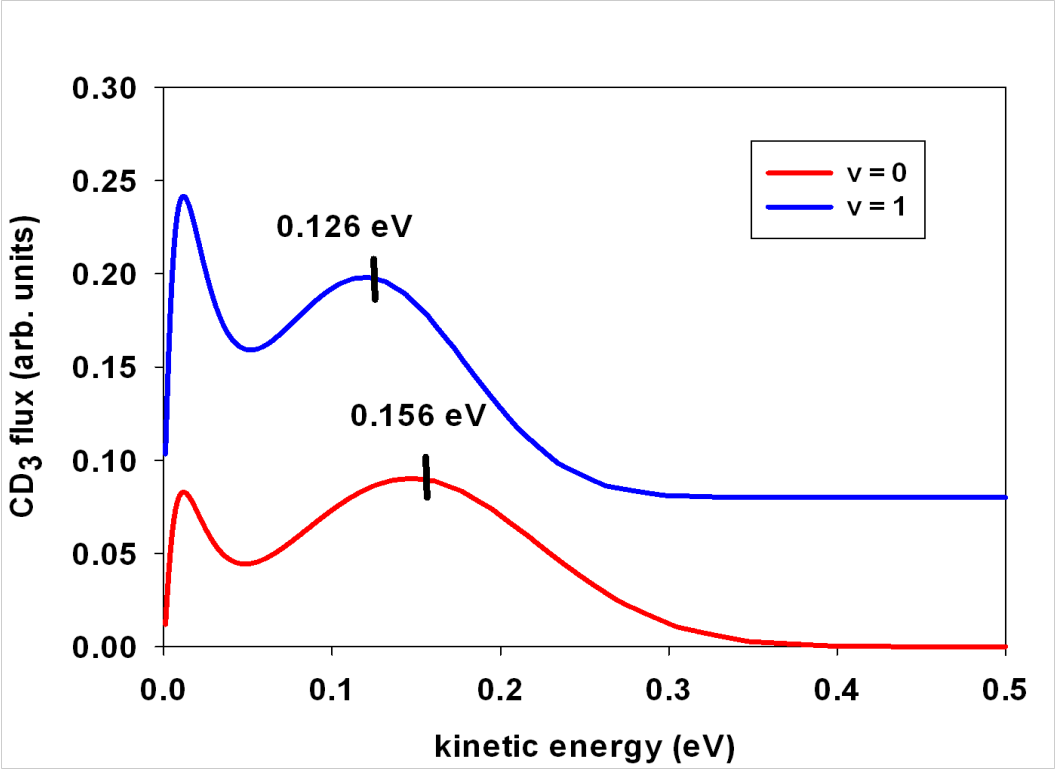

Figure 3.6: Combined fits as a function of vibrational state. Curves are vertically offset for clarity and the mean fast-channel energies are marked for comparison purposes.

	$\langle E_{fast} \rangle$	$\langle E_{slow} \rangle$	$\langle E_{tot} \rangle$ (from data)	$\langle E_{tot} \rangle$ (from fits)	Fast:slow
$\nu = 0$	0.156	0.027	0.137	0.141	5.7
$\nu = 1$	0.126	0.028	0.102	0.104	2.9

Table 3.1: Values showing the mean energies for energy distributions taken for each vibrational state. Also shown are the ratios showing the relative population of methyl radicals in the fast and slow channels. Energy values are in units of eV and are accurate to within $\sim 6\%$ of the quoted value

4 Exploring surface photoreaction dynamics using pixel imaging mass spectrometry (PImMS)

This section was published in *J. Chem. Phys.*, **139**, 084202 (2013)

4.1 Introduction

Since the pioneering work performed by Chandler and Houston[51] and Eppink and Parker,[52] velocity map imaging experiments have been used extensively for elucidating gas phase reaction dynamics occurring at the molecular level.[53] Although the technique was initially used to study gas-phase reactions, several groups have used this approach to study reaction dynamics at surfaces.[54–64]

A common feature to all of these studies is the use of a time-of-flight mass spectrometer (TOF-MS) that is capable of spatially separating ions based upon differences in kinetic energy and trajectory. By using ion optics capable of velocity-vector focusing, ions with a common velocity and trajectory are focused to the same spot on the detector, typically a microchannel plate (MCP) coupled to a phosphor screen. Images of the phosphor screen captured during the experiment can then be analyzed to yield dynamical information about the reaction. While this feature is useful in gas phase experiments for discriminating amongst reaction products with different internal state distributions, surface scientists can use this technique to determine the angular distribution of molecules and/or molecular fragments desorbing from a surface. For reactions which produce multiple products, differences in ion time-of-flight can be exploited to allow for the imaging of different species. Traditionally, the imaging of multiple products is accomplished by applying a time-gate to the TOF-MS detector, whereby the detector is switched on during the expected arrival time window of the mass of interest and is switched off at all other times during the experiment. This procedure is then repeated for imaging other masses. While this is certainly an effective means of conducting a comprehensive imaging study of multiple reaction species, it can prove to be

highly time consuming. This is particularly true for surface science experiments, since surface cleaning and preparation in between measurements leads to additional down time.

For the study of complex photoreactions which yield multiple products, it is highly advantageous to use techniques which allow for the imaging of multiple masses during a single experiment without mass gating. As a result of advances in image sensor technology, multiple mass image capture is now possible using sensor arrays capable of multi-hit, time-resolved detection at individual pixels on a time scale of tens of nanoseconds.[65–68] The combination of mass spectrometry using velocity vector focusing and time-resolved image capture, so-called pixel imaging mass spectrometry (PImMS), has recently been applied to the study of gas-phase fragmentation processes[69] as well as to spatial imaging mass spectrometry.[70] As demonstrated in this work, the PImMS technique is especially useful for analogous surface photochemistry experiments involving multiple mass photoproducts.

In this experiment, we use the PImMS technique to study the ultraviolet (UV)-induced photooxidation of 2-butanone (methyl ethyl ketone) on a $TiO_2(110)$ single crystal surface. These experiments are motivated by the widespread use of titania as a photocatalyst for the degradation of organic pollutants from air and water environments.[5,7,24] Previous work has shown that under UHV conditions, multiple photoproducts are ejected into vacuum (methyl and ethyl radicals, molecular oxygen) upon irradiating adsorbed butanone-oxygen adlayers with ultraviolet light.[16,41] Particularly for the case of ethyl radical desorption, multiple, closely spaced mass peaks (m/z: 27-29) are observed in product mass spectra, which are assumed to be $C_2H_x^+$ hydrocarbon fragments ($x = 3, 4, 5$). Initial studies by Henderson[41] assigned these C_2H_x fragments to primary and secondary reaction products, whereas a recent pump-probe study by Wilson et al.,[16] suggests that all the mass fragments are associated with direct ethyl ejection without secondary collisions. In this work, we show how PImMS technology can be applied to surface photochemistry experiments and use it to gain additional insights into the dynamical origins of the C_2H_x photofragments from butanone photooxidation.

4.2 Experimental

A schematic diagram of the experimental setup is shown in Figure 4.1. The TiO_2(110) surface dosed with adsorbates is irradiated by a UV pump laser beam (335 nm; 3.70 eV) at an incident angle of 45°. Neutral fragments coming from the surface travel a free flight distance of 29.4 mm before being ionized by the coherent vacuum ultraviolet (VUV) radiation (94.7 nm; 13.09 eV) which passes parallel to the surface plane in the center of the acceleration region of an imaging TOF-MS. The ions are accelerated by the lens elements and detected $\sim$ 40 cm downstream by a dual MCP detector and phosphor screen. A sealed enclosure surrounds the phosphor outside of the chamber to minimize light contamination from the laboratory. Due to space restrictions, the PImMS camera was mounted outside of this enclosure. A piece of PVC (polyvinyl chloride) tubing was used to couple the camera to the enclosure and a mirror placed in front of the phosphor directed the images to the camera sensor. In addition to the PImMS camera, a photomultiplier tube (PMT) was placed inside the enclosure, enabling signal from the phosphor to be measured when performing conventional TOF-MS experiments.

Prior to photochemistry experiments, the titania surface was exposed to 80 L of oxygen followed by $\sim$ 1 ML of butanone. Research grade oxygen (Matheson Tri-Gas) was used without further purification, while butanone (Sigma- Aldrich) was purified by multiple pump-freeze-thaw cycles. Oxygen was admitted to the surface by backfilling the chamber and butanone gas was deposited on the surface using a directional doser. Prior to beginning a measurement, the surface was heated to a temperature of $\sim$ 200 K to enhance the ethyl radical signal as observed in previous work.[16] Additionally, photochemistry experiments were conducted in a background atmosphere of oxygen (5×10^{-8} Torr) to further enhance signal levels. By comparing our TPD data to the results published by Henderson,[41] we estimate our butanone coverage at $\sim$ 200 K to be less than $\sim$ 1 ML. Due to the relatively high background pressure of oxygen used in these experiments, the MCP detector was gated so that the large O_2 signal did not damage the detector or saturate the camera sensor.

Pump-probe laser techniques were used to generate and ionize neutral gas-phase species. The pump laser fluence was maintained at $\sim 3.4 \times 10^{14}$ photons $cm^{-2} \cdot s^{-1}$ for these experiments and a single photon, VUV detection scheme was used for product ionization by the probe laser.

4.2.1 PImMS Camera

The PImMS camera has already been described in previous publications, and so only a brief discussion will be presented here.[65–70] The heart of the PImMS camera system is a 72×72 pixel array based on CMOS technology which is designed to capture the visible light image emitted from the phosphor screen. The PImMS sensor is set apart from conventional imaging cameras through its ability to record spatial and temporal information simultaneously for each detected particle. At the time of these experiments, the best available timing resolution was 25 ns, although 12.5 ns resolution is now achievable. Using a time resolution of 25 ns, data can be acquired for 102.4 μs per TOF cycle, determined by the 12-bit capacity of the pixel clock.[69]

4.3 Results

Previous work[41] has shown that the main photooxidation pathway of 2-butanone on $TiO_2(110)$ proceeds via ejection of an ethyl radical (C_2H_5 ; mass 29) into vacuum. However, time-of-flight mass spectra showed the presence of masses at 26-28 amu in addition to ethyl radicals. The kinetic energy distributions obtained for masses 27, 28, and 29 were found to be bimodal ($\langle E_t \text{ (fast)} \rangle = 0.098$ eV, $\langle E_t \text{ (slow)} \rangle = 0.024$ eV) and it was observed that the three distributions were identical.[16] This result is indicative of masses 27-29 having the same neutral parentage, i.e., mass 27 and 28 result from the dissociative ionization of ethyl radical (mass 29) induced by VUV ionization at 13.09 eV.[71] Consequently, mass 27 and mass 28 ions correspond to $C_2H_3^+$ and $C_2H_4^+$ fragments. The time-of-flight spectra of all the gas-phase products resulting from 2-butanone photooxidation on $TiO_2(110)$ are presented in Figure 4.2 and are

consistent with previously published results.[16] The spectrum in Figure 4.2(a) was recorded at a pump-probe laser delay of 59 μs (representative of "slow" ethyl radicals) and shows the presence of methyl radical, background water, and ethyl radical and its fragments. The spectrum in Figure 4.2(b) was taken at a 24.6 μs pump-probe laser delay (representative of "fast" ethyl radicals) and shows a similar product distribution. A small amount of photodesorbing oxygen (mass 32) is also seen. The latter arrives slightly before the background oxygen (as a result of its additional kinetic energy) and thus falls just outside of the gating pulse applied to the MCP detector. The O_2^+ signal is actually much larger than seen in Figure 4.2, but the MCP gate was chosen to eliminate a majority of this signal to prevent saturation of the MCP. The mass spectrum in Figure 4.2(b) shows a small peak for mass 26, whereas this feature is absent at longer pump-probe laser delays (Figure 4.2(a)). As a result of such small signal, it is not possible to provide any further insights into the origin of the mass 26 species, although the observed dependence of the signal on pump-probe laser delay suggests that it is not due to fragmentation of the ethyl radical photoproduct.[16] Signal due to methyl radical is significantly larger at the shorter laser delay consistent with the higher average kinetic energy for the methyl radical ($\langle E_t(\text{total})\rangle = 0.195$ eV) compared to ethyl radical ($\langle E_t(\text{total})\rangle = 0.051$ eV) produced by 2-butanone photooxidation.[17]

In addition to showing the product TOF-MS in Figs. 4.2(a) and 4.2(b), we have also included "4D" representations (which are functions of time, x pixel, y pixel, and signal intensity) of the data as recorded by the camera. The horizontal axis represents time whereas the vertical axis represents one of the camera's pixel directions (i.e., either x or y). The other pixel direction would be normal to the plane of the page and is thus not visible. In this representation, the spatial distribution of reaction products as a function of flight time can be easily visualized. For the $C_2H^+_{(2-5)}$ species, there is an obvious increase in spatial size going from high to low mass. As will be discussed below, this is due to fragmentation of the ethyl cation. Primary surface products (such as methyl and ethyl radicals) appear as tightly collimated distributions about the detector axis whereas background species (such as water)

do not appear to be collimated at all.

Two-dimensional cuts through the PImMS data sets, yielding velocity-map images for ethyl radical and its fragments, are shown in Figure 4.3. The images in Figure 4.3(a) were taken at a pump-probe laser delay of 59 μs, while those in Figure 4.3(b) were taken at a laser delay of 24.6 μs. These laser delays correspond to ionization of the "slow" and "fast" fragments, respectively. As noted earlier, ion images taken at different laser delays will generally have different sizes due to differences in the transverse velocity components of neutrals entering the ionization region with non-zero angles. This is clearly seen for mass 29, for which the image for the "slow" ethyl fragments (Fig. 4.3(a)) is smaller than that for the "fast" ethyl fragments (Fig. 4.3(b)). Note that a similar increase in spatial extent is not observed for masses 27 and 28. More important is the increase in image size for the mass 27 and 28 fragments compared to the ethyl radical parent (mass 29) at either pump-probe delay. As noted above, previous pump-probe experiments have shown that all the three ion products (masses 27-29) exhibit the same velocity and translational energy distributions.[16] The velocity distributions of the various fragments are reflected in the radial distributions of the corresponding images. Hence, if masses 27, 28, and 29 were desorbed directly from the surface, one would expect that the images for all three masses should exhibit similar spatial distributions except for a scaling arising from the difference in mass. The increase in image size for masses 27 and 28 compared to mass 29 must then be due to differences in angular distributions and/or an increase in transverse energy spread. A change in angular distribution would suggest differences in neutral fragmentation dynamics for masses 27-29, whereas an increase in transverse momentum could result from dissociative ionization following VUV photoionization of the parent ethyl radical. As will be discussed in the next section, it is possible to distinguish between signal resulting from direct photodesorption from the surface and signal resulting from fragmentation within the mass spectrometer.

4.4 Discussion

The detector functions not only allow us to extract angular distribution data from the 2D images, but are also useful for differentiating between contributions originating from the desorption of surface species and those arising from fragmentation that occurs after ionization. In Figure 4.4, horizontal cuts through the 2D images shown in Figure 4.3 are plotted along with the detector functions calculated for the relevant pump-probe laser delay and fragment mass. The experimental data shown in Figures 4.4(a) and 4.4(b) were taken at a pump-probe laser delay of 59 μs and 24.6 μs, respectively. As is seen in Figure 4.4, for a given choice of laser delay/ion velocity, the detector functions for masses 27-29 are practically identical. This is due to the fact that the difference in kinetic energy for these ions is small ($\sim 3\% - 5\%$). While the images for mass 29 in Figures 4.3(a) and 4.3(b) are of different sizes depending on the ion's kinetic energy, this difference is not obvious when looking at the detector functions. This is because the detection probability, when presented as a function of desorption angle, must be the same regardless of the ion's initial kinetic energy. If this were not the case, it would be impossible to compare angular distributions for ions generated at different laser delays.

The data presented in Figure 4.4, which shows horizontal cross sections of the images in Figure 4.3, are helpful in understanding which species are due to photodesorption from the surface and which species are due to the fragmentation of primary photoproducts. The signal distribution obtained for mass 29 (ethyl radical) is seen to be significantly narrower than the calculated detector function for both laser delays. This shows that the horizontal acceptance of the imaging detector is not limiting the spatial extent of the observed images and also indicates that the angular distribution of the ethyl radicals leaving the surface is extremely narrow and peaked along the surface normal. This is not unexpected for a "prompt" photofragmentation process on the surface, in which the fragment, ethyl radical in this case, is ejected from the surface without secondary collisions.[32]

To gain some insight into the angular distribution of photodesorbing ethyl radicals, the

images of mass 29 were analyzed to yield angular distributions for ethyl radicals desorbing in the horizontal direction (i.e., parallel to the [001] direction of the surface). Data from the 3 central rows of the2D images for mass 29 were averaged together and plotted as a function of angle as shown in Figure 4.4. These raw data from $-30°$ to $+30°$ were fit to a Gaussian function of the form

$$S(\theta) = A \exp\left[-\frac{1}{2}\left(\frac{\theta - \theta_0}{b}\right)^2\right] \tag{4.1}$$

where S represents signal intensity, A represents amplitude, θ_0 represents the center angle of the distribution, and b represents the distribution width parameter. This fitted function was normalized and divided by the normalized detector function to yield the correct angular distribution for the "slow" channel (59 μs) shown in Figure 4.5(a) and for the "fast" channel (24.6 μs) shown in Figure 4.5(b). There are more data points for the fast channel because, as previously described, the faster ions are not focused as tightly and thus occupy more space on the detector. This results in the angular distribution data being spread over a larger number of pixels and thus gives more data points for a given angular spread. As is common for the analysis of photodesorption angular distributions,[32] the data were fit to functions of the form $\cos^n(\theta)$. It was found that $n = 39.5$ for the slow channel whereas $n = 39.0$ for the fast channel. The fact that these exponent values are nearly identical shows that the angular distributions for ethyl photofragments ejected from the surface do not depend on kinetic energy.

The ion images in Figure 4.3 also shed light on the origin of masses 27 and 28. As noted above, the larger spatial images of the mass 27 and 28 fragments relative to mass 29 could be due to differences in angular distributions or transverse velocity components induced by fragmentation in the ionization region. Previous work by Henderson[41] using electron impact ionization detection had assigned masses 27-29 to ionic fragments resulting primarily from ethane (C_2H_6) and ethylene (C_2H_4) which are formed via secondary reaction products of ethyl radicals on the hydroxylated titania surface. More recently, Wilson et al.[16] using

"soft" VUV ionization were able to show that neither ethane or ethylene are formed under UHV photooxidation conditions, and that dissociative ionization of the ethyl photoproduct was likely to be the source of fragments at masses 27 and 28. Additional support for the dissociative ionization mechanism is provided by the comparison of the experimental horizontal cuts for masses 27 and 28 and the calculated detector functions shown in Figure 5. In the case of dissociative ionization, we expect the daughter fragments to gain transverse momentum relative to the motion of the neutral parent, depending on the dynamics of the ionic fragmentation process induced by VUV photoionization. The spatial and energy distribution of the daughter fragments will depend on the lifetime and excess energy of the excited cation intermediate (ethyl radical ion), and fragments moving transverse to the ethyl radical direction would be expected. Hence, daughter ions resulting from dissociative ionization of ethyl radical should exhibit broader angular distribution than the parent ion. At both pump-probe laser delays, the horizontal angular distributions broaden with decreasing mass. This observation is consistent with a sequential dissociative ionization mechanism in which the formation of mass 27 has experienced two fragmentation events and consequently more transverse "kicks" than mass 28, or by a single-step dissociation in which a fragment of higher mass (H_2 for mass 27 as opposed to H for mass 28) is ejected. The most convincing evidence of dissociative ionization comes from the mass 27 image at the longer pump-probe delay (59 μs). In this image, the experimental horizontal angular distribution extends to angles as large as $\pm 60°$, which are beyond the limits of the detector function. Since it is physically impossible for a neutral fragment originating from the surface to reach the detector at angles larger than 30°, mass 27 must result from fragmentation within the mass spectrometer, i.e., from dissociative ionization. In the case of mass 28, dissociative ionization leads to broader angular distributions than the ethyl parent ion, but still within the acceptance limits of the detector. Nonetheless, the combination of angular broadening and our earlier final state energy distributions provides strong evidence that mass 28 is also a daughter fragment of the primary ethyl radical photoproduct.

4.5 Conclusions

The results presented in this paper are in close agreement with those of previous pump-probe studies of 2-butanone photooxidation on TiO_2(110), which used measurements of final state energy distributions to conclude that the three product ions with masses 27-29 originate from a common neutral photoproduct, i.e., ethyl radical, via dissociative ionization.[16,41] While the use of final-state information can provide fairly conclusive evidence of parent ion fragmentation, the ion imaging approach demonstrated in this work provides an effective alternative and has the added benefit of providing the necessary data in a fraction of the time. In particular, the use of the PImMS technique allows us to explore the spatial distribution of multiple ions simultaneously, and thereby increases the amount of data that can be obtained in a single experiment. This is especially important for surface photochemistry experiments in which the photoactive sample on the surface is fixed and consumed during the measurement. For example, final state measurements of individual masses in a pump-probe experiment require multiple runs, each of which requires a new sample dose onto the crystal, and in some cases also requires crystal cleaning in between runs. By comparison, the sample in a gas-phase photochemistry experiment is essentially continuous, so data acquisition and signal averaging are much less constrained. The ability of the PImMS camera to provide temporal and spatial information for all photoproducts simultaneously allows certain quantitative comparisons to be made for data obtained within a single run. This is typically not possible when taking data on different days because of variations in experimental conditions. The multi-mass imaging capabilities of the PImMS camera provide a significant enhancement in the ability to study the dynamics of complex surface photoreactions such as 2-butanone photooxidation on TiO_2(110).

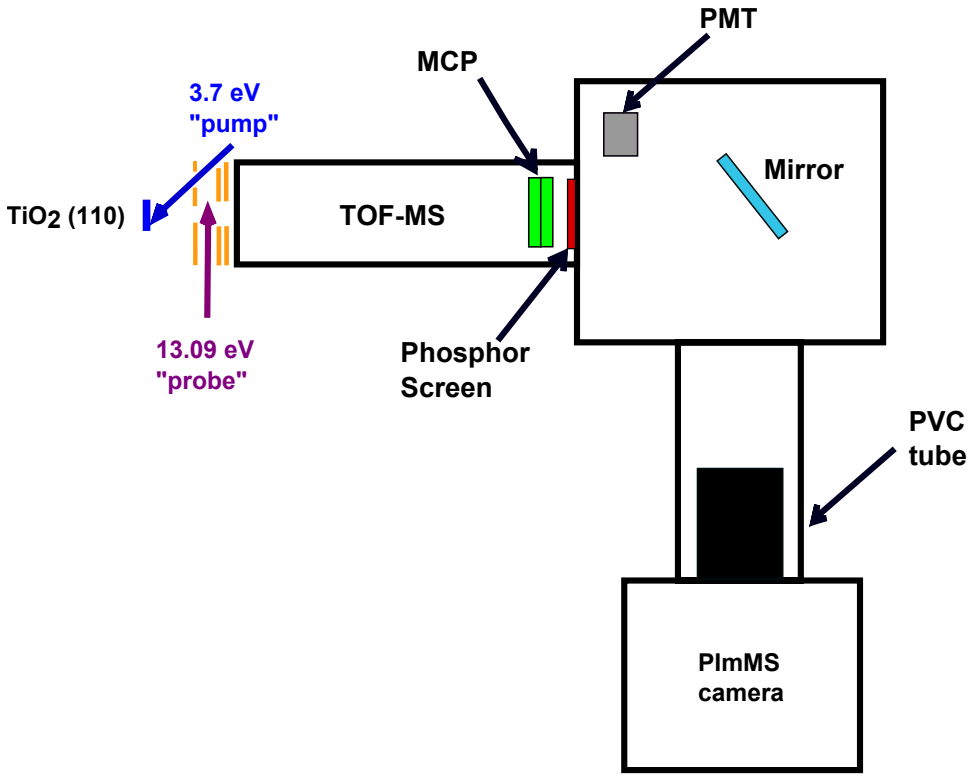

Figure 4.1: A view of the experimental setup showing the necessary modifications required to accommodate the PImMS camera.

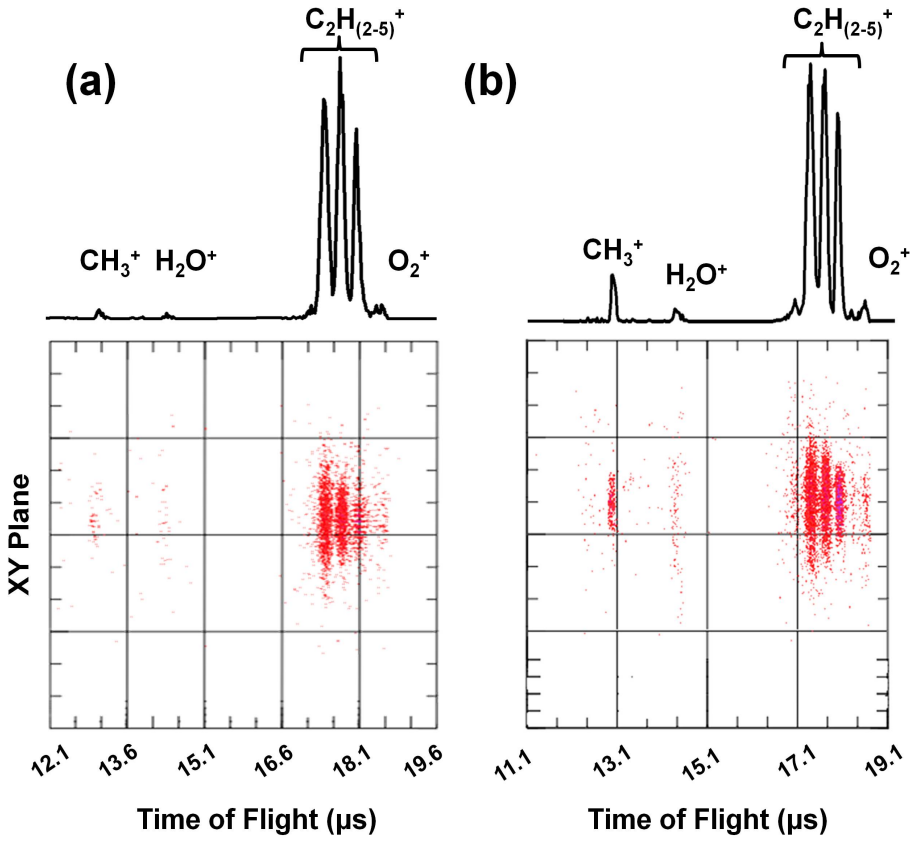

Figure 4.2: Time-of-flight mass spectra taken for both (a) slow and (b) fast channels. Below each mass spectrum is the data in its 3D form where the horizontal axis represents time and the vertical axis represents the detector plane with units of pixels. The 3D images have been rotated slightly about the time axis to better illustrate the ion clouds. Thus, the vertical axes do not correspond to single detector axis (i.e., x or y) but rather some arbitrary combination of the two.

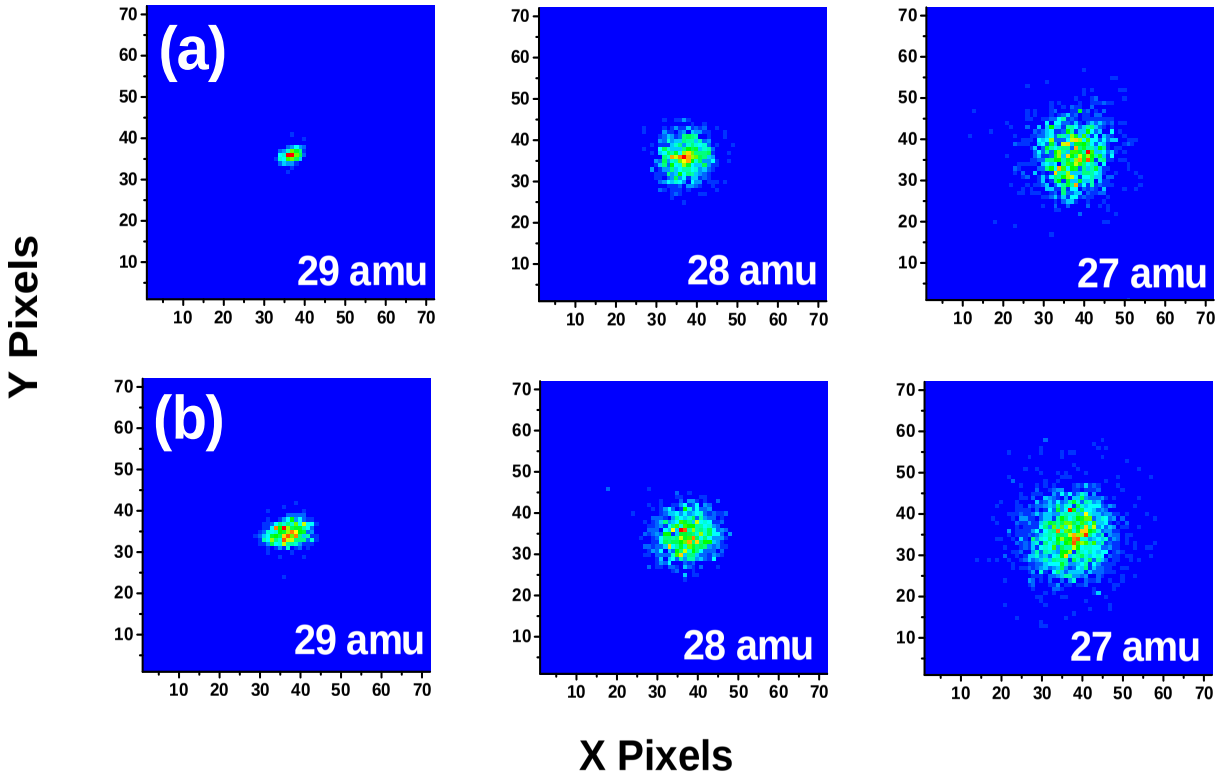

Figure 4.3: Two-dimensional images of masses originating from ethyl radical and its fragments. Panel (a) shows images of(from left to right) ethyl radical (mass 29), mass 28, and mass 27 taken at a 59 μs laser delay. Panel (b) shows images of the same three masses but at a 24.6 μs laser delay.

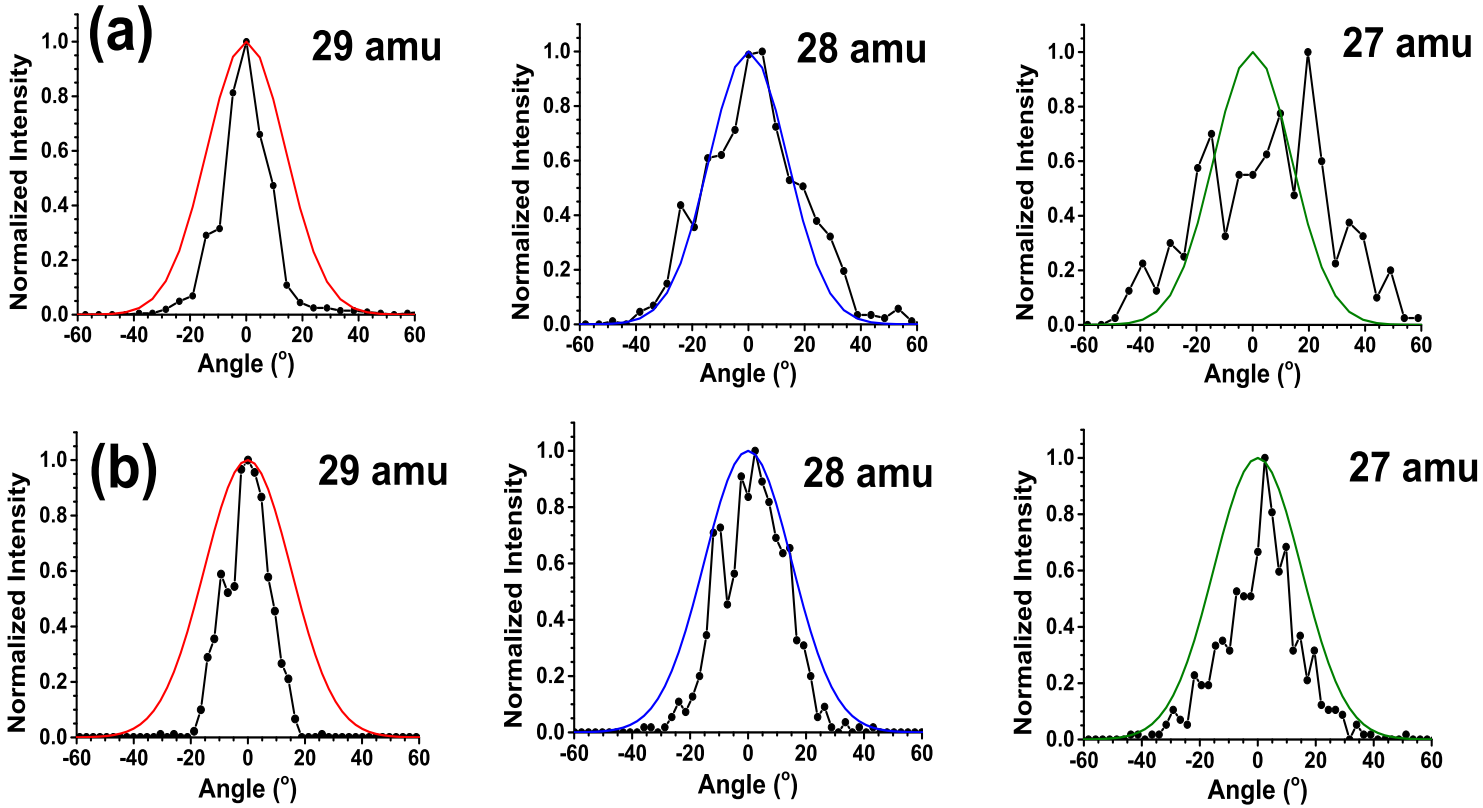

Figure 4.4: Horizontal cross sections taken for images of masses 29-27 (left to right) at (a) 59 μs laser delay and (b) 24.6 μs laser delay. For data taken at the longer delay, the degree of fragmentation for ethyl radical is quite severe and there is signal which falls outside of the limits imposed by our detector function. Fragmentation does not appear to be as severe for data taken at the shorter delay, although there is a clear broadening of the distribution for masses 28 and 27.

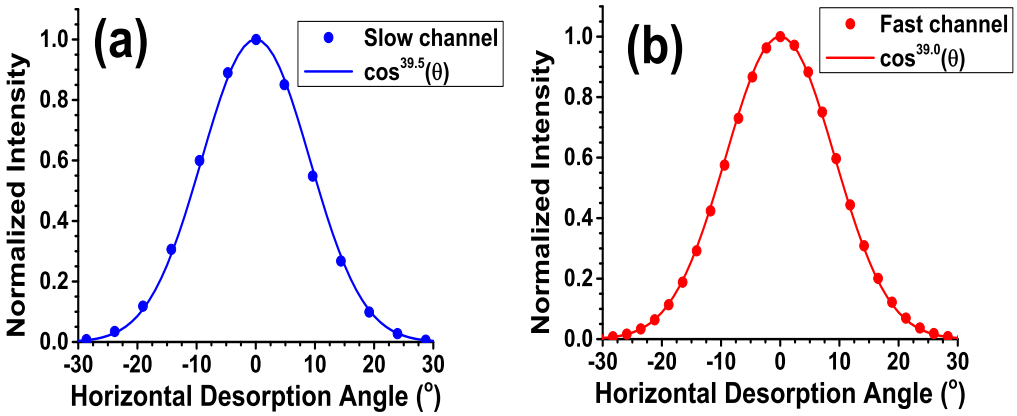

Figure 4.5: Angular distributions of ethyl radical desorption for the (a) slow and (b) fast channels along with $\cos^n(\theta)$ fits to the data. For the slow channel $n = 39.5$ and for the fast channel $n = 39.0$. The angular distribution of ethyl radicals is essentially the same for both kinetic energies studied in this work.

5 Photooxidation of ethanol and 2-propanol on TiO_2(110): evidence for methyl radical ejection

This section was published in *Phys. Chem. Chem. Phys.*, 2013, **15**, 17976-17982.

5.1 Introduction

The photocatalytic decomposition of organic molecules on TiO_2 surfaces is a subject that has been well-studied in recent years.[1,6] Interest in this class of reactions is motivated, in part, by the application of TiO_2 photocatalysts for the destruction of toxic compounds in the environment. Given that ethanol and 2-propanol (isopropyl alcohol) are used extensively as solvents in both home and industrial settings, understanding the photocatalytic decomposition of these molecules is particularly important. Ethanol, in particular, has attracted some additional interest from researchers in the renewable energy field as there is evidence that it can be photodecomposed on Au-TiO_2 nanoparticles to produce hydrogen.[72,73]

The thermal and photochemical reactions of ethanol and 2-propanol on TiO_2 have been studied extensively on both powder catalysts[25,72,74–92] and single crystal surfaces.[93–107] Fundamentally, it is known that the first step in the photooxidation of ethanol and 2-propanol involves the photocatalytic dehydrogenation to acetaldehyde and acetone respectively. However, the mechanism by which these reactions proceed toward their final products (i.e. CO_2, H_2O) remains somewhat ambiguous. On the other hand, recent work on ketone photooxidation has shown that acetaldehyde and acetone (along with co-adsorbed oxygen) photooxidize via methyl radical ejection.[14,15,17,108] In this paper, we have investigated the photooxidation of ethanol and 2-propanol under ultrahigh vacuum (UHV) conditions using a combination of temperature programmed desorption (TPD) measurements and time-of-flight mass spectrometry (TOF-MS) combined with state-resolved laser ionization of desorbing photoproducts. We present results which show that when these adsorbed alcohols are irradiated with ultraviolet light in the presence of oxygen at low temperature, methyl radicals are ejected

into vacuum. As will be shown below, the results presented in this work indicate that these methyl radicals originate from secondary photooxidation of the aldehyde/ketone intermediates formed by the initial photo-dehydrogenation of the alcohols.[15,17]

5.2 Experimental

The surface was cleaned on a daily basis by Ar^+ sputtering (300 K, 0.5 keV, 10 min) and annealing (850 K, 30 min) and was annealed for 10 min at 850 K in between each TPD and photochemistry measurement. Research grade oxygen was obtained from Matheson Tri-Gas and was used without any additional purification. Ethanol (200 proof, HPLC grade) and 2-propanol ($> 99.5\%$) were obtained from Sigma-Aldrich and were purified by multiple pump-freeze-thaw cycles. The alcohol coverages reported below are estimates based upon a comparison between our TPD data and previously published results.[105]

Methyl radical detection was performed using a REMPI scheme cooresponding to the 0_0^0 band of the $^2A_2''(4p_z) \leftarrow\leftarrow \tilde{X}^2A_2''$ two-photon transition of the methyl radical.[36] To excite this transition, Pyrromethene 597 dye dissolved in ethanol was used in the probe laser to produce visible light at 572.6 nm which was subsequently doubled to 286.3 nm. The probe laser was tightly focused at a distance of 29 mm from the TiO_2 surface, parallel to the crystal face. Once ionized, methyl radicals were detected by TOF-MS.

5.3 Results

5.3.1 TPD and photodesorption results

The photooxidation of ethanol and 2-propanol was initially studied by performing post-UV irradiation TPD measurements. Fig. 5.1 shows a series of three ethanol TPD spectra (m/z: 29 amu) under various conditions. Mass 29 signal was monitored in these experiments as it can be used as a fingerprint for both ethanol and acetaldehyde desorption. Fig. 5.1a represents a $\sim$ 0.8 ML dose of ethanol in the absence of UV irradiation, Fig. 5.1b is for

a similar ethanol dose after a 5 min UV exposure in the absence of molecular oxygen and Fig. 5.1c represents a 5 min UV exposure in a background atmosphere of oxygen (5×10^{-8} Torr). All samples were dosed and irradiated at a surface temperature of 105 K prior to the TPD scan. During the TPD experiments presented here, the crystal temperature was increased linearly at a rate of 2 K/s. In Fig. 5.1a, three main desorption features are present in the TPD spectrum. The feature at $\sim$ 300 K is attributed to ethanol desorption from Ti^{4+} sites while the feature between 550 and 650 K is attributed to recombinative desorption involving ethoxy groups and H atoms bound to bridging oxygen rows.[105] The feature at $\sim$ 375 K is attributed to ethanol desorption from defect sites, as this feature is not present on an oxidized surface (data not shown). A similar feature was observed by Bondarchuk et al. in TPD studies of 2-propanol on TiO_2 and was shown to be more prominent on surfaces with a higher concentration of oxygen vacancies.[93] In agreement with previous work, UV irradiation of adsorbed ethanol produces a low temperature desorption peak which appears around 200 K.[106] This peak can be assigned to the formation of adsorbed acetaldehyde which results from the photocatalytic dehydrogenation of ethanol. As shown by others,[99,107] irradiating adsorbed ethanol in the presence of molecular oxygen enhances the amount of acetaldehyde formed. This effect is attributed to electron transfer to O_2 which behaves as a charge trap and thus suppresses electron-hole recombination.[107] The enhancement of acetaldehyde formation by adsorbed oxygen is seen in Fig. 5.1c where the desorption feature near 200 K is significantly larger than without oxygen in Fig. 5.1b.

Assuming that acetaldehyde formed by ethanol dehydrogenation undergoes subsequent photooxidation to formate by ejection of a methyl radical,[17,108] we would expect formate to build up on the surface during UV irradiation. The latter can be detected by post irradiation TPD experiments that monitor its high temperature decomposition to CO. Specifically, Zehr and Henderson used ^{13}C labeled acetaldehyde to show that the decomposition of surface-bound formate occurs between about 500-700 K by monitoring ^{13}CO TPD signal (m/z: 29 amu).[108] Isotopically labeled ethanol was not used in this work which made it difficult to

detect formate decomposition since CO (28 amu) is already present as a background gas in the vacuum system. In addition, mass 28 is also a major cracking fragment of gas-phase ethylene which is a known dehydration product of ethanol that desorbs in the same temperature region.[101,102]

As an alternative method for detecting secondary acetaldehyde photooxidation, we used state-resolved REMPI to observe the photodesorption of methyl radicals in real time. For these experiments, the TiO_2 surface was dosed with $\sim$ 0.8 ML of ethanol at 105 K and placed in a 5×10^{-8} Torr background of O_2. The prepared sample was positioned in front of the TOF-MS on the bottom level of the chamber and was irradiated with the UV pump laser beam. The pump-probe delay (19 μs) was chosen to selectively ionize "fast" methyl radicals[15,17] (see next section). The CH_3^+ ion signal was then recorded as a function of irradiation time for $T_s \approx$ 100 K, 250 K and 300 K as shown in Fig. 5.2a-c, respectively. Methyl radicals were also observed if oxygen ($\sim$ 80 L) was co-dosed on the surface prior to UV exposure instead of the surface being exposed to a background pressure of O2 (data not shown). Fig. 5.2d represents CH_3^+ signal recorded at 100 K without any oxygen present to show that the presence of oxygen is necessary for methyl radical ejection to occur. It is clear from this data that the methyl radical photoyields are strongly dependent on surface temperature. Considering these results along with the TPD data shown in Fig. 5.1, it is possible to correlate the observed temperature dependence of the methyl photoyield with acetaldehyde desorption at $\sim$ 200 K. Below this temperature, acetaldehyde is bound to the surface and can be readily photooxidized in the presence of oxygen.[108] However, as the temperature is increased to 250 and 300 K, the fraction of acetaldehyde remaining on the surface is greatly diminished (see Fig. 5.1). Therefore, it is not surprising that the photodesorption yield for methyl radical decreases significantly at temperatures higher than 100 K. The data in Fig. 5.2 also suggest that the rates of methyl photodesorption vary with surface temperature. In particular, the faster initial photodesorption rate seen at 250 K compared to 100 K might be indicative of a larger fraction of the adsorbed acetaldehyde being tied up as an acetaldehyde-oxygen

complex (e.g., diolate) due to reaction with co-adsorbed oxygen. The latter is thought to be the photoactive species for photooxidation and its formation is known to be thermally activated at temperatures above $\sim$ 175 K.[14,108] As mentioned earlier, the data presented in Fig. 5.2d provides additional evidence for the participation of oxygen in the photooxidation pathway that leads to methyl photoproducts and surface-bound carboxylate species.

Analogous to ethanol photooxidation discussed above, UV irradiation of adsorbed 2-propanol results in dehydrogenation to acetone, which in the presence of adsorbed oxygen should then proceed via methyl radical ejection to produce a surface bound acetate species. As shown by Henderson, acetate adsorbed on the TiO_2(110) surface decomposes at high temperature to produce gas-phase ketene (42 amu).[14] Likewise, mass 42 is also a prominent cracking fragment for propene which, just like in the case of ethanol, is a thermal dehydration product of 2-propanol produced at high temperature.[101,102] As an alternative, we used mass 21 to track acetate decomposition because this cracking fragment appears in the electron impact ionization mass spectrum for ketene but not for propene.[109] Fig. 5.3a shows a TPD spectrum for $\sim$ 0.6 ML of 2-propanol in the absence of UV irradiation where the assignment of the observed peaks is analogous to that of ethanol. The peak at $\sim$ 300 K is attributed to 2-propanol desorption. This can be explained by noting that mass 42 is a minor cracking fragment of 2-propanol and the mass 21 signal is its doubly ionized counterpart. The TPD shown in Fig. 5.3b was taken after irradiating a similar alcohol coverage for 10 min in an O_2 background (5×10^{-8} Torr) using a photon fluence of 2.6×10^{16} photons $s^{-1} \cdot cm^{-2}$. Following this treatment it is clear that new, high temperature peaks are present in the TPD spectrum for mass 21 (or singly charged fragments at mass 42). In comparing this spectrum to post UV irradiation TPD experiments measured for acetone, we believe that these new peaks are indicative of thermal decomposition of acetate on TiO_2(110) which is formed by photooxidation of acetone.[14,15] As will be shown in the following section, pump-probe measurements of methyl radical ejection from alcohol-oxygen adlayers indicate that photodesorbing methyl radicals are secondary photoproducts produced as a result of the

photooxidation of the primary aldehyde/ketone photoproducts.

5.3.2 Methyl radical kinetic energy distributions

The results discussed in the previous section, provide clear evidence for the photodesorption of methyl radicals during the photocatalytic oxidation of ethanol and 2-propanol. To gain further insight into the photooxidation mechanism of these alcohols, we used pump-probe laser ionization techniques to determine the methyl radical kinetic energy distributions. Of particular interest was the possibility of using the methyl fragment energy distributions as a signature property of their molecular origin on the surface by comparison with previous pump-probe studies of methyl ejection from acetone and acetaldehyde photooxidation on $TiO_2(110)$.[15,17] For the purposes of these experiments, the surface was prepared by dosing 80 L of oxygen at 105 K followed by a saturation dose of alcohol. The alcohol-oxygen adlayer was then flashed to 200 K to desorb any multilayer alcohol that may have been present. Methyl radical arrival time distributions were obtained by recording ion signal (15 amu) as a function of pump-probe delay. The photon flux used in these experiments was 5×10^{11} photons $s^{-1} \cdot$ cm^{-2}. The use of a lower photon flux (as compared to other measurements presented here) was necessary to ensure that the depletion rate of methyl radicals from the surface was sufficiently slow to allow for the measurement of their velocity distribution. The arrival time data was then corrected for the depletion of surface coverage during the experiment and smoothed twice using a 3-point average smoothing algorithm. The kinetic energy distributions were derived by using the neutral flight distance for methyl radical and the appropriate Jacobian transformation to convert the experimental data from the time domain to the energy domain.

The resulting methyl radical translational energy distributions for ethanol and 2-propanol photooxidation are shown in Fig. 5.4. The methyl energy distributions for both molecules are bimodal with a "fast" and "slow" channel. To obtain information on the two fragmentation channels, the energy data was fit to a function of the form

$$P(E_K) = AE_K^i(1 - E_K)^j + BE_K^m(1 - E_K)^n \tag{5.1}$$

where the first and second terms represents the energy distributions of the "slow" and "fast" channels, respectively. These functions are similar in form to those derived by Muckerman[110] to describe the prior (statistical) distributions following photodissociation of a polyatomic molecule and were recently used by Goncharov, et al., to fit the kinetic energy distributions of CO fragments resulting from the photolysis of gas-phase acetone.[111] In performing least-squares fits of the data, the parameters A, i, j, B, m, and n were freely varied to obtain the best fit to the experimental results. For the purposes of this work we are not attempting to assign a physical significance to any of these parameters. The goal is only to obtain a best fit to the experimental results so that mean energies for individual channels can be determined.

The fits to the energy data in Fig. 5.4 were used to obtain the methyl radical average kinetic energies presented in Table 5.1. While the average energies of the "slow" channels are similar for the two alcohols, the "fast" methyl radicals from 2-propanol photooxidation have a significantly higher average energy than from ethanol photooxidation. A similar trend was observed by Wilson et al. for methyl radicals produced from ketone photooxidation on $TiO_2(110)$.[17] In that work it was observed that for the photooxidation of heavier ketones, more kinetic energy was imparted to the methyl radical as it was ejected from the surface. In comparing the methyl radical energies measured in the present work to those obtained from ketone photooxidation, the value of $\langle E_{fast} \rangle = 0.15$ eV for ethanol photooxidation compares favorably to the value of $\langle E_{fast} \rangle = 0.162$ eV for acetaldehyde photooxidation.[17] Additionally, the value of $\langle E_{fast} \rangle = 0.20$ eV for 2-propanol photooxidation is comparable to the values obtained for acetone photooxidation which were either 0.183 eV or 0.197 eV depending on the irradiation wavelength used.[15] For these comparisons, it is important to mention that the fitting procedure used in the previous work for extracting "slow" and "fast" translational energies did not use the function used here. Since there is considerable overlap between fast

and slow channels, extracting values for $\langle E_{slow} \rangle$ and $\langle E_{fast} \rangle$ is dependent upon how the data is fit. Therefore the minor discrepancy between the values reported here and those reported previously is likely due to differences in fitting procedures.

Given the similarities between the methyl radical energy distributions measured in this work with those previously measured for acetaldehyde and acetone, i.e., bimodal distributions with very similar average energies, it is likely that the methyl radicals observed during the photooxidation of ethanol and 2-propanol on $TiO_2(110)$ originate from the initial dehydrogenation photoproducts, acetaldehyde and acetone, respectively. As will be discussed in the following section, the use of a state-resolved (REMPI) ionization scheme allows us to easily identify neutral methyl radicals as the photodesorbing species under the conditions studied.

5.4 Discussion

Previous fundamental studies of alcohol photooxidation have attempted to monitor the desorption of photoproducts in real time. In particular, recent experiments aimed at understanding ethanol photooxidation on $TiO_2(110)$[107] and RuO_x/Ru-modified $TiO_2(110)$[104] surfaces both used a QMS to observe gas-phase species produced under UV irradiation of adsorbed ethanol. In these experiments, which were conducted at 300 K, acetaldehyde was observed as the major photoproduct. This result is consistent with previous TPD measurements made by Zehr and Henderson[108] which showed that for coverages approaching 1 ML, a large fraction (but not all) of acetaldehyde thermally desorbs from $TiO_2(110)$ at temperatures below 300 K. In the post UV-irradiation TPD measurements presented in Fig. 5.1 and elsewhere,[106] most of the acetaldehyde photoproduct desorbs by 300 K. Hence, it is not surprising that others have not observed methyl radical ejection during ethanol photooxidation at room temperature. In fact, Kundu and co-workers attempted to look for methyl radical (15 amu) signal during their photodesorption measurements but found that this signal tracked with acetaldehyde desorption.[104] Given that CH_3^+ is a major cracking fragment for acetaldehyde[109]

($\sim$ 35% of 29 amu signal intensity) when using electron impact ionization and QMS detection, it is necessary to remove contributions to the mass 15 signal from acetaldehyde fragmentation to obtain information on the photoyield of neutral methyl radicals.

In the present work, the use of state-resolved REMPI detection of desorbing methyl radicals eliminates the problem of separating signal contributions from ion fragmentation since the REMPI probe only ionizes neutral methyl radicals ejected from the surface. Additionally, since the kinetic energy measurements were performed at $\sim$ 100 K, acetaldehyde photoproducts will be thermally trapped on the surface and will photooxidize to produce gas-phase methyl radicals and surface-bound formate. Of course, as shown in Fig. 5.2c, running this reaction at 300 K results in a non-negligible methyl radical signal which most likely originates from the acetaldehyde species that do not desorb from the surface. Therefore, even under ambient temperatures, we should expect that acetaldehyde does photooxidize via methyl radical ejection. For those acetaldehyde molecules which remain on the surface, photooxidation via methyl radical ejection represents a plausible mechanism which would account for the surface-bound carboxylate species observed by others.[99,104,107]

Based on what is already known regarding 2-propanol photooxidation on TiO_2, we should expect that the photooxidation mechanism for this molecule is similar to that of ethanol. Just as in the case of ethanol photooxidation, the secondary photooxidation of acetone photoproducts is likely to be desorption limited. This conclusion is consistent with TPD measurements by Brinkley and Engel[95] as well as Henderson[20] which show that a significant amount of acetone desorbs from TiO_2(110) below 300 K for coverages approaching 1 ML. In fact photochemistry measurements using molecular beam scattering techniques show that acetone photoproducts desorb from the surface at $T_s \approx 350$ K.[95] Therefore under conditions where acetone remains trapped on the surface long enough for further reaction to occur, photooxidation via methyl radical ejection is a likely pathway for decomposition.

In light of the results presented in this work, we propose a mechanism for ethanol and 2-propanol photooxidation on TiO_2 in Fig. 5.5 where R=H in the case of ethanol and R=CH_3

in the case of 2-propanol. We leave open the possibility for either molecular alcohol or alkoxy groups as the initial species in the reaction as, under the conditions employed in this work, both species are likely to be present on the surface. In the case of methanol photooxidation on TiO_2(110), Shen and Henderson showed that methoxy species (formed in the presence of O-adatoms) are more photoactive than methanol.[112] By analogy, it is possible that the alkoxy species are more photoactive in the initial dehydrogenation of ethanol and 2-propanol. This result also suggests that co-adsorbed oxygen may play an additional role (aside from diolate formation) in promoting the photocatalytic oxidation of these molecules. The first step in ethanol and 2-propanol photooxidation is the photocatalytic dehydrogenation of these species to acetaldehyde/acetone. In the second step, an acetaldehyde/acetone-oxygen complex forms and is subsequently photooxidized to formate/acetate via methyl radical ejection.[14,15,108]

5.5 Conclusion

Results obtained using TPD as well as pump-probe laser ionization techniques have shown that methyl radicals are produced during the photocatalytic oxidation of ethanol and 2-propanol on TiO_2(110). Methyl radical energy distributions obtained for ethanol and 2-propanol photooxidation are in close agreement with those obtained for acetaldehyde and acetone respectively. These results support a mechanism in which methyl radicals produced during alcohol photooxidation are secondary photoproducts which originate from photooxidation of the primary aldehyde/ketone photoproducts.

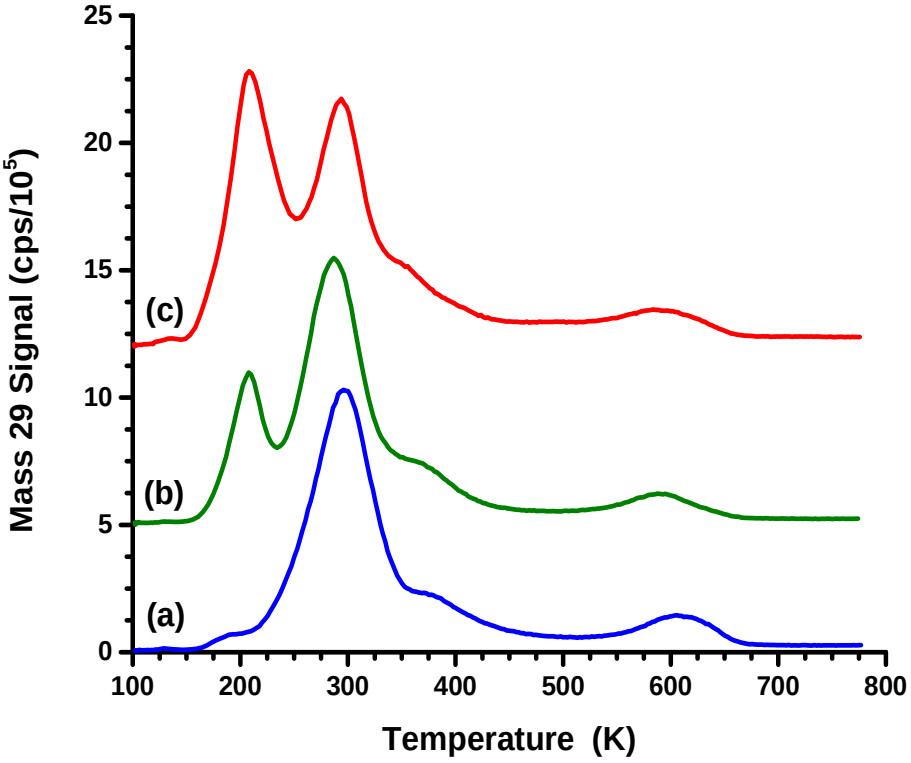

Figure 5.1: Ethanol TPD spectra showing signal for 29 amu for (a) no UV irradiation, (b) irradiation of ethanol in the absence of oxygen (c) irradiation of ethanol in 5×10^{-8} Torr of O_2. For curves b and c, the sample was irradiated for 5 min using a photon flux of 2.6×10^{16} photons$\cdot s^{-1} \cdot cm^{-2}$. For all three experiments, the ethanol coverage is estimated to be ~ 0.8 ML. Spectra are vertically offset for clarity.

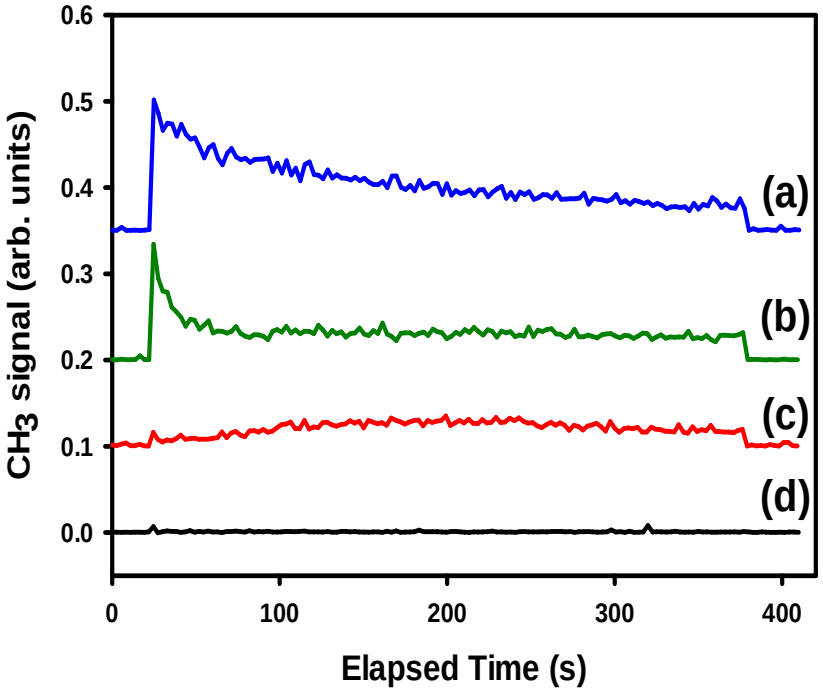

Figure 5.2: Methyl radical depletion measurements taken at (a) 100 K, (b) 250 K, (c) 300 K and (d) 100 K without oxygen. These samples were irradiated using a photon flux of 2.6×10^{16} photons$\cdot s^{-1} \cdot cm^{-2}$, in the case of (a)-(c), a background oxygen atmosphere of 5×10^{-8} Torr. Individual curves are vertically offset for clarity.

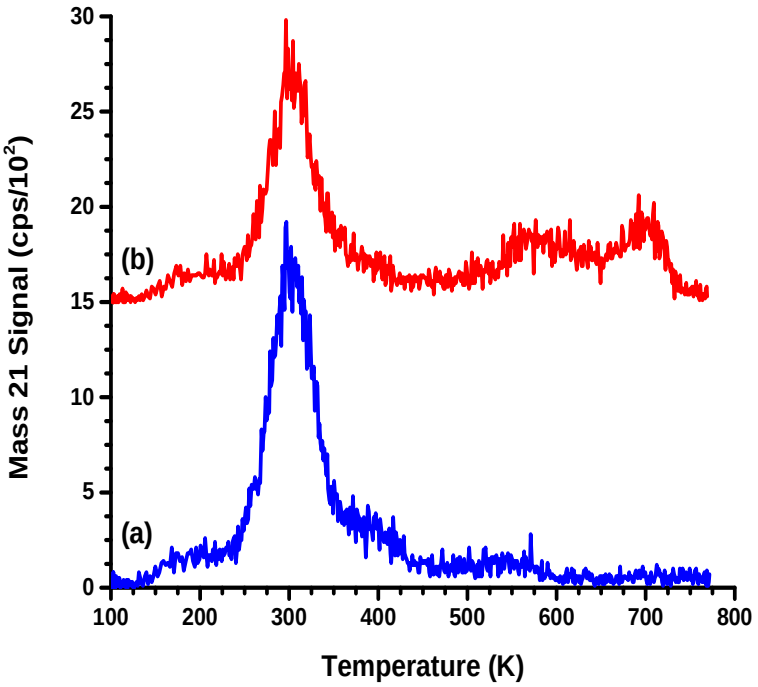

Figure 5.3: 2-Propanol TPD spectra showing signal for m/z = 21. Spectrum (a) represents a 2-propanol dose of ~ 0.6 ML in the absence of UV irradiation while spectrum (b) represents the same dose of 2-propanol irradiated for 10 min in 5×10^{-8} Torr of O_2 using a photon flux of 2.6×10^{16} photons$\cdot s^{-1} \cdot cm^{-2}$

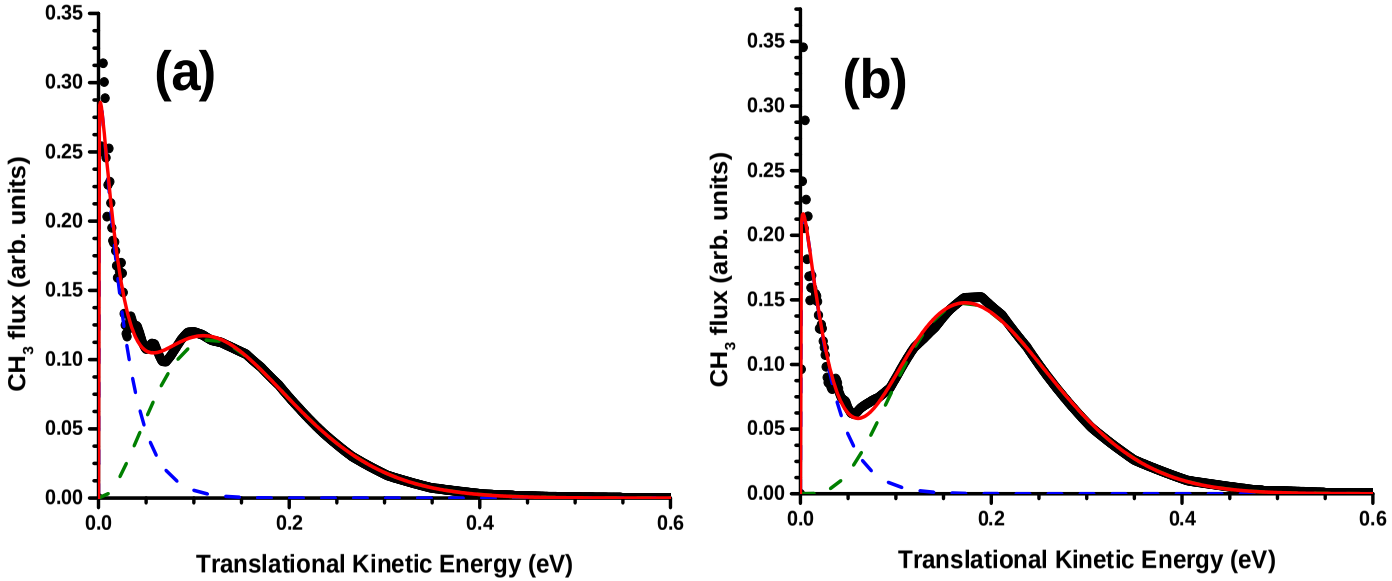

Figure 5.4: Methyl radical kinetic energy distributions for (a) ethanol and (b) 2-propanol. Solid points represent experimental data, dashed lines represent fits for fast and slow channels and the solid trace represents the overall fit.

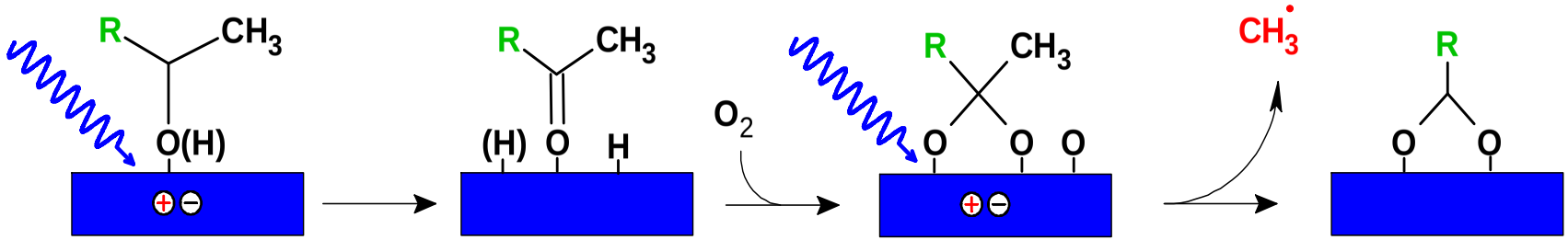

Figure 5.5: Mechanism of ethanol and 2-propanol photooxidation on $TiO_2(110)$. R = H in the case of ethanol photooxidation and R = CH_3 in the case of 2-propanol photooxidation.

Molecule	$\langle E_{fast} \rangle$	$\langle E_{slow} \rangle$	$\langle E_{tot} \rangle expt.$
Ethanol	0.15	0.03	0.12
2-Propanol	0.20	0.03	0.17

Table 5.1: Mean kinetic energies for desorbing methyl radicals produced following ethanol and 2-propanol photooxidation. Values are in units of eV and have an estimated uncertainty of 10%. This uncertainty is derived from the error in measuring the neutral flight distance between the surface and ionization region of the TOF-MS

6 Design of an Imaging TOF-MS for Ultrafast Surface Studies

In the experiments discussed so far, the kinetic energy and vibrational energy of methyl radicals was probed by first initiating reaction with one laser pulse and ionizing the radical with a second pulse (or multiple pulses) after the radical traveled several millimeters from the surface. While this approach has more than enough temporal resolution for kinetic energy measurements, it is completely inadequate for studying the ultrafast dynamics of surface photoreactions. Since ultrafast experiments are conducted on a femtosecond to picosecond time-scale (as opposed to the nanosecond to microsecond time-scale required for kinetic energy measurements), products of interest must be ionized directly at the surface.

The only practical way to accomplish this is to design an imaging TOF-MS where the crystal surface behaves as the first (repeller) electrode. An example of this design has been detailed by the Wodtke group in their study of KBr surface photochemistry.[54,61] While this design works well for this experiment (which doesn't require constant movement of the crystal for cleaning and dosing), it does not lend itself to experiments where the sample must be moved around often.

In this chapter, the design of a new imaging TOF-MS based upon the designs of Wodtke[54,61] and Koehler[62] will be presented. Construction of this new TOF-MS apparatus is motivated by a desire to both increase the angular acceptance angle for desorbing photoproducts and to enable surface dynamics studies on an ultrafast time-scale. Examples of surface ultrafast studies that could benefit from the use of this detector will be described in the next chapter.

6.1 Construction details

A photograph of the assembled detector is shown in Fig. 6.1 and consists of a 12 lens design. The lenses are machined from 1.2 mm thick 304 stainless steel using a waterjet machine. Each lens has an outer diameter of 100 mm and an inner diameter of 55 mm and has four mounting

holes drilled close to the outer circumference of each lens along with a small clearance hole for high voltage wires to be attached using 0-80 screws and nuts. The fourth and fifth lenses in the stack were machined to include a pair of 10 mm holes for laser beam access to the surface (see Fig 6.2 for a better view of this) at an angle of 45° with respect to the crystal surface normal. The first lens was originally designed to be open with an inner diameter of 55 mm like the rest of the lenses, with the intent that the sample holder would be re-designed with a large faceplate that could fit within the 55 mm hole (for example, see Ji et. al[54]). This idea was abandoned due to concerns regarding crystal cooling and so a 0.005 inch steel foil was spot-welded over the opening and a 10 mm hole was drilled in the center to allow access the surface. The new approach is to place the crystal surface approximately 1 mm in front of the first lens and bias it at a slightly higher voltage to accelerate ions from the surface. The final lens in the detector is actually a stainless steel can that is bolted to the 8 inch side of a 6 to 8 inch zero-length reducing conflat flange using six, 10-32 vented machine screws. The lens stack is assembled as follows: four 4-40 threaded rods are inserted into tapped holes in the can (V_{12}) and long ceramic tubes are placed over these rods to ensure no lens can short to ground. The lenses are then inserted one by one along with additional ceramic tubes which allow the lenses to be offset from one another by 10.2 mm. UHV compatible wires are then attached to each lens to supply the necessary. Once the ion optics assembly is bolted to the machine, a flight tube consisting of a 6 inch conflat spool piece is attached to the back of the assembly and the final step is attaching an imaging MCP/phosphor detector to seal the system. The final distance from the inside face of the first lens to the face of the MCP is 43 cm.

The final piece of hardware needed for the detector is a voltage divider capable of evenly dividing the voltage across the lenses. Since lens 12 is always held at ground potential, a divider capable of supplying 11 variable voltages is required. Following the work of Reid and Koehler,[62] the lens stack is divided into two regions powered by two separate voltage dividing circuits. The first region, consisting of lenses V_1 through V_5 is designed to produce electric

electric fields of approximately 50 V/cm while the second region consisting of lenses V_6 through V_{11} is designed to produce electric fields of approximately 125 V/cm. The circuit diagram is shown in Fig. 6.3. The voltages are supplied using two separate high voltage power supplies (Bertan 210-02R, 0-2kV/0-100mA for the first region and Bertan 205B-03R, 0-3kV/0-10mA for the second region) which can be independently tuned to establish the proper focusing conditions.

6.2 Computer simulations of the detector

In order to figure out the proper voltage ratio between the two regions of the TOF detector, a model of the detector was created using SIMION 8.1 (Scientific Instrument Services Inc.) software which is is capable of calculating the electric fields produced in the mass spectrometer. Once generated, this model can be used to determine the trajectories of ions as a function of applied voltage(s) which is critical for determining the proper conditions for velocity map imaging experiments. A computer rendering of the detector is shown in Fig. 6.4 along with electric field potentials (red lines) and ion trajectories computed for methyl radicals leaving the surface at various angles. The optimum focusing conditions are achieved for $V_{crystal}$ = 1109 V, V_1 = 1100 V and V_6 = 800 V and enable trajectories from 0 to 80° relative to the surface normal to be studied using this detector. As can be seen in Fig. 6.4, the distinct velocity groups (regardless of where the ion was born on the surface) are resolved at the MCP confirming that VMI conditions are satisfied.

It was observed in the computer simulations that the focusing ability of the detector was very sensitive to small changes in the V_1:V_6 ratio as well as in the value of $V_{crystal}$. For example while $V_{crystal}$ = 1109 V was the optimized value for ions originating at the crystal surface, a value of 1107 V was optimum if the ions were born at a distance of 1 mm in front of V_1 (as is the case for the gas phase studies presented in the next section). Generally speaking, the experimental tests of the detector did not seem to indicate a high degree of sensitivity to small voltage differences. Further experimentation is likely needed to

understand why this is so. In particular, it would be desirable to understand the influence on the images as a function of V_{sample} as this has not been thoroughly investigated.

6.3 Preliminary Results - CH_3I photodissociation

To experimentally validate the performance of the detector, the photolysis of CH_3I was studied. This reaction was the first to be imaged by Chandler and Houston[51] and has also been studied by Eppink and Parker[2] using velocity map imaging technique. In this experiment, a linearly polarized laser with its polarization vector oriented parallel the detector plane is used to dissociate methyl iodide through a single photon absorption through its A-band. Following this absorption, methyl iodide decomposes by forming a methyl radical and iodine atom. The much lighter methyl radicals are ejected along the vector defined by the polarization vector and the resulting ion images appear as projections of two opposing half-rings. A wavelength of 286.3 nm was chosen to both dissociate methyl iodide and ionize methyl radicals ($2+1$ REMPI detection) through the $4p_z$ Rydberg state.[36]

In order to extract the kinetic energy information from the CH_3 ion images, an energy calibration using SIMION was performed to relate initial kinetic energy with final position relative to the center of the MCP. In the simulation, a group of CH_3 ions originating at the center of the TOF axis and 1 mm in front of the first lens was flown at an initial trajectory parallel to the detector face. The energy was varied from 0 to 0.9 eV in 0.1 eV increments and the final position recorded. The results are shown in Fig. 6.5 and, as expected, the kinetic energy is proportional to the square of the distance traveled.

The CH_3 ion image recorded using this detector is shown in Fig. 6.6. The image at left is the raw image whereas the the image at right is the image following an inverse-Abel reconstruction performed using a Python implementation[113] of the BASEX algorithm developed by the Reisler group.[114] This step is necessary because the raw image is a 2D projection of a cylindrically symmetric, three-dimensional ion cloud. The image reconstruction thus allows for the full 3D information provided in the experiment to be extracted from this 2D image.

Once the image has been transformed, the kinetic energy spectrum of the methyl radicals can be extracted by summing the pixels over a 2π rotation about the image center. The pixel numbers from the image can be converted to linear distance (mm) and finally to kinetic energy using the calibration curve shown in Fig. 6.5. The pixel to mm conversion is performed by simply recording an image of the phosphor screen which is 40 mm in diameter and using this image to obtain a pixel/mm conversion factor. The final kinetic energy spectrum is shown in Fig. 6.7 along with data taken from Eppink and Parker.[2] The agreement with the literature is reasonably good with an experimental peak position of 0.81 eV as compared with the literature measurement of 0.85 eV. The resolution of the experimental data is clearly less than that of Eppink and Parker, although it is important to note that their experimental apparatus used a well-collimated molecular beam[52] of molecules (dia. $\sim$1 mm) whereas this data was recorded by backfilling the chamber with methyl iodide. The molecular beam approach is advantageous because it defines a small ionization volume at the center of the TOF axis which is where the VMI performance of the detector is best.[52]

It is also possible that further optimization of the setup described here is required. While the performance of this detector in terms of energy mapping appears to be good, it would be better to image another molecule which shows more peaks and thus will enable a calibration over the full detector space. A good candidate is O_2 dissociation at 225 nm which exhibits many features in the velocity mapped images.[52,115]

Once testing and calibration are complete, this detector will be used for studying surface photoreaction experiments in conjunction with a new generation of imaging detector called TimepixCam.[116] TimepixCam is a portable imaging detector developed at Brookhaven National Lab and is based on Timepix sensor technology.[117] Much like the PImMS camera described earlier, the TimepixCam is capable of producing time-resolved images with a resolution of $\sim$ 25 ns on a 256×256 pixel array.[116] Unlike the PImMS camera however, the Timepix sensor pixels can only record single hits per trigger as opposed to PImMS which can record up to four events per trigger. On the other hand, the sensor resolution for Timepix-

Cam is much better than the 72×72 pixel array of the PImMS sensor. For studying ultrafast surface photoreaction dynamics, TimepixCam will be able to provide images and time-of-flight spectra simultaneously. Since the time-of-flight peak for a photodesorbing fragment will contain information about that fragment's kinetic energy distribution, the TimepixCam should allow for angular distributions as a function of kinetic energy to be determined. This is an important advantage since it is not necessarily expected that photoproducts ionized on an ultrafast timescale will possess narrow kinetic energy distributions for a given pump-probe delay. On the other hand, the imaging study of butanone described earlier did produce ion images which were defined over a narrow kinetic energy range because this particular pump-probe experiment was designed to carefully distinguish between products of different kinetic energy. In closing, it is expected that this new VMI TOF-MS coupled with the Timepix-Cam detector will allow for the measurement of photoproduct kinetic energy and angular distribution as related to the femtosecond dynamics of such photochemical reactions.

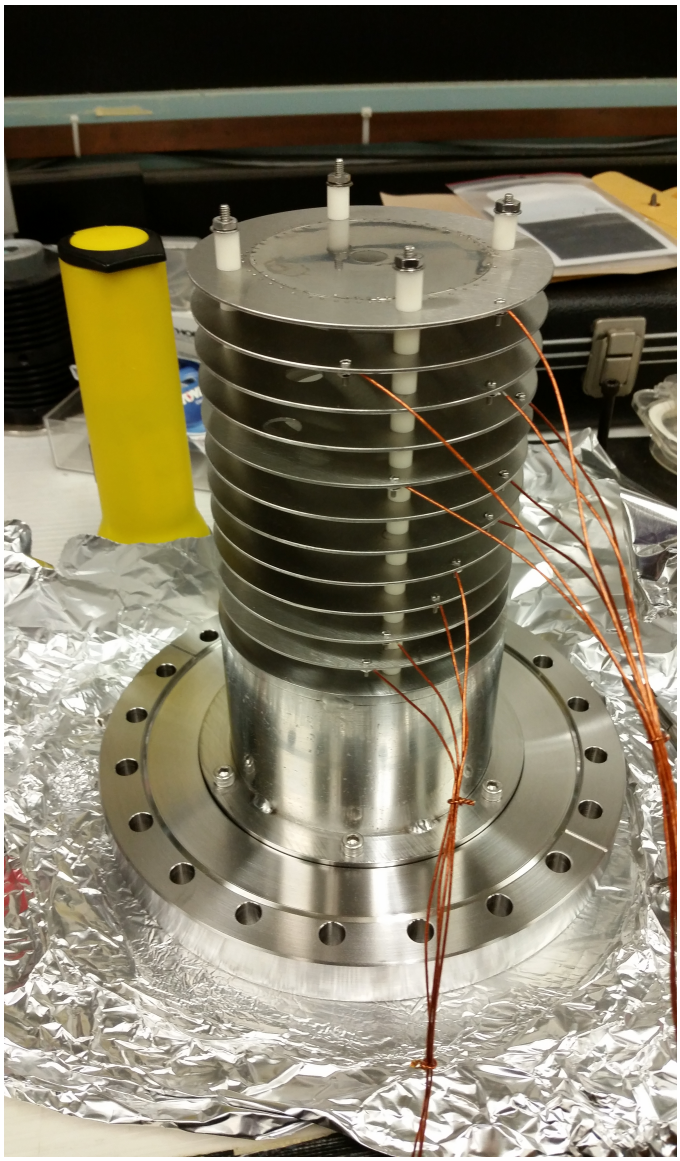

Figure 6.1: Photograph of the fully assembled detector prior to installation on the vacuum system.

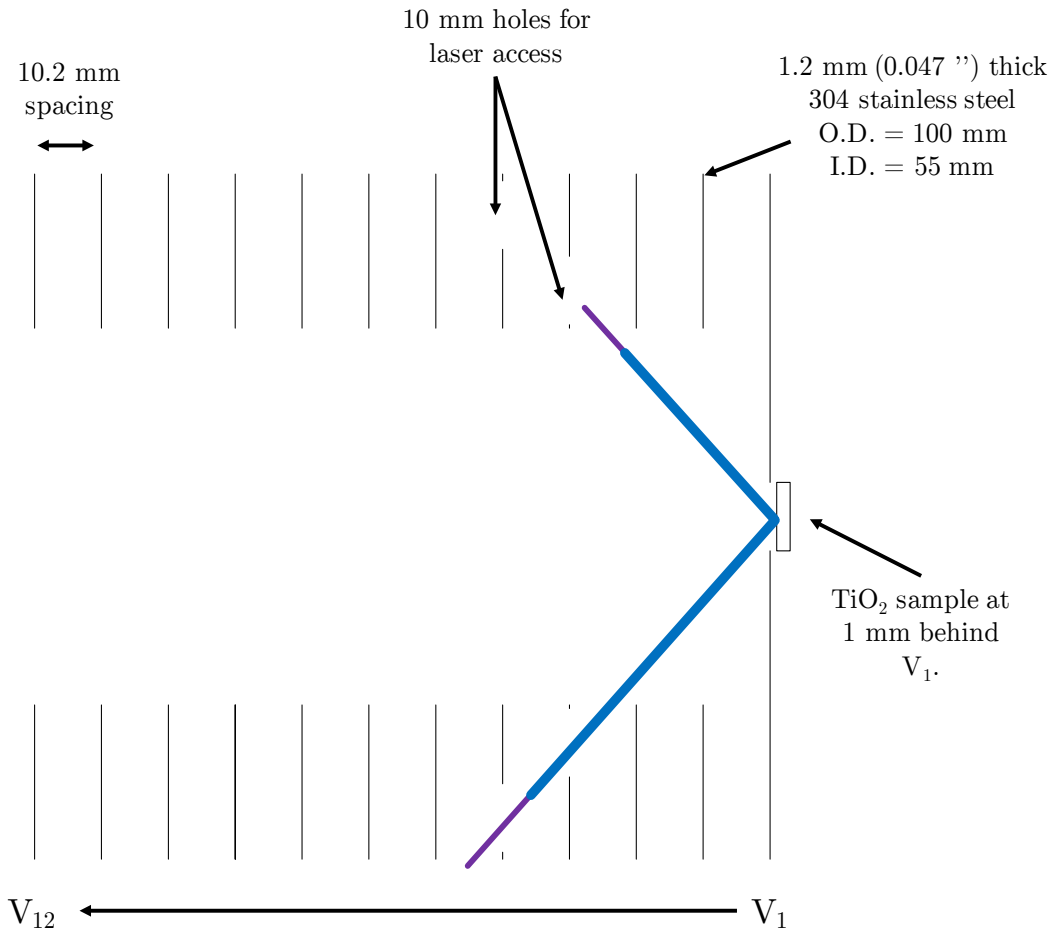

Figure 6.2: Two dimensional cross section of the ion imaging optics. This design contains 11 tunable lenses plus a final lens that is held at ground potential. Carefully positioned holes in V_4 and V_5 allow for co-linear pump and probe laser beams to access the surface at an angle of $\sim 45^\circ$ with respect to the surface normal.

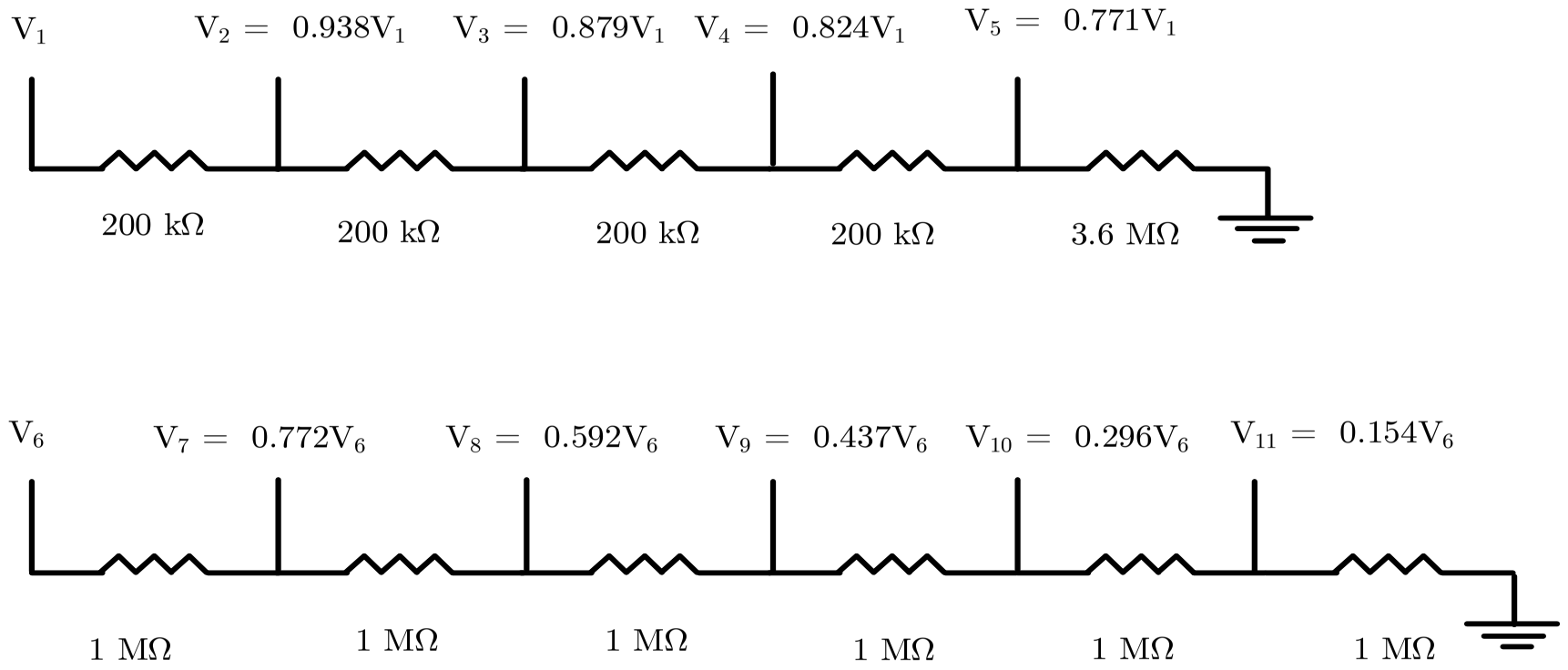

Figure 6.3: Circuit diagram of the voltage divider for the ion optics. Instead of having 11 individually tunable lenses, the ion optics were divided into two regions with two separate dividing circuits. This allows for easy adjustment of the V_1:V_6 ratio which in turn determines the quality of the image focus. The voltages for each lens are given in terms of either V_1 or V_6 and for VMI experiments typical voltages used are 1100 V for V_1 and 800 V for V_6. The crystal is biased separately at a voltage of $7 - 9$ V higher than V_1.

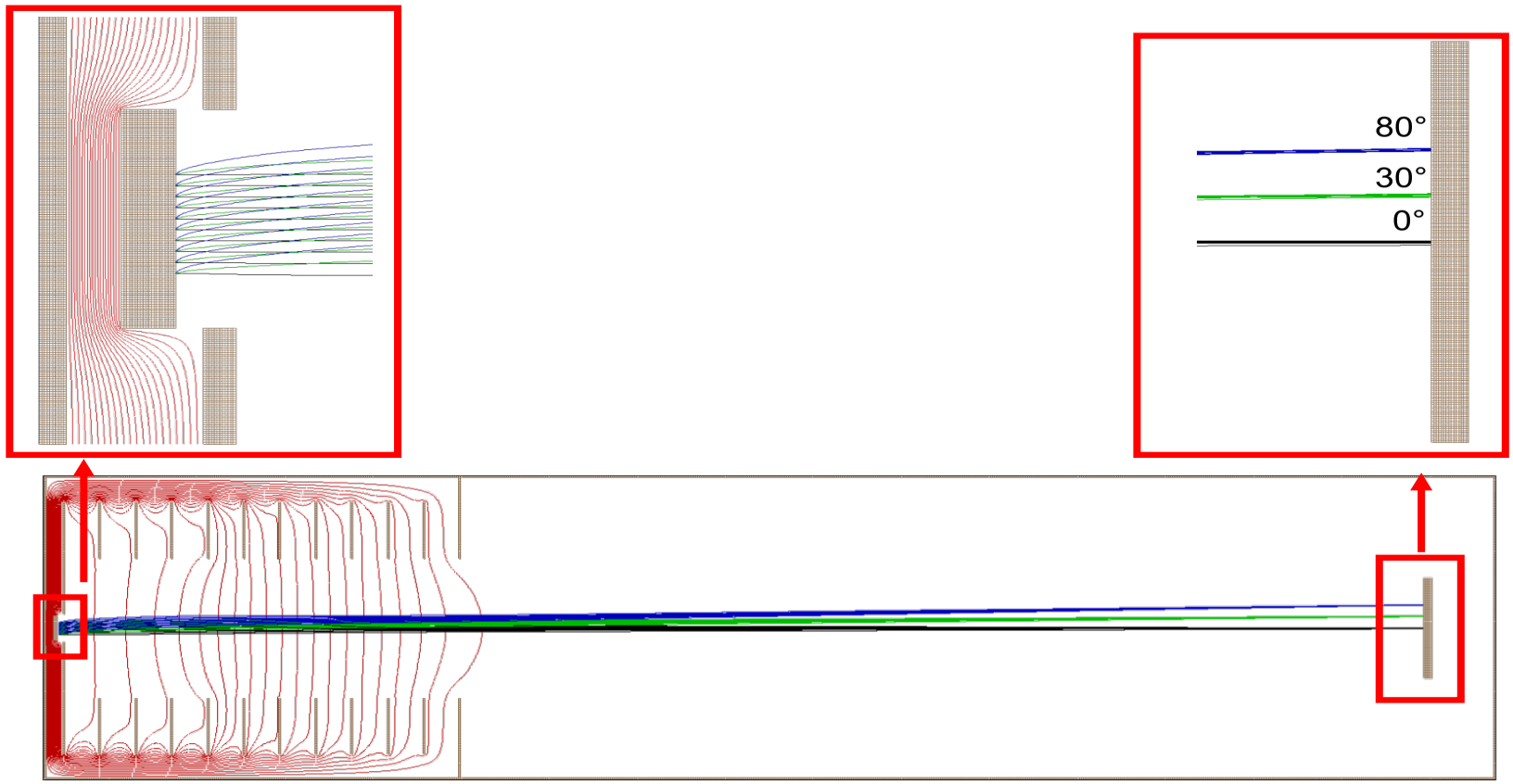

Figure 6.4: Computer representation of the imaging detector produced with the help of SIMION 8.0 software. The red contours show the electric field potentials inside the detector and the black, green and blue traces represent ion trajectories for methyl radicals desorbing at angles of 0, 30 and 80 degrees with respect to the surface normal. Ions are flown beginning at the crystal surface across an distance of $\pm$ 2.5 mm from the center of the crystal and are focused in groups at the detector depending upon their initial trajectory

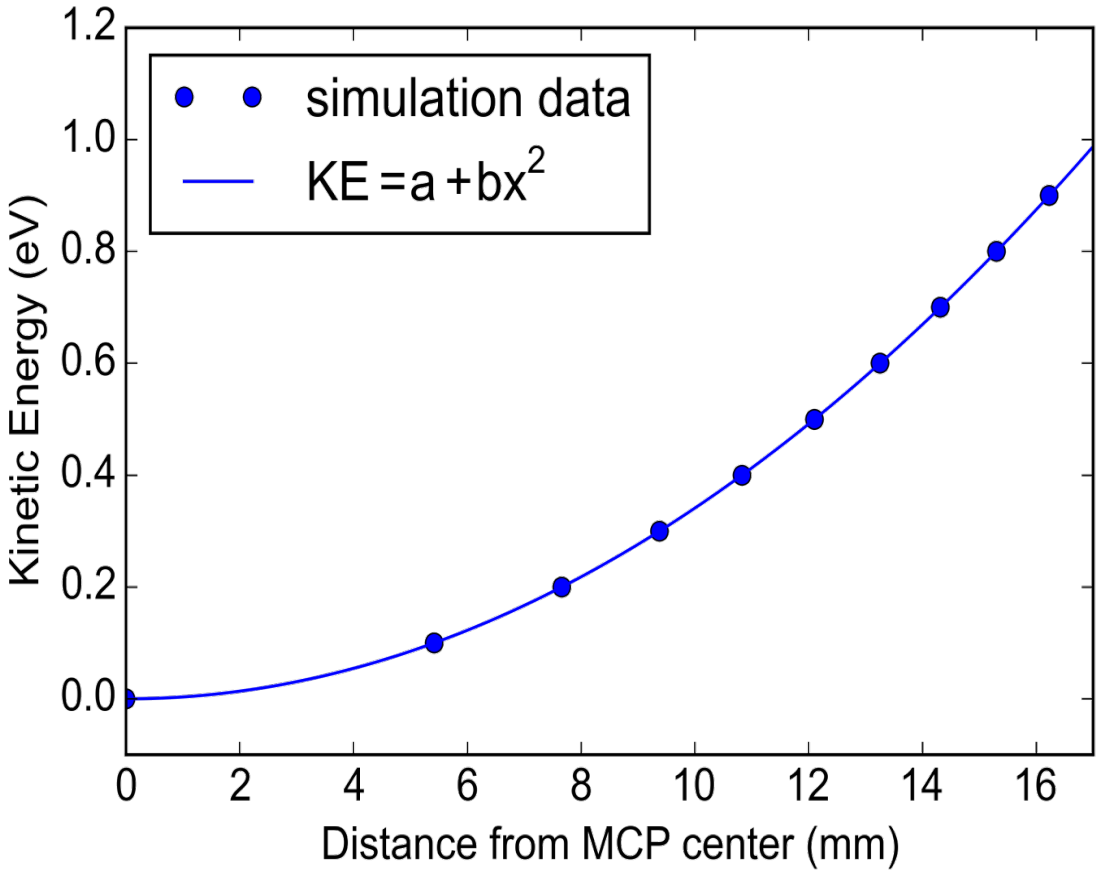

Figure 6.5: Graph showing the initial ion kinetic energy as a function of final position on the MCP detector. This calculation was performed for methyl radicals moving in a trajectory parallel to the MCP and so the energy is simply the kinetic energy along this direction. This is intended to simulate methyl radical ejection following CH_3I photolysis where the photolysis laser polarization vector is also parallel to the detector plane.

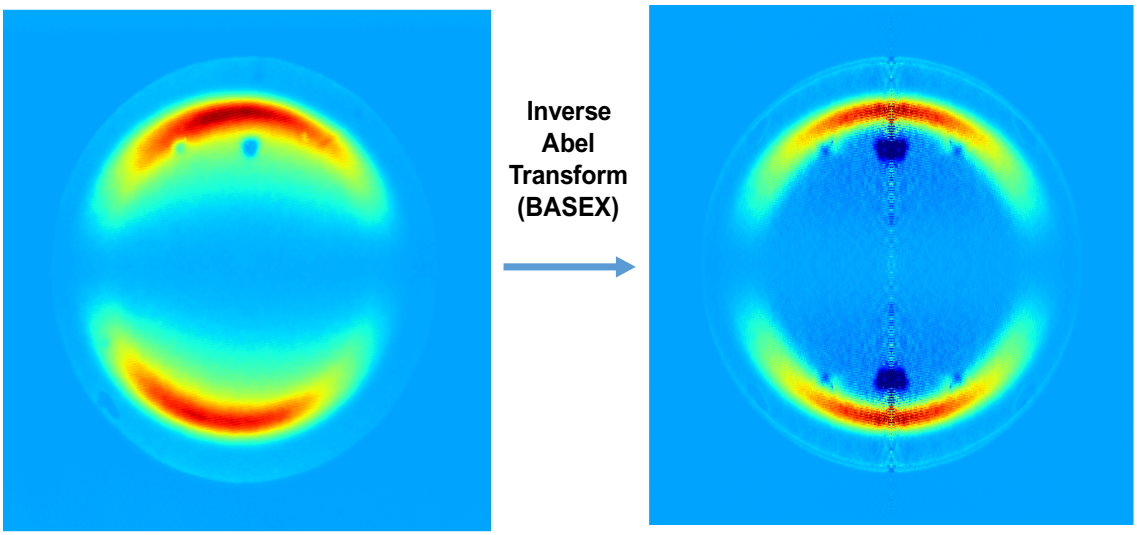

Figure 6.6: Velocity mapped image of methyl radicals following dissociation of CH_3I. The raw image is shown on the left and the inverse Abel-transformed image is shown on the right. The inverse Abel transformation is necessary to extract the correct energy distribution from the raw image which is a 2D projection of a 3D ion cloud. Dark blue spots in the transformed image are due to dead spots in the detector. The dissociation of CH_3I and ionization of methyl radicals was performed by a single laser tuned to 286.3 nm which represents the 0_0^0 band of the $4p_z$ Rydberg state of CH_3. Hence following a one photon absorption/dissociation step, methyl radicals were ionized through a $2+1$ REMPI process.

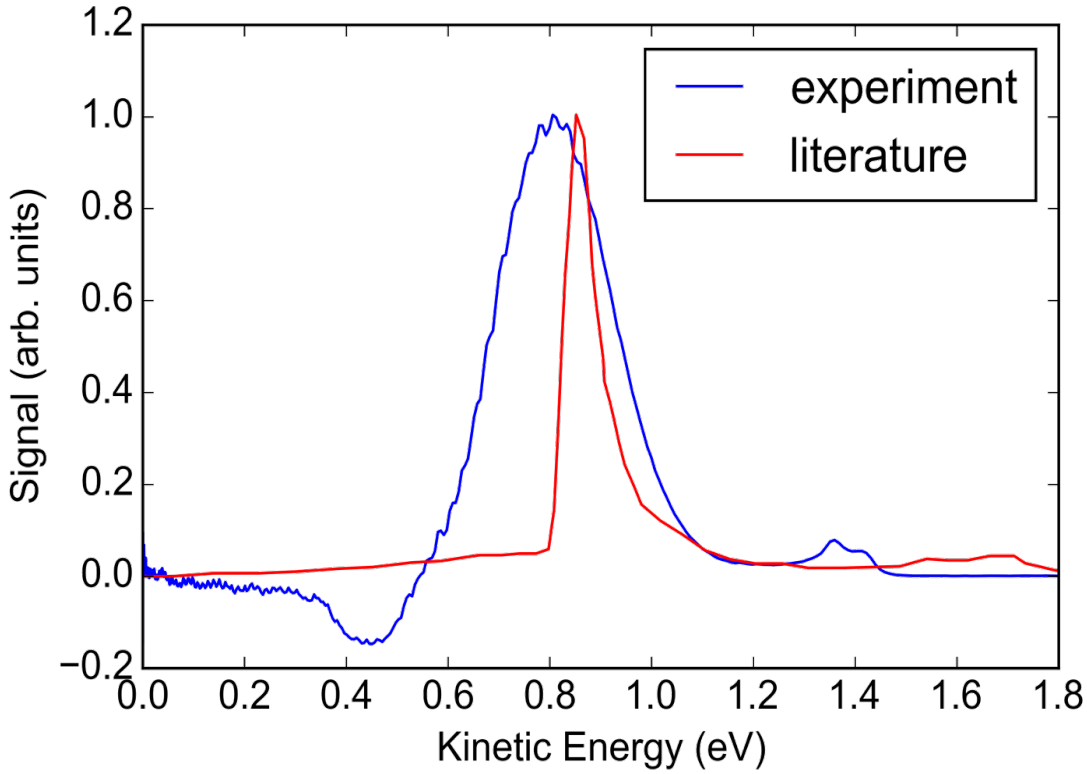

Figure 6.7: Kinetic energy distribution for methyl radicals following CH_3I photolysis. The data was extracted from the transformed image and represents the summed signal over a 2π integration about the image center. Experimental data is shown as a blue trace while the data in red is taken from Eppink and Parker.[2]

7 Summary and Future Directions

The work presented here described several experiments concerning the photooxidation of small ketones and alcohols on TiO_2(110). Specifically, the use of pump-probe spectroscopic techniques enabled the dynamics of these photoreactions to be studied by providing insights into how energy is distributed in desorbing photoproducts. As described in this work, knowledge of photofragment kinetic energy as well as internal state distributions can provide interesting insights into the transition state and mechanism of these reactions. For example, the vibrationally resolved measurements on acetone photooxidation revealed a cold vibrational distribution (ν_2 umbrella mode) for methyl radicals which may potentially indicate a late transition state for this reaction. As another example, the experiments presented on alcohol photooxidation provided some clarity for the mechanism of these reactions by bridging the gap between previous studies on alcohol photooxidation and recent work on ketone photooxidation.

While these results help to improve knowledge of these systems, there are a couple of outstanding issues that remain to be addressed either experimentally or theoretically. The first question concerns the high reactivity of the ketone-diolate species as compared to the ketone.[14,18,19] As described earlier, one hypothesis is that the HOMO levels for the diolate species overlap more favorably with the TiO_2 valence band maximum and thus lead to a more efficient reaction.[15] Another hypothesis could be that this oxygen adatom which forms the diolate creates a localized area of electron density which promotes hole diffusion to this site and leads to reaction. This type of mechanism would be more of a band bending effect that has been observed in oxygen photodesorption experiments by the Yates group.[12] Efforts to resolve this issue are ongoing and involve both an experimental and theoretical approach.[118]

From a reaction dynamics perspective, future experiments on these systems should seek to observe reaction products on an ultrafast time scale. By studying photoproduct formation in real time, individual pathways leading to reaction can be better understood. Such experiments require a laser system capable of producing pulses on a femtosecond time scale

as we expect the bond breaking/formation process to occur on a femtosecond to picosecond time scale.[119] These types of experiments have already been performed by Bernhardt and co-workers for the photodissociation of CH_3I adsorbed on MgO and Au surfaces.[120–128] The samples were irradiated with 266 nm radiation which induces CH_3 dissociation following a one-photon absorption through the A-band of CH_3I. Neutral methyl products were then probed via a $2+1$ REMPI process through the $3p_z$ $^2A_2''$ Rydberg state. In order to study photoproduct formation on such time scales, the authors placed their prepared sample with adsorbed CH_3I in front of a TOF-MS and directed the pump and probe laser beams to the surface co-linearly at a 45° angle. Both laser beams must strike the surface because in order to observe product formation in real time, the products must be ionized at the surface. Ion signal is then collected as a function of pump-probe delay to reveal information regarding the real-time dynamics of CH_3I photodissociation. For the case of CH_3I photodissociation on MgO, the results of these experiments show that this reaction proceeds by two pathways: a fast dissociation (130 fs) that occurs when the $CH_3I^{*\ddagger}$ transition state is ionized directly to form CH_3^+ ions and a slow dissociation (680 fs rise time following 170 fs delay) that occurs when methyl radicals that are generated following dissociation collide with the surface prior to desorption.[125] These collisions occur because CH_3I molecules on MgO can adopt a configuration where the methyl groups are pointing toward the surface. If measurements like this were to be performed for acetone photooxidation, it is less likely that collisions would play a role in the reaction dynamics. Since the diolate geometry on the surface is relatively well defined with methyl groups pointing away from the surface, differences in dynamics due to surface collisions might not be observed (in contrast with CH_3I on MgO where CH_3I molecules can be oriented with the methyl radicals pointing toward the surface).

In the experiment described above, the MgO surface (which is an insulator) does not participate in charge transfer with the adsorbed molecules unlike TiO_2 surfaces involved in photocatalytic processes. For example, if the approach used by Bernhardt and co-workers was applied to the study of acetone photooxidation on TiO_2, the main process under in-

vestigation would be charge transfer between the acetone diolate and the TiO_2 surface. It is unclear whether there would be multiple charge transfer events that might present (i.e. charge transfer from trap states vs. conduction and valence bands) or whether the observed dynamics would just indicate a single event. Time-resolved experiments involving electron transfer from SCN^- molecules to TiO_2 photoholes have been summarized in a review by Henderson.[6] These experiments used TiO_2 powders in solution and so the results may not be completely comparable to experiments performed in vacuum. At the very least they provide a good starting point for understanding what kind of timescales to expect for a photooxidation process. In these experiments, fast electron transfers (100 fs to 1 ps timescale) were attributed to interaction with non-thermalized holes whereas slow electron transfers ($>$ 100 ps) were attributed to interaction with holes trapped far from reaction sites.[129,130] Based on these studies it might be expected that, at the very least, ultrafast experiments on TiO_2 photooxidation would be able to distinguish between charge transfer from localized carriers and carriers which must travel a longer distance to the reaction site.

In addition to exploring the ultrafast dynamics of organic photooxidation reactions, it would also be desirable to correlate these ultrafast measurements with product kinetic energy and angular distribution. This could be accomplished through use of a TOF-MS capable of velocity map imaging which would provide data on angular distributions as described in chapter 4 of this dissertation. Furthermore, by modeling the ion time-of-flight as a function of initial kinetic energy, it should be possible to extract kinetic energy distributions from the time-of-flight signals. Such experiments would yield a great deal of information about how final state properties of desorbing photoproducts are related to the initial events which lead to product formation.

8 References

[1] Pang, C. L.; Lindsay, R.; Thornton, G. *Chemical Society Reviews* **2008**, *37*, 2328–2353.

[2] Eppink, A.; Parker, D. H. *Journal of Chemical Physics* **1999**, *110*, 832–844.

[3] Web of Science Database, apps.webofknowledge.com, accessed Jan. 11, 2016.

[4] Fujishima, A.; Honda, K. *Nature* **1972**, *238*, 37–38.

[5] Fujishima, A.; Zhang, X.; Tryk, D. A. *Surface Science Reports* **2008**, *63*, 515–582.

[6] Henderson, M. A. *Surface Science Reports* **2011**, *66*, 185–297.

[7] Hoffmann, M. R.; Martin, S. T.; Choi, W.; Bahnemann, D. W. *Chemical Reviews* **1995**, *95*, 69–96.

[8] Diebold, U. *Surface Science Reports* **2003**, *48*, 53–229.

[9] Lu, G. Q.; Linsebigler, A.; Yates, J. T. *Journal of Chemical Physics* **1995**, *102*, 4657–4662.

[10] Henderson, M. A.; Epling, W. S.; Perkins, C. L.; Peden, C. H. F.; Diebold, U. *The Journal of Physical Chemistry B* **1999**, *103*, 5328–5337.

[11] Petrik, N. G.; Kimmel, G. A. *The Journal of Physical Chemistry C* **2011**, *115*, 152–164.

[12] Zhang, Z.; John T. Yates, J. *The Journal of Physical Chemistry Letters* **2010**, *1*, 2185–2188.

[13] Zhang, Z.; John T. Yates, J. *Chemical Reviews* **2012**, *112*, 5520–5551, PMID: 22783915.

[14] Henderson, M. A. *The Journal of Physical Chemistry B* **2005**, *109*, 12062–12070.

[15] Wilson, D. P.; Sporleder, D.; White, M. G. *Journal of Physical Chemistry C* **2012**, *116*, 16541–16552.

[16] Wilson, D. P.; Sporleder, D. P.; White, M. G. *The Journal of Physical Chemistry C* **2013**, *117*, 9290–9300.

[17] Wilson, D. P.; Sporleder, D.; White, M. G. *Physical Chemistry Chemical Physics* **2012**, *14*, 13630–13637.

[18] Petrik, N. G.; Henderson, M. A.; Kimmel, G. A. *The Journal of Physical Chemistry C* **2015**, *119*, 12262–12272.

[19] Petrik, N. G.; Henderson, M. A.; Kimmel, G. A. *The Journal of Physical Chemistry C* **2015**, *119*, 12273–12282.

[20] Henderson, M. A. *Journal of Physical Chemistry B* **2004**, *108*, 18932–18941.

[21] Li, M.; Hebenstreit, W.; Diebold, U.; Tyryshkin, A. M.; Bowman, M. K.; Dunham, G. G.; Henderson, M. A. *Journal of Physical Chemistry B* **2000**, *104*, 4944–4950.

[22] Johnson, P. M. *Accounts of Chemical Research* **1980**, *13*, 20–26.

[23] Page, R. H.; Larkin, R. J.; Kung, A. H.; Shen, Y. R.; Lee, Y. T. *Review of Scientific Instruments* **1987**, *58*, 1616–1620.

[24] Fox, M. A.; Dulay, M. T. *Chemical Reviews* **1993**, *93*, 341–357.

[25] Coronado, J. M.; Kataoka, S.; Tejedor-Tejedor, I.; Anderson, M. A. *Journal of Catalysis* **2003**, *219*, 219–230.

[26] Wang, T. H.; Dixon, D. A.; Henderson, M. A. *Journal of Physical Chemistry C* **2010**, *114*, 14083–14092.

[27] Epling, W. S.; Peden, C. H. F.; Henderson, M. A.; Diebold, U. *Surface Science* **1998**, *412-13*, 333–343.

[28] Petrik, N. G.; Kimmel, G. A. *The Journal of Physical Chemistry Letters* **2010**, *1*, 1758–1762.

[29] Herzberg, G. *Molecular Spectra and Molecular Structure, vol. III. Electronic Spectra and Electronic Structure of Polyatomic Molecules*; D. Van Nostrand Company, Inc: Princeton, NJ, 1966.

[30] Srivastava, A.; Osgood, R. M. *Chemical Physics Letters* **2002**, *355*, 371–377.

[31] Fairbrother, D. H.; Briggman, K. A.; Stair, P. C.; Weitz, E. *Journal of Chemical Physics* **1995**, *102*, 7267–7276.

[32] Holbert, V. P.; Garrett, S. J.; Stair, P. C.; Weitz, E. *Surface Science* **1996**, *346*, 189–205.

[33] Polanyi, J. C.; Sze, N. S. K.; Wang, J. X. *Journal of Physical Chemistry A* **1997**, *101*, 6679–6687.

[34] Kutzner, J.; Lindeke, G.; Welge, K. H.; Feldmann, D. *Journal of Chemical Physics* **1989**, *90*, 548–555.

[35] Black, J. F.; Powis, I. *Journal of Chemical Physics* **1988**, *89*, 3986–3992.

[36] Hudgens, J. W.; DiGiuseppe, T. G.; Lin, M. C. *The Journal of Chemical Physics* **1983**, *79*, 571–582.

[37] PGOPHER, a Program for Simulating Rotational Structure, C.M. Western, University of Bristol, http://pgopher.chm.bris.ac.uk.

[38] Sporleder, D.; Wilson, D. P.; White, M. G. *The Journal of Physical Chemistry C* **2009**, *113*, 13180–13191.

[39] Rusu, C. N.; Yates, J. T. *Journal of Physical Chemistry B* **2000**, *104*, 1729–1737.

[40] Thompson, T. L.; Yates, J. T. *Journal of Physical Chemistry B* **2006**, *110*, 7431–7435.

[41] Henderson, M. A. *The Journal of Physical Chemistry C* **2008**, *112*, 11433–11440.

[42] Ogorzalek Loo, R.; Haerri, H. P.; Hall, G. E.; Houston, P. L. *Journal of Chemical Physics* **1989**, *90*, 4222–42364236.

[43] Comsa, G.; David, R. *Surface Science Reports* **1985**, *5*, 145–198.

[44] Garrett, S. J.; Holbert, V. P.; Stair, P. C.; Weitz, E. *Journal of Chemical Physics* **1994**, *100*, 4626–4636.

[45] DeSimone, A. J.; Olanrewaju, B. O.; Grieves, G. A.; Orlando, T. M. *The Journal of Chemical Physics* **2013**, *138*, 084703–9.

[46] Miller, E. R.; Muirhead, G. D.; Jensen, E. T. *Journal of Chemical Physics* **2013**, *138*.

[47] Trentelman, K. A.; Kable, S. H.; Moss, D. B.; Houston, P. L. *Journal of Chemical Physics* **1989**, *91*, 7498–7513.

[48] Kim, S. H.; Stair, P. C.; Weitz, E. *Journal of Chemical Physics* **1998**, *108*, 5080–5088.

[49] Snelson, A. *Journal of Physical Chemistry* **1970**, *74*, 537.

[50] Kim, J.; Kelley, J. A.; Ayotte, P.; Nielsen, S. B.; Weddle, G. H.; Johnson, M. A. *Journal of the American Society for Mass Spectrometry* **1999**, *10*, 810–814.

[51] Chandler, D. W.; Houston, P. L. *Journal of Chemical Physics* **1987**, *87*, 1445–1447.

[52] Eppink, A.; Parker, D. H. *Review of Scientific Instruments* **1997**, *68*, 3477–3484.

[53] Ashfold, M. N. R.; Nahler, N. H.; Orr-Ewing, A. J.; Vieuxmaire, O. P. J.; Toomes, R. L.; Kitsopoulos, T. N.; Garcia, I. A.; Chestakov, D. A.; Wu, S. M.; Parker, D. H. *Physical Chemistry Chemical Physics* **2006**, *8*, 26–53.

[54] Ji, Y. Y.; Koehler, S. P. K.; Auerbach, D. J.; Wodtke, A. M. *Journal of Vacuum Science and Technology A* **2010**, *28*, 807–813.

[55] Menges, M.; Baumeister, B.; Alshamery, K.; Freund, H. J.; Fischer, C.; Andresen, P. *Surface Science* **1994**, *316*, 103–111.

[56] Wilde, M.; Fukutani, K.; Murata, Y.; Kampling, M.; Al-Shamery, K.; Freund, H. J. *Surface Science* **1999**, *427–428*, 27–33.

[57] Burns, A. R.; Stechel, E. B.; Jennison, D. R. *Surface Science* **1993**, *280*, 359–368.

[58] Burns, A. R. *Surface Science* **1993**, *280*, 349–358.

[59] Corr, D.; Jacobs, D. C. *Review of Scientific Instruments* **1992**, *63*, 1969–1972.

[60] Kobrin, P. H.; Schick, G. A.; Baxter, J. P.; Winograd, N. *Review of Scientific Instruments* **1986**, *57*, 1354–1362.

[61] Koehler, S. P. K.; Ji, Y. Y.; Auerbach, D. J.; Wodtke, A. M. *Physical Chemistry Chemical Physics* **2009**, *11*, 7540–7544.

[62] Reid, M.; Koehler, S. P. K. *Review of Scientific Instruments* **2013**, *84*.

[63] Roscioli, J. R.; Bell, D. J.; Nelson, D. J.; Nesbitt, D. J. *Physical Chemistry Chemical Physics* **2012**, *14*, 4070–4080.

[64] Roscioli, J. R.; Nesbitt, D. J. *Faraday Discussions* **2011**, *150*, 471–479.

[65] Nomerotski, A.; Brouard, M.; Campbell, E.; Clark, A.; Crooks, J.; Fopma, J.; John, J. J.; Johnsen, A. J.; Slater, C.; Turchetta, R.; Vallance, C.; Wilman, E.; Yuen, W. H. *Journal of Instrumentation* **2010**, *5*.

[66] John, J. J. et al. *Journal of Instrumentation* **2012**, *7*.

[67] Brouard, M.; Campbell, E. K.; Johnsen, A. J.; Vallance, C.; Yuen, W. H.; Nomerotski, A. *Review of Scientific Instruments* **2008**, *79*, 123115–8.

[68] Sedgwick, I. et al. PImMS: A self-triggered, 25ns resolution monolithic CMOS sensor for Time-of-Flight and Imaging Mass Spectrometry. New Circuits and Systems Conference (NEWCAS), 2012 IEEE 10th International. 2012; pp 497–500.

[69] Clark, A. T. et al. *Journal of Physical Chemistry A* **2012**, *116*, 10897–10903.

[70] Brouard, M. et al. *Review of Scientific Instruments* **2012**, *83*, 114101.

[71] FitzPatrick, B. L.; Maienschein-Cline, M.; Butler, L. J.; Lee, S. H.; Lin, J. J. *Journal of Physical Chemistry A* **2007**, *111*, 12417–12422.

[72] Murdoch, M.; Waterhouse, G. I. N.; Nadeem, M. A.; Metson, J. B.; Keane, M. A.; Howe, R. F.; Llorca, J.; Idriss, H. *Nature Chemistry* **2011**, *3*, 489–492.

[73] Connelly, K. A.; Idriss, H. *Green Chemistry* **2012**, *14*, 260–280.

[74] Arsac, F.; Bianchi, D.; Chovelon, J. M.; Ferronato, C.; Herrmann, J. M. *Journal of Physical Chemistry A* **2006**, *110*, 4202–4212.

[75] Guzman, F.; Chuang, S. S. C. *Journal of the American Chemical Society* **2010**, *132*, 1502–1503.

[76] Hwang, S. J.; Raftery, D. *Catalysis Today* **1999**, *49*, 353–361.

[77] Kaise, M.; Nagai, H.; Tokuhashi, K.; Kondo, S.; Nimura, S.; Kikuchi, O. *Langmuir* **1994**, *10*, 1345–1347.

[78] Kim, K. S.; Barteau, M. A.; Farneth, W. E. *Langmuir* **1988**, *4*, 533–543.

[79] Larson, S. A.; Widegren, J. A.; Falconer, J. L. *Journal of Catalysis* **1995**, *157*, 611–625.

[80] Muggli, D. S.; Larson, S. A.; Falconer, J. L. *Journal of Physical Chemistry* **1996**, *100*, 15886–15889.

[81] Muggli, D. S.; Lowery, K. H.; Falconer, J. L. *Journal of Catalysis* **1998**, *180*, 111–122.

[82] Muggli, D. S.; McCue, J. T.; Falconer, J. L. *Journal of Catalysis* **1998**, *173*, 470–483.

[83] Nadeem, A. M.; Waterhouse, G. I. N.; Idriss, H. *Catalysis Today* **2012**, *182*, 16–24.

[84] Nimlos, M. R.; Wolfrum, E. J.; Brewer, M. L.; Fennell, J. A.; Bintner, G. *Environmental Science and Technology* **1996**, *30*, 3102–3110.

[85] Piera, E.; Ayllon, J. A.; Domenech, X.; Peral, J. *Catalysis Today* **2002**, *76*, 259–270.

[86] Pilkenton, S.; Hwang, S. J.; Raftery, D. *Journal of Physical Chemistry B* **1999**, *103*, 11152–11160.

[87] Rekoske, J. E.; Barteau, M. A. *Journal of Catalysis* **1997**, *165*, 57–72.

[88] Reztsova, T.; Chang, C. H.; Koresh, J.; Idriss, H. *Journal of Catalysis* **1999**, *185*, 223–235.

[89] Wu, W. C.; Chuang, C. C.; Lin, J. L. *Journal of Physical Chemistry B* **2000**, *104*, 8719–8724.

[90] Xu, W. Z.; Raftery, D. *Journal of Physical Chemistry B* **2001**, *105*, 4343–4349.

[91] Xu, W. Z.; Raftery, D.; Francisco, J. S. *Journal of Physical Chemistry B* **2003**, *107*, 4537–4544.

[92] Yu, Z. Q.; Chuang, S. S. C. *Journal of Catalysis* **2007**, *246*, 118–126.

[93] Bondarchuk, O.; Kim, Y. K.; White, J. M.; Kim, J.; Kay, B. D.; Dohnalek, Z. *Journal of Physical Chemistry C* **2007**, *111*, 11059–11067.

[94] Brinkley, D.; Engel, T. *Surface Science* **1998**, *415*, L1001–L1006.

[95] Brinkley, D.; Engel, T. *Journal of Physical Chemistry B* **1998**, *102*, 7596–7605.

[96] Brinkley, D.; Engel, T. *Journal of Physical Chemistry B* **2000**, *104*, 9836–9841.

[97] Farfan-Arribas, E.; Madix, R. J. *The Journal of Physical Chemistry B* **2002**, *106*, 10680–10692.

[98] Gamble, L.; Jung, L. S.; Campbell, C. T. *Surface Science* **1996**, *348*, 1–16.

[99] Jayaweera, P. M.; Quah, E. L.; Idriss, H. *The Journal of Physical Chemistry C* **2007**, *111*, 1764–1769.

[100] Kim, Y. K.; Hwang, C. C. *Surface Science* **2011**, *605*, 2082–2086.

[101] Kim, Y. K.; Kay, B. D.; White, J. M.; Dohnalek, Z. *Journal of Physical Chemistry C* **2007**, *111*, 18236–18242.

[102] Kim, Y. K.; Kay, B. D.; White, J. M.; Dohnalek, Z. *Catalysis Letters* **2007**, *119*, 1–4.

[103] Kim, Y. K.; Kay, B. D.; White, J. M.; Dohnalek, Z. *Surface Science* **2008**, *602*, 511–516.

[104] Kundu, S.; Vidal, A. B.; Nadeem, M. A.; Senanayake, S. D.; Idriss, H.; Liu, P.; Rodriguez, J. A.; Stacchiola, D. *The Journal of Physical Chemistry C* **2013**,

[105] Li, Z. J.; Smith, R. S.; Kay, B. D.; Dohnalek, Z. *Journal of Physical Chemistry C* **2011**, *115*, 22534–22539.

[106] Ma, Z.; Guo, Q.; Mao, X.; Ren, Z.; Wang, X.; Xu, C.; Yang, W.; Dai, D.; Zhou, C.; Fan, H.; Yang, X. *The Journal of Physical Chemistry C* **2013**,

[107] Nadeem, A. M.; Muir, J. M. R.; Connelly, K. A.; Adamson, B. T.; Metson, B. J.; Idriss, H. *Physical Chemistry Chemical Physics* **2011**, *13*, 7637–7643.

[108] Zehr, R. T.; Henderson, M. A. *Surface Science* **2008**, *602*, 2238–2249.

[109] Stein, S.E., director "Mass Spectra" by NIST Mass Spec Data Center in NIST Chemistry WebBook, NIST Standard Reference Database Number 69, ed. P.J. Linstrom

and W.G. Mallard, National Institute of Standards and Technology Gaithersburg MD, 20899, http://webbook.nist.gov, retrieved July 2, 2013.

[110] Muckerman, J. T. *Journal of Physical Chemistry* **1989**, *93*, 179–184.

[111] Goncharov, V.; Herath, N.; Suits, A. G. *Journal of Physical Chemistry A* **2008**, *112*, 9423–9428.

[112] Shen, M.; Henderson, M. A. *The Journal of Physical Chemistry Letters* **2011**, *2*, 2707–2710.

[113] Hickstein, D.D., Yurchack, R., Das, D., Shih, C., and Gibson, S.T., PyAbel(v0.7): A Python Package for Abel Transforms, 2016.

[114] Dribinski, V.; Ossadtchi, A.; Mandelshtam, V.; Reisler, H. *Review of Scientific Instruments* **2002**, *73*, 2634–2642.

[115] Ryazanov, M.; Reisler, H. *The Journal of Chemical Physics* **2013**, *138*.

[116] Fisher-Levine, M.; Nomerotski, A. *Journal of Instrumentation* **2016**, *11*, C03016.

[117] Llopart, X.; Ballabriga, R.; Campbell, M.; Tlustos, L.; Wong, W. *Nuclear Instruments and Methods in Physics Research Section A: Accelerators, Spectrometers, Detectors and Associated Equipment* **2007**, *581*, 485 – 494.

[118] Muraca, A.R., Kershis, M.D., Yu, H.G. and White M.G., to be published.

[119] Zewail, A. H. *The Journal of Physical Chemistry A* **2000**, *104*, 5660–5694.

[120] Vaida, M. E.; Hindelang, P. E.; Bernhardt, T. M. *The Journal of Chemical Physics* **2008**, *129*.

[121] Vaida, M. E.; Bernhardt, T. M. *The European Physical Journal D* **2009**, *52*, 119–122.

[122] Vaida, M. E.; Bernhardt, T. M. *ChemPhysChem* **2010**, *11*, 804–807.

[123] Vaida, M. E.; Bernhardt, T. M.; Barth, C.; Esch, F.; Heiz, U.; Landman, U. *physica status solidi (b)* **2010**, *247*, 1001–1015.

[124] Vaida, M. E.; Gleitsmann, T.; Tchitnga, R.; Bernhardt, T. M. *physica status solidi (b)* **2010**, *247*, 1139–1146.

[125] Vaida, M. E.; Bernhardt, T. M. *Review of Scientific Instruments* **2010**, *81*.

[126] Vaida, M. E.; Bernhardt, T. M. *AIP Conference Proceedings* **2011**, *1387*, 146–154.

[127] Vaida, M. E.; Tchitnga, R.; Bernhardt, T. M. *Beilstein Journal of Nanotechnology* **2011**, *2*, 618–627.

[128] Vaida, M. E.; Bernhardt, T. M. *Faraday Discuss.* **2012**, *157*, 437–449.

[129] Furube, A.; Asahi, T.; Masuhara, H.; Yamashita, H.; Anpo, M. *Research on Chemical Intermediates* **2001**, *27*, 177–187.

[130] Morishita, T.; Hibara, A.; Sawada, T.; Tsuyumoto, I. *The Journal of Physical Chemistry B* **1999**, *103*, 5984–5987.